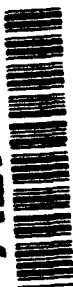TRANSIENT BODY FORCE EFFECTS ON THE
DRYOUT AND REWET OF A
HEATED CAPILLARY STRUCTURE

Dissertation

Michael K. Reagan. Major. USAF

AFIT/DS/AA/94-1

DTIC
ELECTE
APR 2 2 1994
S   G   D

DEPARTMENT OF THE AIR FORCE
AIR UNIVERSITY

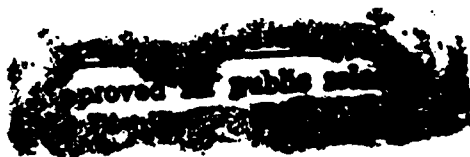# AIR FORCE INSTITUTE OF TECHNOLOGY

Wright-Patterson Air Force Base, Ohio

TRANSIENT BODY FORCE EFFECTS ON THE
DRYOUT AND REWET OF A
HEATED CAPILLARY STRUCTURE

Dissertation

Michael K. Reagan, Major, USAF

AFIT/DS/AA/94-1

DTIC
ELECTE
APR 2 2 1994
G

94-12265

94 4 21 046

TRANSIENT BODY FORCE EFFECTS ON THE

DRYOUT AND REWET OF A

HEATED CAPILLARY STRUCTURE

DISSERTATION

Presented to the Faculty of the Graduate School of Engineering

of the Air Force Institute of Technology

Air University

In Partial Fulfillment of the

Requirements for the Degree of

Doctor of Philosophy

Michael K. Reagan, B.S., M.S.

Major, USAF

April 1994

TRANSIENT BODY FORCE EFFECTS ON THE
DRYOUT AND REWET OF A
HEATED CAPILLARY STRUCTURE

Michael K. Reagan, B.S., M.S.

Major, USAF

Approved:

W. J. Bowman, Major, USAF, ENY Chairman	14 April 1994
	Date
Dr. W. C. Elrod, ENY	14 April 1994
	Date
Dr. M. E. Franke, ENY	14 April 1994
	Date
Dr. M. E. Oxley, ENC	14 April 1994
	Date
Dr. P. I. King, ENY	19 Apr 1994
	Date

Accepted:

Dr. J.S. Przemieniecki   Date
Institute Senior Dean

Preface

In the course of this work, I would like to thank my advisor, Major Jerry Bowman, for his assistance and guidance. His common sense approach to problem solving was immensely helpful, both professionally and personally. I am also thankful to the remainder of my committee, Dr. W. C. Elrod, Dr. M. E. Franke, and Dr. M. E. Oxley, for numerous and insightful discussions during my coursework and the experimental portion of the research. The success of this work is due in large part to their many combined years of experimental and mathematical expertise. Thanks also to Dr. P. I. King for many thought-provoking comments and suggestions during the draft phase of this document.

I would also like to thank the Aero Propulsion and Power Directorate of Wright Laboratories for sponsoring this work. Special recognition goes to Dr. Jerry Beam, of the Aerospace Power Division, who volunteered his time and talents to serve on the committee. His expertise in heat pipe technology was greatly appreciated.

Mr. Joe Hofele of the AFIT Model Shop was instrumental in the construction of the experimental apparatus. His expert skill and timely completion of my many short-notice requests is acknowledged and appreciated.

The department technicians, especially Mr Andy Pitts, were instrumental during the experimental portion of this work. Their contribution to the success of this work is appreciated. I also enjoyed the many good, non-technical discussions!

Finally, to my wife Kate, for understanding the bad times and helping me to enjoy the good times--thank you.

<div align="right">Mike Reagan</div>

Table of Contents

List of Figures

viii

List of Tables

List of Symbols

Symbol	Definition	Units

Arabic:

Symbol	Definition	Units
A	liquid cross-sectional flow area	m^2
$\bar{A}$	average liquid cross-sectional flow area	m^2
$\tilde{A}$	area over which shear stress acts	m^2
A_{in}	area over which external heat transfer occurs	m^2
$A*$	non-dimensional cross-sectional flow area	--
B	source term derivative, $B = \dfrac{\partial S}{\partial U}$	--
c	wave speed of the numerical solution	m/s
c_p	specific heat	J/kg-K
$C_0 - C_{10}$	constants defined in Chapter II	--
dx	grid spacing	m
d	front location extending from node nb	m
D_h	hydraulic diameter, $D_h = \dfrac{4A}{\rho}$	m
E	total energy per unit mass	W
	numerical spatial matrix defined in Chapter II	--
F_B	body force per unit mass, $F_B = g\sin\psi + \Omega^2 r$	m/s^2
F_C	capillary force per unit mass, $F_C = \dfrac{\sigma A}{R\rho\forall}$	m/s^2
f	friction coefficient between groove wall and liquid	--
G	numerical amplification factor defined in Chapter III	--
g	gravitational constant, $g = 9.81$	m/s^2
H	modified flux function defined in Chapter III	--
h	average liquid height, $h = \dfrac{A}{w}$	m
$\bar{h}$	average liquid hydrostatic height, $\bar{h} = \dfrac{h\cos\psi}{2}$	m
$\tilde{h}$	average liquid potential height	m
$\hat{h}$	average liquid height defined in Chapter II, $\hat{h} = 2\bar{h}$	m
h_{in}	heat transfer coefficient between groove wall and liquid	W/m^2-K
h_l	average liquid height in the groove, $h_l = (1 - \dfrac{h_p}{\delta})$	m
h_p	depth gauge measurement defined in Chapter IV	m
I	imaginary constant, $I = (-1)^{0.5}$	--
i, j	numerical counters	--
$J, \bar{J}, \tilde{J}$	Jacobian matrices defined in Chapter III	--
k	thermal conductivity	W/m-K

L_w	groove length	m
$\{M\}$	multiplier matrix defined in Chapter II	--
m	mass	kg
$\dot{m}$	mass flow rate, $\dot{m} = \rho A V$	kg/s
P	average liquid pressure	N/m²
P_c	capillary pressure, $P_c = P_v - P$	N/m²
P_v	ambient pressure	N/m²
$P*$	non-dimensional liquid pressure	--
$\wp$	wetted perimeter	m
Nu	Nusselt Number, $Nu = \dfrac{hD_h}{k}$	--
Q_{cond}	rate of energy transfer due to axial conduction, $Q_{cond} = -kA\dfrac{\partial T}{\partial x}$	W
Q_{in}	rate of energy transfer between groove wall and liquid, $Q_{in} = h_{in}A_{in}(T_g - T)$	W
Q_{out}	rate of energy transfer between the liquid and the environment due to evaporation, $Q_{out} = \dot{m}_e\lambda$	W
Q_{rad}	rate of energy transfer between the liquid and the environment due to radiation transfer, $Q_{rad} = \sigma_{SB}(T^4 - T_\infty^4)$	W
R	liquid meniscus radius of curvature	m
$\hat{R}$	numerical matrix defined in Chapter III	--
Re	Reynolds Number, $Re = \dfrac{VD_h}{\nu}$	--
r	axial distance from center of rotation	m
r_h	hydraulic radius, $r_h = \dfrac{2A}{\wp}$	m
S	source term matrix	--
T	bulk liquid temperature	K
T_g	groove temperature	K
T_∞	ambient temperature	K
t	time	s
t_∞	total experimental run time	s
$t*$	non-dimensional time	--
U	numerical temporal matrix defined in Chapter II	--
V	liquid velocity	m/s
$\bar{V}$	groove structure translational velocity relative to inertial reference frame	m/s
V_∞	numerical reference velocity, $V_\infty = \dfrac{L_w}{t_\infty}$	m/s
$V*$	non-dimensional velocity	--
$\forall$	volume	m³
w	groove width	m

X	distance between groove and inertial reference frame	m
x	axial distance from groove center of rotation	m
x_0	stationary point used in Beam Piston Model	m
x^*	non-dimensional distance	--
z	height dimension defined in Chapter II	m

Greek:

α^*	groove aspect ratio, $\alpha^* = \dfrac{w}{\delta}$	--
γ	angle describing axial variation of liquid cross-sectional flow area	rad
Δt	numerical timestep	s
Δx	numerical grid spacing	m
δ	groove depth	m
θ	wetting angle	rad
	variable defined in Fourier component in Chapter III only	--
$\hat{\Lambda}$	diagonal matrix defined in Chapter III	--
λ	latent heat of vaporization	J/kg
λ_1, λ_2	eigenvalues defined in Chapter III	m/s
μ	absolute viscosity	kg/m-s
ν	kinematic viscosity	m^2/s
ξ_1, ξ_2	eigenvectors defined in Chapter III	--
π	numerical constant, $\pi = 3.14159$	--
ρ	liquid density, $\rho = 785$	kg/m^3
ρ_e	vapor density	kg/m^3
ρ_∞	reference density, $\rho_\infty = 785$	kg/m^3
ρ^*	non-dimensional density	--
σ	liquid surface tension coefficient	N/m
σ_{SB}	Stefan-Boltzmann constant, $\sigma_{SB} = 5.67 \times 10^{-8}$	W/m^2-K^4
τ	shear stress between groove wall and liquid	N/m^2
ψ	groove tilt angle	rad
Ω	groove rotation rate	rad/s
$\dot{\Omega}$	time rate of change of groove rotation, $\dot{\Omega} = \dfrac{d\Omega}{dt}$	rad/s^2
ω	groove frequency	s^{-1}
∂	partial derivative	--

Subscripts:

c	capillary	--
$c1, c2, c3$	critical area designators	--
co	condenser	--
e	evaporation	--

ev	evaporator	--
ep	extinction point	--
g	groove	--
int	internal	--
lv	liquid-vapor	--
sec	sector	--
nb	new boundary	--
r	remaining	--
sl	solid-liquid	--
sv	solid-vapor	--
t, x	temporal and spatial partial derivatives used in Chapter III	--
w	wick	--

Superscripts:

*	non-dimensional	--
n	time level	--
T	transpose	--

Abstract

A transient, one-dimensional numerical code was developed to model the liquid flow in a non-uniformly heated, axial square groove. The groove was subjected to transient body forces up to approximately 0.51 m/s². Axial variation in meniscus levels, shear stress and heat transfer between the groove wall and the liquid, axial conduction through the liquid, evaporation and body forces were accounted for in the model. Dryout and rewet of the groove was allowed; the front location was determined using conservation of mass and linear extrapolation.

A physical experiment was performed with a stainless steel plate into which eight square grooves were machined. Ethanol was used as the working liquid. One end of the plate was tilted relative to the other end and this tilt was varied with time, thereby providing the transient body force. The depth of the ethanol in the groove, and the dryout and rewet front locations, were experimentally measured.

Within the uncertainty of the measurements, the numerical results from the code predicted the correct movement of liquid within the groove structure and also the correct position of the dryout and rewet fronts.

TRANSIENT BODY FORCE EFFECTS ON THE DRYOUT AND REWET OF A HEATED CAPILLARY STRUCTURE

I. *Introduction*

In recent years, heat transfer devices that utilize the phase change of a working fluid within a capillary structure have been proposed as a means of thermal management in the aerospace industry. Two examples of these heat transfer devices are the heat pipe and the capillary-driven evaporator. Proposed uses of these devices include electronics cooling (1-4) and engine inlet and wing leading edge cooling (5-10). Also, these devices are being used more and more as a means of thermal management on space-based platforms (11-16).

The environment of the aerospace vehicle or the space-based platform is one where these capillary devices have traditionally not been used. The aerospace environment is, in fact, a dynamic one where time-varying body forces influence the movement of liquid in the capillary structure of these devices. This is supported by a 1991 report which concluded that the thermal and environmental loadings on these devices are generally not constant but change with time depending on the ambient conditions (17). Additionally, a conclusion from a 1989 paper stated that the operational response of these devices was dependant on their environment, which was generally dynamic (18). These conclusions demonstrate that transient effects must be accounted for properly. Acceptance of capillary-driven heat transfer devices as the primary means of cooling in these dynamic environments will depend on a thorough understanding of their operation under the expected transient conditions (3).

Thesis

The liquid motion in a non-uniformly heated capillary structure subject to transient body forces may be numerically modeled. Specifically, the dryout and rewet process in such a structure may be accurately predicted.

Definitions

Several terms used in the thesis are now defined. The first term is transient body force; this simply refers to any body force that is varying with time. The body force may be varying in magnitude or direction or both. The second term is capillary structure (also referred to as a wick); this refers to a structure containing a liquid whose characteristic dimensions are such that a meniscus forms at the liquid-vapor interface. Additionally, in the absence of body forces, the motion of the liquid in such a structure must be induced by the forces generated by the curved interface. The third term is dryout; this refers to the process where a capillary structure, that is initially full of liquid, becomes void of liquid due to evaporation or bulk motion. The final term, rewet, refers to the opposite behavior; namely, the process where a capillary structure, initially void of liquid, becomes full.

Two additional terms which are used extensively in this document are now defined. The first of these is recession; this refers to the formation of the meniscus in the capillary structure. Consider a clean glass buret that is initially filled to the top with water such that no meniscus exists. Over time, as water evaporates from the top of the buret, the level of water will decrease and a meniscus will form. As more water evaporates, the level in the buret will continue to decrease. This decrease is referred to as the recession of the liquid.

The second additional term, front, is related to the terms dryout and rewet described above. When a capillary structure is in a state of dryout, there is a region in the structure where liquid is present, termed wet, and a region where there is no liquid, termed dry. The interface between the dry and wet regions in a capillary structure is defined as the front. Different front definitions are used by different researchers; the one used in this work is specifically defined in Chapter IV. Note that liquid in a capillary structure necessarily recedes before dryout occurs.

Literature Review

Since the obvious application of this work is to a heat pipe wick, the literature review was focused in this area. Several papers were found relating to the effect of body forces on heat pipe performance (19-29). The bulk of knowledge on body force effects can be divided into that dealing with steady-state body forces (constant accelerations or vibrations) and that dealing with transient body forces. The bulk of literature on body force effects lies in the steady-state category. The information pertaining to transient body forces will now be discussed.

In August 1990, NASA Lewis Research Center organized a workshop on modeling heat pipe performance under transient conditions (30). Conclusions from the workshop indicated that modeling of the liquid flow in the wick with conduction in the wall was the most important part of the transient heat pipe problem. They recommended continued emphasis on experiments geared toward physical understanding of the liquid flow, especially the dryout and rewet phenomena. They noted that no work was underway to study body force-induced transients during heat pipe operation.

Yerkes et al. (28) studied the effects of transverse and axial accelerations with step power changes on the performance of a flexible copper/water heat pipe designed for use

on high performance fighter aircraft. Steady, periodic and burst transverse accelerations with frequencies of 0.01 and 0.03 Hz and peak-to-peak values of 1.1 to 9.8 g were experimentally tested. Results of the study indicated a partial dryout of the artery at higher accelerations. They also noted that reduction in the acceleration was the most effective method for rewetting the pipe. Theoretical analysis dealt only with the steady behavior of increased accelerations on the pipe's performance and no attempt was made to model the liquid flow in the wick. Essentially, this work verified that increased body forces, especially those directed axially along the pipe, caused the liquid in the wick to collect at one end of the pipe, a phenomenon referred to as pooling. Additionally, it showed that reducing the body force was the most effective means of redistributing the pooled liquid along the wick. This work was important in that it was the first to actually document the dryout of the wick due to transient body forces.

One paper was found that attempted to visually observe the effect of transient body forces on the liquid flow in a wick structure. In this work, Hawthorne (27) studied the effect of a transient body force on the liquid flow in a single, heated capillary groove, simulating the flow in a heat pipe wick. The transient body force was generated by rotating the groove. He discovered that the extent of dryout in the groove depended on the magnitude and duration of the rotation transient. This work was important in that it visually verified what had been experimentally measured; namely, body forces (in this case, transient) served to move the liquid in the wick such that a dryout condition occurred. Also, by proper application of the same transient body force, a rewet of the dried-out groove was possible. No analytical model, other than a steady-state calculation of the capillary limit, was made.

Several investigators have attempted to numerically model the liquid flow in a heat pipe wick (31-39). Two numerical models repeatedly found in the literature are the

Groove Analysis Program (GAP) and the Beam piston model. A description of each model is found in Appendix A. The underlying assumptions made in each of these models are representative of those made in most numerical wick models. Limitations specific to each model are described below.

The GAP model (32) is a steady-state formulation that is applicable only to grooved structures and treats the body forces as steady; no temporal or spatial variations are allowed. The liquid radius of curvature in the groove is properly modeled, allowing it to vary along the groove axis. A limitation, however, is that this radius of curvature is only allowed to vary from a minimum at the evaporator equal to one-half the groove width to a maximum at the condenser equal to the radius of the vapor space. Based on Hawthorne's observations, this limits the capillary pumping to an arbitrarily low value.

The Beam piston model (33) is an unsteady formulation that does not include body forces. The wick is assumed to be entirely full up to the dryout front which means that no recession of the liquid along the groove axis is allowed. In an actual heat pipe, recession of the liquid into the wick can occur without causing dryout and always occurs as a precursor to dryout. Visual observations from the work of Hawthorne (27) and Ambrose et al. (35) have verified this behavior. Because liquid recession into the wick is ignored, the Beam piston model predicts dryout earlier than actually occurs.

A limitation of both models is that neither attempts to describe the nature or behavior of the liquid front within the wick. In the GAP model, no liquid front is allowed to develop; the simulations are stopped when the capillary limit is achieved. In the Beam model, the front is treated like a piston with no attempt to describe what it actually looks like.

Finally, both models assume that momentum changes in the liquid are negligible. This assumption reduces the liquid momentum equation to a form of Darcy flow, which

models the pressure drop by equating the sum of pressure, shear and body force terms to zero and neglects any change in the liquid inertia (40). During steady-state behavior, the liquid velocity is small and hence, inertia effects are probably negligible. The same conclusion cannot be deduced for the case of a transient body force environment where inertia effects can be significant.

Summary

Based on the experimental work accomplished to date, there is sufficient evidence to suggest that body forces do influence the liquid flow in a capillary structure. Specifically, these body forces act on the liquid and move it in a manner that can cause a dryout condition. These same body forces can also effect a rewet of the dried-out region.

The capability to numerically model unsteady capillary flow subject to transient body forces is inadequate. Several simplifying assumptions in the unsteady model presented above make results from this model questionable. A new, more realistic model is warranted. This new model must be an unsteady formulation that properly models recession and allows for transient body forces and changes in liquid momentum within the capillary structure.

Method of Study

This work approached the problem from both a numerical and experimental perspective and had the following objectives:

Numerical--develop and numerically solve a set of governing equations describing liquid motion in a capillary structure subject to transient body forces which generate a dryout and rewet condition.

Experimental--design and build a capillary structure and test section to obtain accurate, time-dependant data in order to verify the numerical model.

1-6

The numerical model was developed utilizing control volume techniques to represent the unsteady liquid flow in a capillary structure subject to transient body force effects. The capillary structure was modeled as an axial, square groove; a common capillary structure used in heat pipes (32). In addition to transient body forces, the numerical model included liquid recession, capillary and friction forces, heat transfer, evaporation, and dryout and rewet.

In order to validate the numerical model, several physical experiments were performed. These experiments were designed to simulate the groove structure and phenomena listed above. Experimental data was gathered on the liquid distribution in the groove and the location of the dryout and rewet fronts. This data was compared to the numerical results and used to validate the numerical model.

Research Value

The value of this research is twofold; first, many of the simplifying assumptions made in heat pipe wick models, which simulate capillary flow, are removed in this work. Additionally, the body force term is treated as a time-dependent variable and not as a constant. This makes the research important in that it is an attempt to develop a transient numerical model that more accurately describes liquid motion in a capillary structure subject to transient body forces.

The second reason this research needs to be accomplished lies in its power as a predictive and design tool. Because of the more accurate representation of the liquid inventory, dryout and rewet may be predicted more accurately.

Additionally, since this research deals specifically with body force-induced dryout of the wick, this new model may be used as an aid in designing and studying wick structures that are more tolerant to adverse transient body forces.

II. *Theory*

The purpose of this chapter is to define the physical principles governing liquid flow in capillary structures and to present a new model that will account for the unique operating characteristics of liquid flow in a capillary structure subject to transient body forces.

Surface Tension

At the interface between a liquid and a gas or between two liquids that do not mix, forces develop in the interface between them which cause it to behave like a membrane stretched over the liquid. In reality, there is no membrane, but the analogy helps explain some everyday occurrences. For example, a small needle will float on water if gently placed there even though the density of the needle is significantly greater than that of water. Similarly, water droplets will bead up on the surface of a newly waxed car.

These surface phenomena are due to the unbalanced cohesive forces acting on the liquid molecules near the surface. The molecular density in the interior of the liquid is much greater than the molecular density very near the surface. Molecules deep within the liquid repel each other, while molecules near the surface attract each other. The net effect is that the surface of the liquid is in tension (40).

If a cut of length dx is made in the interfacial surface, equal and opposite forces of magnitude σdx are exposed normal to the cut and parallel to the surface, as seen in Figure 2-1. σ is termed the surface tension coefficient and has units of N/m. σ is found to decrease with increasing temperature and is a function of the liquids on either side of the interface.

2-1
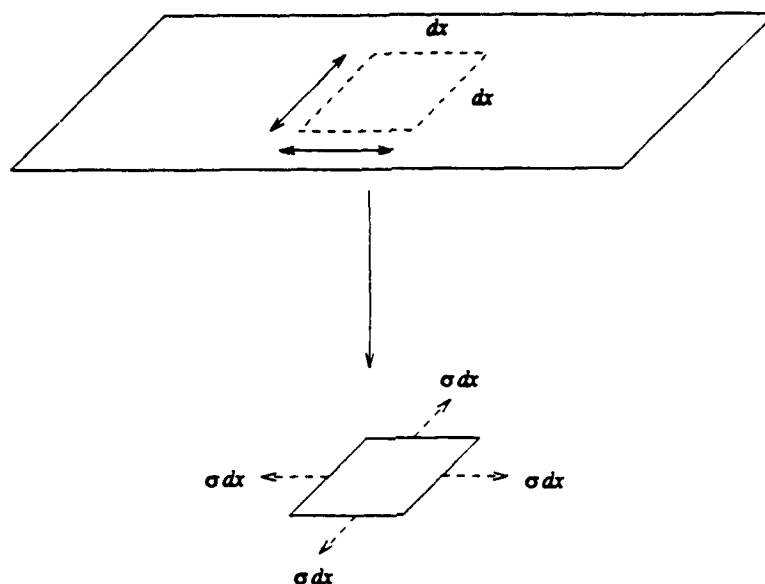
Figure 2-1. Interfacial Cut Showing Associated Shear Stress

Surface films also exist between solids and liquids, and solids and vapors, and each ha⁻ a respective surface tension coefficient, termed σ_{sl} and σ_{sv} . The curvature of a liquid surface near a solid interface depends on the difference between these two coefficients. Consider the solid-liquid-vapor interfaces seen in Figure 2-2. If σ_{sv} is greater than σ_{sl} , then the net resulting force, σ_{lv} , is up and to the left and liquid is pulled up the side of the wall. The angle between the wall and the resultant force, θ , is termed the wetting angle. In this instance, the wetting angle is some value between 0 and $\pi/2$ radians. Detergents and wetting agents both serve to reduce the wetting angle of a liquid to a value less than $\pi/2$ radians. The meniscus that is formed by water in a glass capillary tube is an example of a liquid that wets a surface.

If, however, σ_{sv} is less than σ_{sl} , then the net resulting force is down and to the left and the liquid is pulled downward. The wetting angle in this case is greater than $\pi/2$

2-2
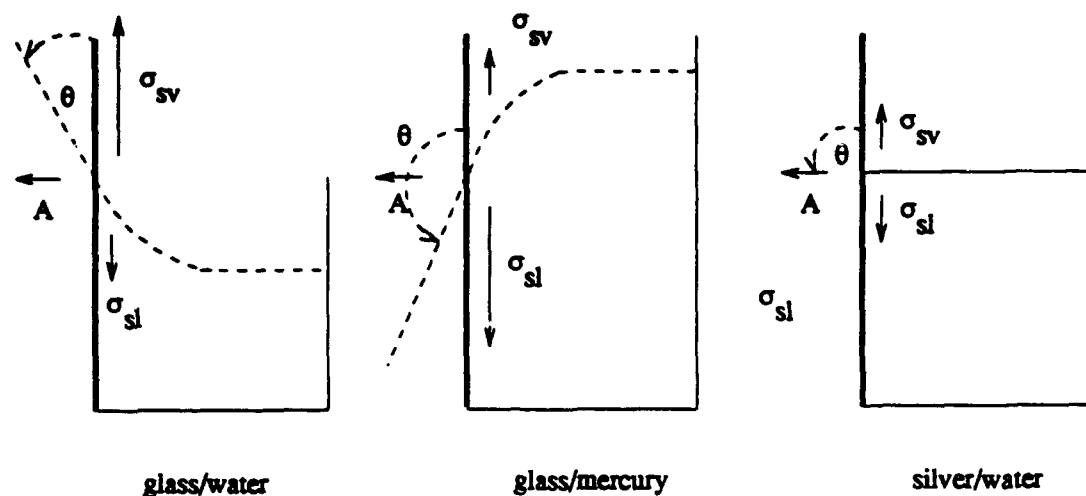
Figure 2-2. Solid-Liquid-Vapor Interfaces and Associated Surface Tension Forces

radians. This helps explain why water beads up on the surface of a newly waxed vehicle and why mercury forms an inverted meniscus in a barometer. Each of these is an example of a liquid that does not wet a surface.

Finally, if σ_{sl} and σ_{sv} are approximately equal, then the net force is perpendicular to the interface and the liquid has no tendency to climb up or down the wall. The wetting angle in this case is identically $\pi/2$ radians. The wetting angle, in all these cases, is only a function of the liquid and the material with which it is in contact.

If a similar wall is placed in close proximity to the one wall shown in Figure 2-2, with the liquid occupying the space between them, then two curved surfaces develop, one on either wall, and the resulting shape of the combined interfacial surface is curved and is termed a meniscus. A mechanical balance on the meniscus reveals a pressure

difference across this interface, with the pressure on the concave side being greater. This change in pressure due to a curved surface is termed capillarity and is now described.

Capillarity

Liquid flow in channels of small cross-section is influenced by the phenomenon of capillary action. Axial variation in the meniscus radius of curvature in the channel establishes an axial pressure gradient. This pressure gradient formed by the variation in meniscus shape, termed capillarity, provides the driving force that moves the liquid in the absence of any external accelerations. The pressure difference across the meniscus at any location along the channel is termed the capillary pressure and is a function of the channel geometry and the properties of the liquid within the channel.

The capillary pressure of the liquid, P_c, at any point along the channel is governed by the Laplace-Young equation (41)

$$P_c = \sigma \left(\frac{1}{R_1} + \frac{1}{R_2} \right) \qquad \text{[2-1]}$$

where σ is the surface tension of the working liquid (σ with no subscript refers to σ_{lv}), and R_1 and R_2 are the principal radii of curvature of the curved surface defining the interface between the liquid. Figure 2-3 shows a typical curved interface and its associated radii of curvature.

Two simple geometries illustrate the effect of capillarity and how the capillary pressure is determined. First, consider a capillary tube of radius, r, as seen in Figure 2-4. The two principal radii of curvature, R_1 and R_2, are equal to each other and can be shown to be $R = r/\cos\theta$. Substituting into Eqn [2-1] yields
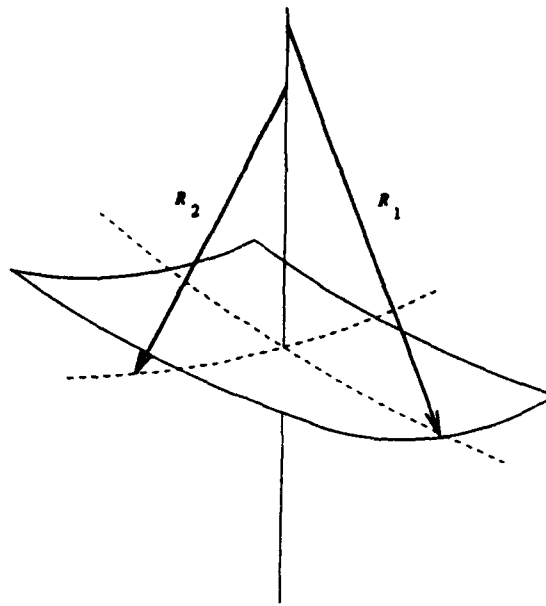
Figure 2-3. Typical Curved Interface and Associated Radii of Curvature
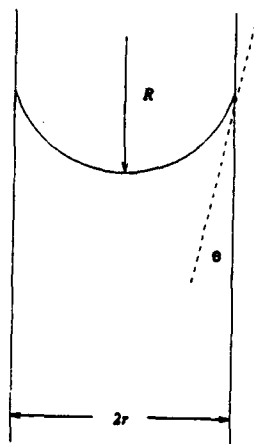
Figure 2-4. Capillary Tube
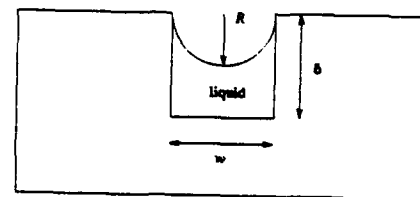
Figure 2-5. Rectangular Groove

$$P_c = \frac{2\sigma}{r} \cos\theta \qquad\qquad [2\text{-}2]$$

A second geometry that lends itself to a simple solution is the rectangular groove seen in Figure 2-5. In this geometry, one principal radius of curvature (the one extending into and out of the page), is infinite, while the other has a value of $R = w/2\cos\theta$, where w is the width of the groove. Substituting this into Eqn [2-1] yields

$$P_c = \frac{2\sigma}{w} \cos\theta \qquad\qquad [2\text{-}3]$$

The surface tension, wetting angle and geometry are assumed known in Eqn [2-2] and Eqn [2-3]. From these examples, the capillary pressure is seen to be only a function of the geometry of the capillary structure and the liquid.

New Model

A new thermo-hydrodynamic model is presented to analyze the liquid flow in a non-uniformly heated capillary structure exposed to a transient body force environment. Control volume analysis, including continuity, momentum and energy relationships, is used to model the liquid flow.

Assumptions. Several assumptions were made concerning the derivation of the mathematical model and many of the assumptions were made, so the particular experiment described in Chapter IV could be modeled. The assumptions made and the physical situation that was modeled are now described.

With respect to the capillary structure, an axial square groove structure was selected. The axial groove is a common heat pipe wick structure and has been used extensively in wicking tests at AFIT (27,42). The groove used for the experimental work was constructed from stainless steel. It had a constant width, w, and depth, δ, along its entire length. One end of the groove could be tilted relative to the other end and this tilt

could be varied with time, thereby providing a transient body force. Additionally, no flooding of the groove was allowed. In other words, the level of liquid in the groove was not allowed to exceed the groove depth. This was done to simplify the modeling process. Finally, the environmental pressure above the liquid in the groove was assumed to be constant and equal to the ambient pressure.

The working fluid was ethyl alcohol, frequently called ethanol. Ethanol was chosen because of its wetting compatibility with respect to stainless steel and also due to its ready availability. The ethanol was considered incompressible and homogeneous. Using published data (43) and over the temperature ranges of this work (295 K - 315 K), the density varied by less than one percent around a mean value of 785 kg/m^3; this value was used throughout the study.

Free convection and radiation losses from the liquid to the surrounding environment were considered negligible compared to the energy carried away via evaporation. Consider ethanol at a mean bulk temperature of 305 K; using experimental data from Chapter IV, the mass flux is approximately 1.7 gm/s-m^2. Using published data, the latent heat, λ, at this temperature is approximately 1000 KJ/kg (43). The energy flux associated with evaporation is the product of the mass flux and the latent heat. Therefore, the evaporative heat loss rate is approximately 1700 W/ m^2. Using a free convection coefficient of 15 W/m^2-K and an ambient temperature, T_∞, of 295 K, the free convection losses are approximately 150 W/m^2, an order of magnitude less than the evaporative heat loss. Finally, assuming the radiation losses to the environment to be proportional to $Q_{rad} = \sigma_{SB}\left(T^4 - T_\infty^4\right)$, where σ_{SB} is the Stefan-Boltzmann constant, the radiation losses are approximately 50 W/m^2, almost two orders of magnitude less than the evaporative heat loss. Based on these arguments, free convection and radiation losses were neglected.

Additionally, the flow of ethanol in the groove structure was assumed to be laminar. Early tests on a square groove with characteristic dimension of approximately 1.5 mm revealed that for groove tilt angles comparable to what was investigated in this study, the ethanol velocity was approximately 5 mm/s. This was estimated by monitoring the movement of impurities in the ethanol during the tilting of the groove. Using these dimensions and velocities, the Reynolds Number was on the order of 10. This is much less than the laminar limit of 2300. Based on this argument, the flow in the groove was assumed laminar at all times.

Several general assumptions were made. Changes in kinetic and potential energies within the liquid were considered negligible with respect to changes in its internal energy. Consider ethanol at a bulk temperature of 305 K. The change in internal energy per unit mass of ethanol at this temperature is given by $c_p \Delta T$, where c_p is the specific heat per unit mass. The specific heat of ethanol at this temperature is approximately 2.4 KJ/kg. Assuming a 1 K change in liquid temperature, in order for the change in liquid specific kinetic energy, $\Delta \left(\dfrac{V^2}{2} \right)$, to be order of magnitude close, velocities in excess of 70 m/s would have to exist in the groove structure. This is an unrealistic situation. A similar line of reasoning was used to neglect the influence of the potential energies. For the same 1 K change in temperature, changes in potential heights in excess of 200 m would be needed; again, an unrealistic scenario. Based on these arguments, changes in the kinetic and potential energies of the liquid were neglected in favor of changes in the internal energy.

Additionally, only one front was allowed to exist at any one time within the groove. This was done to simulate the dryout and rewet that was expected in the physical experiment.

Finally, the reference frame for this analysis remained fixed to the groove structure and rotated with the groove. This was done to simplify writing the equations of motion. However, in order to account for the fact that this was a non-inertial reference frame, a modification to the momentum equation was needed and will be discussed in more detail later in this chapter.

Continuity Equation. Consider the control volume shown in Figure 2-6. The flow is from left to right and the level of the meniscus in the groove is assumed to vary linearly as a function of axial location, x. For this analysis, the area on either side of the

$$\dot{m}_e$$

$(\rho A V)$

$$(\rho A V) + \frac{\partial}{\partial x} (\rho A V) dx$$

dx

$+$
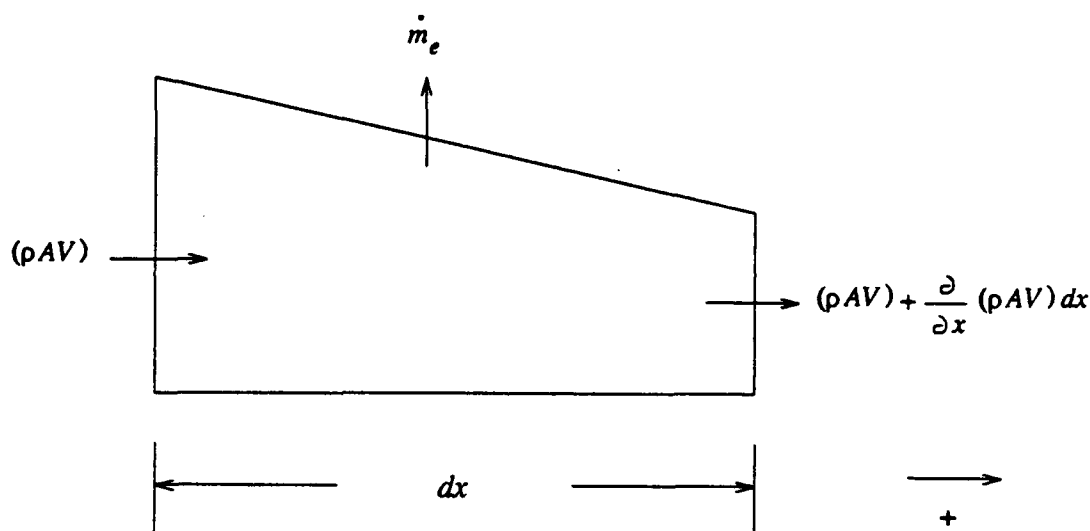
Figure 2-6. Control Volume for Liquid Continuity Analysis

control volume through which the liquid flows is assumed to include the liquid from the base of the groove up to and including the bottom of the meniscus, along with the liquid that forms the meniscus. This cross-sectional flow area is a function of axial location, x, and time, t.

Conservation of mass for this control volume requires that the sum of the time rate of change of mass within the control volume and the mass flow exiting the control volume minus the mass flow entering the control volume equal zero. Summing the flows and subtracting out similar terms yields the one-dimensional, unsteady continuity equation for this control volume

$$\frac{\partial(\rho \bar{A} dx)}{\partial t} + \frac{\partial(\rho A V)}{\partial x} dx + \dot{m}_e = 0 \qquad [2\text{-}4]$$

ρ is the liquid density, $\bar{A}$ is a simply-averaged area between the left and right ends of the control volume, V is the liquid velocity and $\dot{m}_e$ is the evaporative mass flow. Applying incompressibility, noting that $\bar{A} \rightarrow A$ as $dx \rightarrow 0$, and dividing by ρdx, Eqn [2-4] simplifies to

$$\frac{\partial A}{\partial t} + \frac{\partial(A V)}{\partial x} + \frac{\dot{m}_e}{\rho dx} = 0 \qquad [2\text{-}5]$$

The evaporative mass flow term is a function of the liquid temperature and a discussion of how it was determined is found in Chapter IV.

Momentum Equation. Figure 2-7 shows the same control volume with the appropriate forces (solid arrows) and momentum terms (dashed arrows). Conservation of momentum requires that the sum of the time rate of change of the momentum within the control volume and the momentum flow out of the control volume minus the momentum flow into the control volume equal the summation of all forces acting upon the control volume.

Summing the forces and flows and subtracting out similar terms yields the one-dimensional, unsteady momentum equation in Eqn [2-6]. P and P_v are the liquid and ambient pressures respectively, and V_e is the velocity with which the evaporative mass
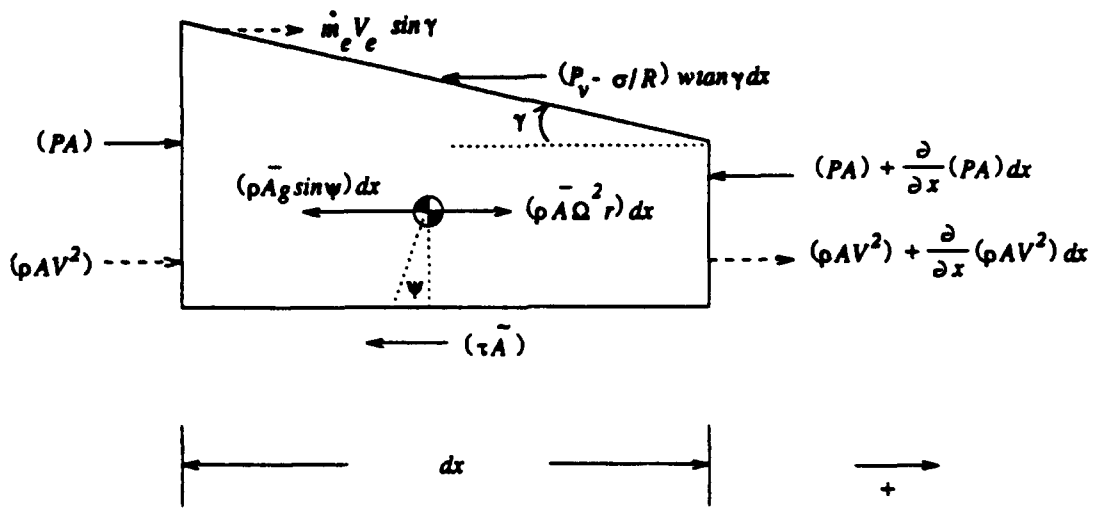
Figure 2-7. Control Volume for Liquid Momentum Analysis

$$\frac{\partial(\rho \bar{A} V dx)}{\partial t} + \frac{\partial(\rho A V^2)}{\partial x} dx + \dot{m}_e V_e \sin\gamma = -\frac{\partial(PA)}{\partial x} dx$$

$$- \rho \bar{A} g \sin\psi dx - (P_v - \frac{\sigma}{R}) w \tan\gamma dx - \tau \tilde{A} + \rho \bar{A} \Omega^2 r dx$$

[2-6]

flow leaves the control volume. This velocity was calculated using $V_e = \frac{\dot{m}_e}{\rho_e A_e}$, where ρ_e is the ethanol vapor density and A_e is the area over which the evaporation occurs. ψ is the groove tilt angle, defined positive when the evaporator end is raised, τ is the shear stress between the groove wall and the liquid and $\tilde{A}$ refers to the circumferential area of the control volume over which the shear acts. γ refers to the angle generated by the axial variation in meniscus level, Ω is the groove rotation rate and r is the axial distance from the center of rotation to any point in the liquid.

The last term on the right hand side of the Eqn [2-6] is a fictitious acceleration term that must be added to account for the fact that these equations of motion are written in a non-inertial reference frame.

The center of rotation of the groove structure was considered to be the inertial point of reference and this point was assumed to be stationary in an inertial reference frame. In the experiment, the center of rotation was not translating but only rotating with respect to this inertial reference frame.

According to White (44), the fictitious acceleration terms are

$$a = -\frac{d^2X}{dt^2} - \frac{d\Omega}{dt} \times r - \Omega \times (\Omega \times r) - \frac{d\overline{V}}{dt} - 2\Omega \times \overline{V}$$

where X is the distance between the inertial frame and the moving frame, $\overline{V}$ is the translational velocity of the moving frame and Ω and r are as described previously. Since X and $\overline{V}$ are zero in this particular experiment, the first, fourth and fifth terms above are zero. Term two is non-zero but its direction is perpendicular to the groove axis and therefore does not contribute to the liquid motion. This acceleration term acts to force liquid out of the groove in a direction perpendicular to the groove axis.

In order to neglect this term, its magnitude must be less than the acceleration due to gravity. This inequality is given by $|\dot{\Omega}r| < g$, where $\dot{\Omega} = \frac{d\Omega}{dt}$. Solving this inequality in terms of $\dot{\Omega}$ results in $|\dot{\Omega}| < \frac{g}{r_{max}}$, where r_{max} is the maximum length of the capillary structure. This last inequality provides a limit to the motions that may be analyzed with this new model.

Consider sinusoidal groove motion given by $\psi = \psi_{max}\sin(2\pi\omega t)$, where ψ_{max} is the maximum amplitude of the motion and ω is the frequency of rotation. This motion was used for the numerical experiments of this study. Differentiating this last expression twice with respect to time provides $\dot{\Omega}$ which is $\dot{\Omega} = -4\pi^2\omega^2\psi_{max}\sin(2\pi\omega t)$. Substituting

2-12

this result into the inequality above, noting that the maximum value of $\sin(2\pi\omega t)$ is one, and solving for the frequency results in the following inequality, $\omega^2 < \dfrac{g}{4\pi^2 \psi_{max} r_{max}}$.

This inequality was plotted and the result is seen in Figure 2-8. This figure shows the maximum allowed frequency for a given maximum amplitude for the motion
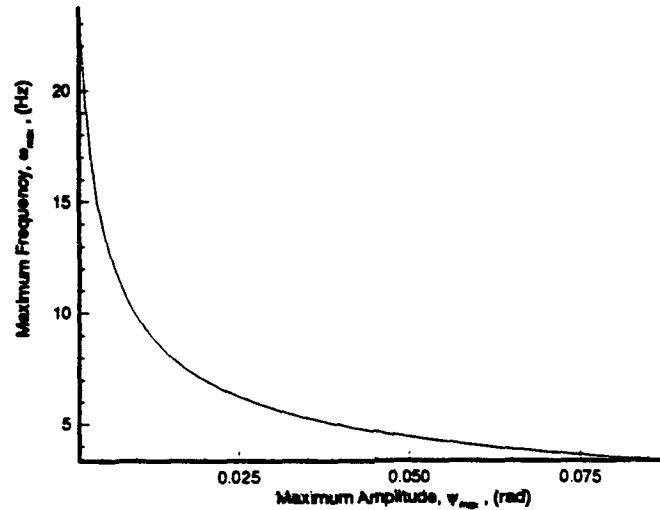
Figure 2-8. Frequency vs. Amplitude Limit for Numerical Experiments

described above. The length of the groove, r_{max} , is 0.254 m and the gravitational constant, g , is 9.81 m/s^2. As long as the combination of frequency and amplitude lie below the limit line, the assumption that the out of plane acceleration term has no influence on the liquid flow is valid. This curve only applies to the sinusoidal motion described above. Since all of the numerical work in this study was performed within the limit described above, the $\left(\dfrac{d\Omega}{dt} \times r \right)$ term was neglected.

The only contribution to the liquid motion therefore, comes from the $\Omega^2 r$ term. It is important to note that this result is only valid for this experiment; those terms

2-13

neglected in this analysis may appear in other analyses depending on the environment in which the capillary structure is placed.

The resulting form of the momentum equation, after dividing Eqn [2-6] by the constant, ρdx, yields

$$\frac{\partial(AV)}{\partial t} + \frac{\partial}{\partial x}(AV^2 + \frac{PA}{\rho}) = -\frac{\dot{m}_e V_e \sin\gamma}{\rho dx} - Ag\sin\psi$$

$$-\frac{\tau\bar{A}}{\rho dx} - \frac{1}{\rho}(P_v - \frac{\sigma}{R})w\tan\gamma + A\Omega^2 r$$

[2-7]

Pressure. The liquid pressure at any location along the groove is defined as the sum of the capillary pressure and the average pressure generated by the height of liquid in the groove at that location. This is seen by referring to the groove structure inclined at an angle ψ in Figure 2-9.
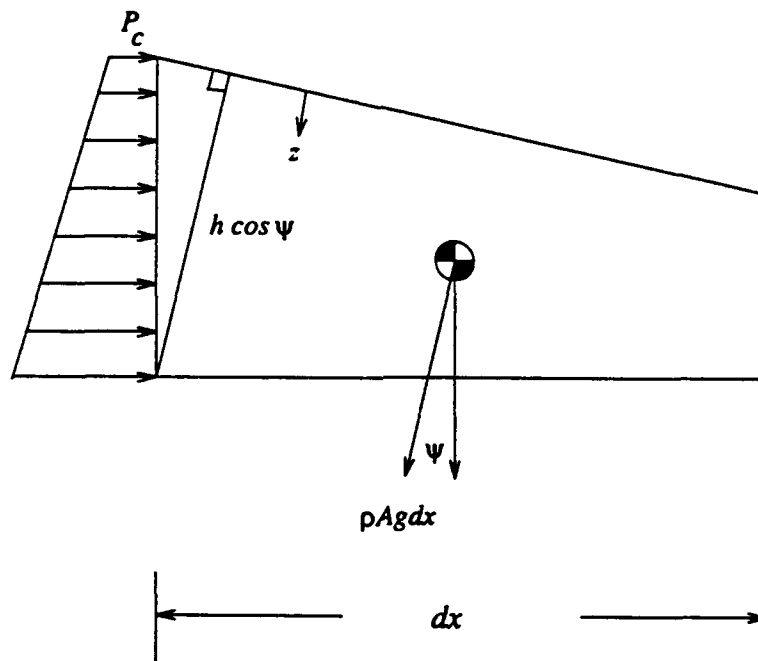
Figure 2-9. Control Volume for Derivation of Hydrodynamic Pressure

In general, the liquid pressure in the groove, P, is defined as,

$$P = \frac{1}{A} \int_A P(z) \, dA \qquad \text{[2-8]}$$

A, the cross-sectional flow area, is approximated by $A = wh$, where h is the average height of the liquid in the groove. From the figure, A may also be written as

$$A = \frac{w\hat{h}}{\cos \psi} \qquad \text{[2-9]}$$

where $\hat{h} = h \cos \psi$. Substituting Eqn [2-9] into Eqn [2-8] results in

$$P = \frac{1}{\hat{h}} \int_0^{\hat{h}} P(z) \, d\hat{h} \qquad \text{[2-10]}$$

With z as shown in Figure 2-9, the pressure at any z location, measured from the meniscus down to the bottom of the groove, is

$$P(z) = P_c + \rho g z \qquad \text{[2-11]}$$

where P_c is the capillary pressure. Substituting Eqn [2-11] into Eqn [2-10] and integrating yields the average liquid pressure in the groove as

$$P = P_c + \rho g \bar{h} \qquad \text{[2-12]}$$

where $\bar{h} = 0.5 \hat{h}$.

The capillary pressure has already been discussed. Recession of the meniscus into the groove structure reduces the liquid pressure from ambient pressure by an amount equal to σ/R. R, the radius of curvature of the meniscus, is a geometric quantity and is found in the following manner.

If the groove is entirely full, then the radius of curvature approaches infinity. As liquid is removed from the groove, the meniscus begins to recede and the radius of curvature begins to decrease from infinity to a value equal to one-half the groove width

2-15

when the meniscus is fully formed. From this point, any further decrease in the liquid inventory causes the meniscus to fall within the groove structure but not change from its fully formed shape. This behavior is assumed to be true until the liquid inventory reaches a state such that the bottom of the meniscus is tangent to the bottom of the groove.

When the meniscus is fully formed it is generally accepted that the capillary pumping has reached its maximum. In the Hawthorne work (27), experimental observations of the dryout and rewet behavior of an ethanol front in a 1 mm rectangular copper groove heated from below were made. Hawthorne observed that the front (liquid inventory sufficient for the meniscus to be tangent to the bottom of the groove) was well-defined and its position recordable. In addition to the front, liquid spikes were visible that extended forward of the front on either side and the ethanol in these spikes remained concentrated in the corners of the groove. These spikes also appeared to be pumping or pulling ethanol from the bulk of liquid behind the front. The shape and behavior of these spikes was different depending on whether the groove was drying out or rewetting. The fact that these spikes appeared to be pumping liquid at all indicated that the radius of curvature decreased beyond the generally accepted minimum value for a groove and that additional capillary pumping was possible. Similar observations were noted by this author on a groove structure with dimensions identical to the groove used in this work.

It is therefore assumed that as the liquid inventory depletes beyond the tangent condition described above, the remaining liquid recedes into the corners of the groove and the radius of curvature continues to decrease until the point that the pressure decrease caused by the capillary action causes a negative liquid pressure.

Radius of Curvature. Figure 2-10 shows the various meniscus levels within the groove structure and defines three critical areas. The first critical area, A_{c1}, occurs

$A_{c1} = w\delta$

$A_{c2} = w\delta - 0.5\pi(w/2)^2$

$A_{c3} = 0.125w^2(4 - \pi)$

δ

w
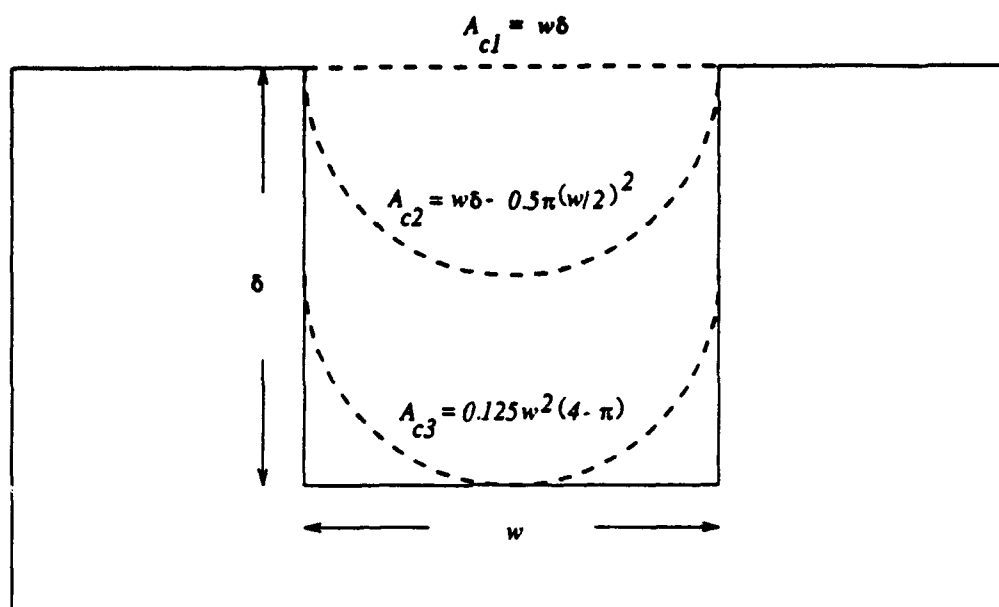
Figure 2-10. Critical Meniscus Levels for a Square Groove

when the groove is entirely full and its value is simply $A_{c1} = w\delta$ with a corresponding infinite radius of curvature.

The second critical area, A_{c2}, corresponds to the point at which the meniscus first becomes fully formed. At this point, the radius of curvature is $w/2$ and the critical area is $A_{c2} = w\delta - 0.5\pi(w/2)^2$.

The sector area between A_{c1} and A_{c2}, termed A_{sec}, is calculated knowing the radius of curvature and the groove width by

$$A_{sec} = R^2 \sin^{-1}\left(\frac{w}{2R}\right) - \frac{w}{2}\left(R^2 - \frac{w^2}{4}\right)^{1/2} \qquad [2\text{-}13]$$

Eqn [2-13] is a transcendental equation and may not be solved for R in terms of w and A_{sec}. However, given a range of R values, a corresponding list of non-dimensional cross-sectional flow areas (A/A_{c1}) can be calculated and plotted. The resulting curve is seen in

2-17

Figure 2-11 and this curve was curve-fit to provide a more useful relationship between A_{soc} and R. A tenth order natural log polynomial curve-fit of the form

$$R = \frac{w}{2 *} \qquad * = \sum_{i=0}^{i=10} C_i \left[\ln \left(\frac{A}{A_{cl}} \right) \right]^i \qquad [2\text{-}14]$$

with coefficients given in Table 2-1 provides errors of less than 0.04 percent at all areas between A_{cl} and A_{c2} . The natural log polynomial fit was chosen over a simple polynomial fit because it provided the best correlation with the data.
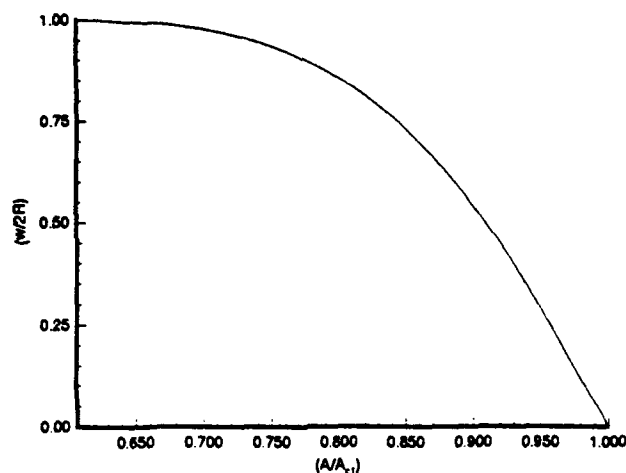
Figure 2-11. Radius of Curvature vs. Cross-Sectional Flow Area in a Square Groove

The third critical area, A_{c3} , occurs when the meniscus is tangent to the bottom of the groove. This is equal to a cross-sectional flow area of $A_{c3} = 0.125 w^2 (4 - \pi)$ and a radius of curvature equal to $w/2$. As the cross-sectional area decreases beyond A_{c3} , the radius of curvature also decreases. Its value is found as a function of the remaining cross-sectional flow area as

Table 2-1. Curve-fit Coefficients for 10th Order Natural Log Polynomial Fit to Radius of Curvature vs. Cross-Sectional Flow Area for a Square Groove

C_0	3.05395E-08
C_1	-6.0002
C_2	-3.0324
C_3	61.972
C_4	48.415
C_5	-1483.4
C_6	-8296.2
C_7	-22364.
C_8	-34471.
C_9	-29195.
C_{10}	-10583.

$$R = \left(\frac{2A}{4-\pi} \right)^{1/2} \qquad [2\text{-}15]$$

This additional decrease in radius of curvature is allowed to continue until the minimum allowable liquid pressure occurs.

In summary, the liquid pressure in the groove at any axial location is strictly a function of the ambient pressure, the groove geometry and tilt, the cross-sectional flow area and the liquid properties and is given by

$$P = P_v - \frac{\sigma}{R} + \rho g \bar{h} \qquad [2\text{-}16]$$

where R is a function of the cross-sectional flow area and $\bar{h}$ is a function of the cross-sectional flow area and the groove tilt.

Shear Stress. The shear force between the liquid and the groove wall must be modeled in order to solve the momentum equation. According to Chi (41), its value is calculated in a manner similar to classic pipe flow theory, but with modifications to

account for the fact that the groove is not a tube but a channel. How the shear stress was modeled in this work is now presented.

From the assumptions, the flow in the groove is laminar at all times. With this assumption, the (f·Re) product is calculated using the following equation from Shah (45)

$$(f \cdot Re) \approx 24.0 \, (\, 1 - 1.3553\alpha^* + 1.9467\alpha^{*^2} - 1.7012\alpha^{*^3} +$$
$$0.9564\alpha^{*^4} - 0.2537\alpha^{*^5} \,)$$

[2-17]

where α^* is the groove aspect ratio defined as $\alpha^* = w/\delta$ and Re is the Reynolds Number based on the hydraulic diameter, D_h, where $D_h = 2w\delta/(w+\delta)$. Eqn [2-17] is a curve-fit to experimental data and is valid to within 0.05 percent (45).

To account for the fact that the flow in the groove is really flow in an open channel, a modification to Eqn [2-17] is made. Chi (41) recommends using Eqn [2-17], but with a modified aspect ratio equal to the groove width divided by twice the wetted groove height. The Reynolds Number form is the same but the hydraulic diameter is recalculated using $D_h = 4w\delta/(w+2\delta)$. This results in an overall increase in the (f·Re) factor from the smooth tube value. With the channel friction factor determined, the shear stress is calculated using

$$\tau = \frac{f\rho V^2}{2}$$

[2-18]

Energy Equation. Figure 2-12 depicts the same control volume used to develop the mass and momentum equations with the appropriate energy terms, where free convection and radiation losses are assumed negligible. Conservation of energy states that sum of the time rate of change of energy within a control volume and the rate of energy exiting the control volume minus the rate of energy entering the control volume must

2-20
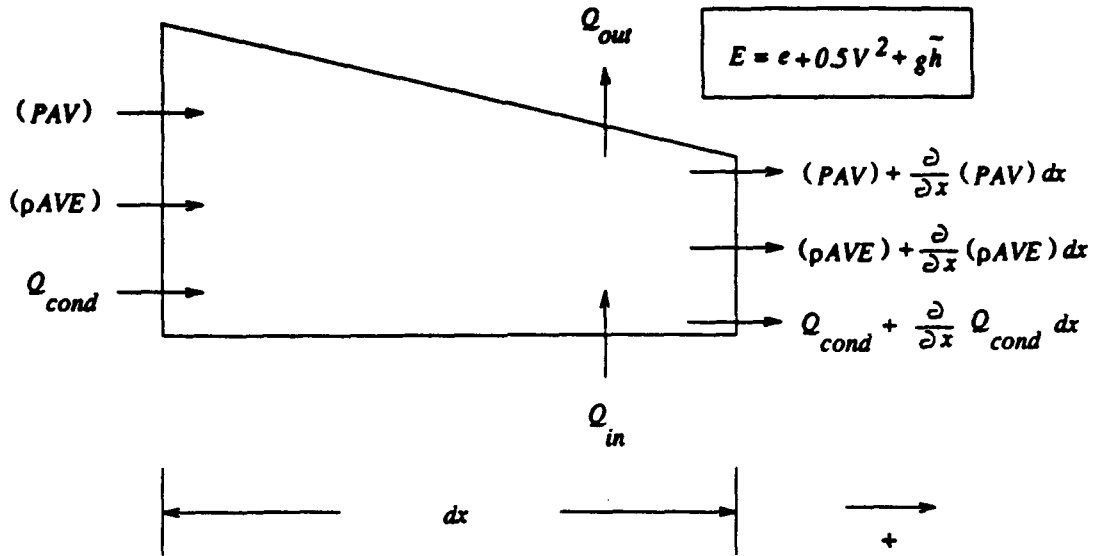
Figure 2-12. Control Volume for Liquid Energy Analysis

equal the sum of the rates at which heat is added to and work is performed on the control volume.

The one-dimensional, unsteady energy equation for the control volume above is

$$\frac{\partial}{\partial t}\left(\rho \bar{A} E\, dx\right) + \frac{\partial}{\partial x}\left(\dot{m} E + P A V\right) dx = (Q_{in} - Q_{out}) - \frac{\partial}{\partial x}(Q_{cond})\, dx \qquad \text{[2-19]}$$

where E is the total energy per unit mass which includes internal, kinetic and potential energies, $(Q_{in} - Q_{out})$ is the net change in energy in the control volume due to heat addition by convection from the groove wall and evaporation of the liquid, and Q_{cond} is the rate of energy transfer axially through the control volume due to conduction. Dividing out the constant $\rho\, dx$ term, Eqn [2-19] simplifies to

$$\frac{\partial}{\partial t}(A E) + \frac{\partial}{\partial x}\left(A V\left[E + \frac{P}{\rho}\right]\right) = \frac{(Q_{in} - Q_{out})}{\rho\, dx} - \frac{1}{\rho}\frac{\partial Q_{cond}}{\partial x} \qquad \text{[2-20]}$$

2-21

Total Energy. The total energy term includes internal, kinetic and potential energies and is written as

$$E = c_p T + \frac{V^2}{2} + g \tilde{h} \qquad \text{[2-21]}$$

where c_p is the specific heat, T is the bulk liquid temperature and $\tilde{h}$ is the potential height of the liquid above some energy datum. However, since kinetic and potential energies have been neglected in this analysis, the total energy, per unit mass, of the liquid is approximated by $c_p T$.

$(Q_{in} - Q_{out})$. This term represents the net change of energy in the liquid due to heat addition and evaporation. Since free convection and radiation losses from the liquid to the surroundings are assumed negligible, this term represents the difference between the heat entering the control volume from the groove walls and the heat lost from the liquid due to evaporation.

The heat entering the liquid is modeled using Newton's Cooling Law

$$Q_{in} = h_{in} A_{in} (T_g - T) \qquad \text{[2-22]}$$

where A_{in} is the groove wall area across which the heat travels, T_g is the groove wall temperature and h_{in} is the heat transfer coefficient between the groove walls and the liquid. Because channel flow resembles internal flow more than external flow, the most appropriate temperature to use in the equation above is the bulk liquid temperature (46). The groove temperature is a boundary condition to the set of governing equations and is an experimentally measured quantity. A discussion of how it was obtained is found in Chapter IV.

Convection correlations for laminar flow in rectangular tubes are used to model the heat transfer coefficient, h_{in} , in Eqn [2-22] . The variation of Nusselt Number with groove aspect ratio is shown in Figure 2-13 (46). The curve in Figure 2-13 is valid for

a constant surface heat flux and Prandtl Numbers greater than 0.6. Since Prandtl Numbers for ethanol over the temperature range of this work are approximately 15, this correlation is considered acceptable (43).
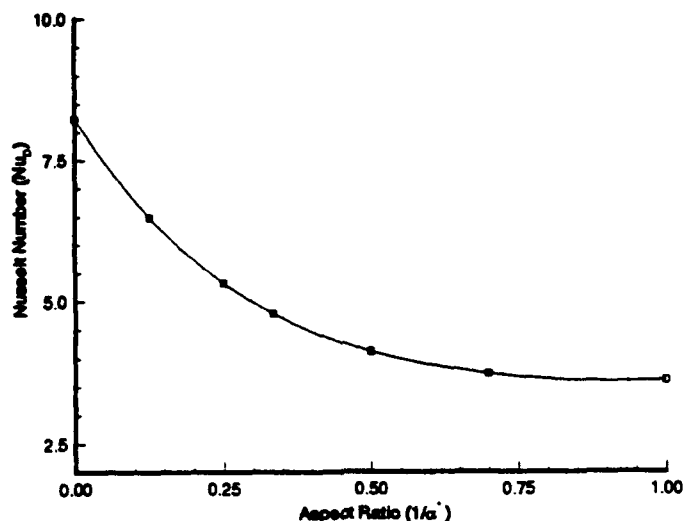
Figure 2-13. Nusselt Number Variation for Rectangular Groove--Constant Surface Heat Flux

To account for open channel flow, a modified aspect ratio--equal to the groove width divided by twice the wetted groove height--is used in Figure 2-13. This is similar to the modified aspect ratio used in the shear stress calculation. The heat transfer coefficient is then calculated using

$$h_{in} = \frac{Nu \; k}{D_h} \qquad [2\text{-}23]$$

where k is the liquid thermal conductivity and D_h is the hydraulic diameter.

The rate of energy exiting the liquid, Q_{out}, is related to the evaporative mass flow by the latent heat, λ. The evaporative mass flow, along with the latent heat, are both

functions of temperature. Evaporative mass flow as a function of temperature was determined experimentally and is presented in Chapter IV.

The net change in energy to the control volume is the difference between the rate of energy entering and the rate of energy exiting and is written as

$$(Q_{in} - Q_{out}) = h_{in} A_{in} (T_s - T) - \dot{m}_e \lambda \qquad [2\text{-}24]$$

Q_{cond} . This term represents the amount of energy transferred axially through the liquid by conduction and its magnitude is given by

$$Q_{cond} = -kA \frac{\partial T}{\partial x} \qquad [2\text{-}25]$$

Eqns [2-5], [2-7] and [2-20] form the governing equations for liquid flow in the groove structure for the proposed model with Eqns [2-14] through Eqn [2-16] providing closure for the system. Together, these equations take into account body forces, inertia effects, evaporation, shear stress between the liquid and the groove wall, and varying meniscus heights. These variables were either neglected or oversimplified in previous models.

Energy Decoupling

There are three equations and three unknowns; the three equations are continuity, momentum and energy and the unknowns are cross-sectional flow area, liquid velocity and bulk liquid temperature. All of the other variables in these equations are either constants, known functional relationships, experimentally determined values or are rewritten in terms of the unknown variables. The only thing left to decide is whether to solve a 3 x 3 matrix system consisting of the three equations above, or to try to decouple the energy equation from continuity and momentum and solve the resulting 2 x 2 system; a savings in computing resources.

In order to decouple energy from continuity and momentum, no relationship between density, pressure and temperature within the liquid can exist. Incompressibility immediately removes any dependence density may have with pressure and temperature. It is only necessary to show that pressure and temperature are independent variables.

By assuming the liquid to be incompressible, the only reversible means of changing its internal energy is by adding or removing heat. According to the state postulate, then, only one independent thermodynamic property is required to fully define the state and for this work that property is temperature (internal energy or entropy could also have been selected). Incompressibility removes compression as a means of changing the internal energy of the liquid and therefore, pressure becomes a purely mechanical variable and no thermodynamic significance may be attached to it (47). Therefore, pressure and temperature are independent properties and the energy equation may be decoupled from continuity and momentum equations and solved separately.

Alternately, consider the continuity and momentum equations; there are two equations and three unknowns; namely, the area, velocity and pressure. However, the pressure is a function of the flow area and hence, once the area is known, the pressure is also known. This leaves two equations and two unknowns and the system may be solved independent of the energy equation. This is not analogous to the compressible gas dynamic equations where pressure is related to temperature. This pressure-temperature relationship is what causes the coupling between continuity, momentum and energy in the gas dynamic case and forces a solution of a 3 x 3 system of equations. Since pressure and temperature are not dependent properties in this problem, a 2 x 2 system may be solved independent of any energy considerations.

Non-Dimensionalization

The continuity and momentum equations are rewritten in a form that is more conducive to solution by established numerical methods; namely, a non-dimensional matrix equation containing temporal and spatial derivative terms, along with a forcing function. This essentially treats the system of equations as Euler-type (non-viscous) and handles the viscous and body force terms as source terms. This makes the resulting system hyperbolic, not the mixed elliptic-parabolic system one might expect in an incompressible viscous solution (48). The one-dimensionality of this problem prevents formation of the second order terms that give rise to the elliptic-parabolic nature of the incompressible, viscous Navier-Stokes equations. However, as long as the source term containing the shear and body force elements is modeled properly, no difficulty is expected. The final test will be in the match of the theory to experiment.

The following definitions were used to non-dimensionalize the equations; * refers to the non-dimensional value

$$A^*=A/A_{cl} \qquad\qquad V^*=V/V_\infty$$

$$x^*=x/L_\infty \qquad\qquad t^*=t/t_\infty$$

$$P^*=P/(\rho_\infty V_\infty^2) \qquad \rho^*=\rho/\rho_\infty$$

L_∞ is the overall length of the groove, t_∞ is the total run time (a constant) for any particular experiment, V_∞ is the characteristic velocity given by $V_\infty = L_\infty/t_\infty$ and ρ_∞ is the liquid density. Note that ρ^* is unity using these definitions.

These non-dimensional variables are substituted into the continuity and momentum equations and the resulting system is written as

$$\frac{\partial \bar{U}}{\partial t} + \frac{\partial \bar{E}}{\partial x} = \{M\}\bar{S} \qquad\qquad [2\text{-}26]$$

where {M} is a multiplier matrix. Combining the equations, the individual matrices become,

$$\bar{U} = \begin{bmatrix} A^{\bullet} \\ A^{\bullet}V^{\bullet} \end{bmatrix}$$

$$\bar{E} = \begin{bmatrix} A^{\bullet}V^{\bullet} \\ A^{\bullet}V^{\bullet 2} + \dfrac{P^{\bullet}A^{\bullet}}{\rho^{\bullet}} \end{bmatrix}$$

$$\{M\} = \begin{bmatrix} \dfrac{t_{\infty}}{A_{cl}} \\[2mm] \dfrac{t_{\infty}}{A_{cl}V_{\infty}} \end{bmatrix} \qquad \bar{S} = \begin{bmatrix} -\dfrac{\dot{m}_{e}}{\rho\, dx} \\[3mm] -\dfrac{\dot{m}_{e}V_{e}\sin\gamma}{\rho\, dx} - A g\sin\psi - \dfrac{\tau \tilde{A}}{\rho\, dx} - \dfrac{1}{\rho}(P_{v} - \dfrac{\sigma}{R})w\tan\gamma + A\Omega^{2}r \end{bmatrix}$$

The solution of Eqn [2-26] provides the cross-sectional flow area and velocity of the liquid in the groove as a function of location and time. These results are then used to solve the energy equation. How the matrix system is solved, along with the treatment of the boundary conditions, is the subject of Chapter III.

III. *Numerical Solution*

The solution of Eqn [2-26] requires a numerical scheme capable of integrating a hyperbolic system of non-linear equations. The choice between explicit and implicit schemes is essentially a matter of preference. Explicit schemes are generally easier to program but suffer from small timestep restrictions in order to preserve numerical stability. This generally leads to excessive computational requirements. Implicit schemes are usually quicker and provide unconditional stability; however, the programming of these schemes can sometimes be cumbersome. The purpose of this chapter is to describe the numerical scheme used in this work and lay the theoretical foundation for its use. Additionally, a discussion of how the scheme is implemented and how the boundary conditions are updated is provided.

Numerical Scheme

The numerical scheme used was an explicit method proposed by Roe (49). It is an approximate Riemann solver that is first-order accurate in time and space. The overbar representation of vectors and matrices used in Chapter II is neglected for brevity. Vectors and matrices are represented by capital letters. Where necessary, a short discussion is provided to differentiate between vector, matrix and scalar quantities. Except where noted, subscripts refer to node locations and superscripts refer to time levels.

Linear, Coupled Systems. Consider the following system of linear, coupled equations described by

$$U_t + J U_x = S \qquad \text{[3-1]}$$

U is a column vector of dimension n and J is a (n x n) matrix with real eigenvalues, λ_i. The t and x subscripts refer to time and space derivatives respectively.

3-1

This coupled system can be uncoupled by diagonalizing the matrix J through a similarity transformation. If it is assumed that J has only real eigenvalues, then there exists a matrix R, such that $R^{-1}JR = \Lambda$, where Λ is a diagonal matrix with the eigenvalues of J as its elements, and R is composed of the right eigenvectors of J. By letting $W = R^{-1}U$, such that $U = RW$, then Eqn [3-1] may be rewritten as

$$W_t + \Lambda W_x = R^{-1}S$$

Following the work of Yee (50), the solution of the equation above is

$$W_i^{n+1} = W_i^n - \frac{\nu}{2}\Lambda(W_{i+1}^n - W_{i-1}^n) + \frac{\nu}{2}|\Lambda|(W_{i+1}^n - 2W_i^n + W_{i-1}^n) + \Delta t R^{-1}S_i^n \qquad [3\text{-}2]$$

where ν is the Courant number defined as $\nu = \Delta t/\Delta x$, and $|\Lambda|$ is a (n x n) diagonal matrix such that

$$|\Lambda|_{ij} = 0 \qquad (i \neq j)$$

$$|\Lambda|_{ii} = |J_i| \qquad (i = 1,2,\ldots,n)$$

Transforming Eqn [3-2] back to the original variables yields

$$U_i^{n+1} = U_i^n - \frac{\nu}{2}J(U_{i+1}^n - U_{i-1}^n) + \frac{\nu}{2}\bar{J}(U_{i+1}^n - 2U_i^n + U_{i-1}^n) + \Delta t S_i^n \qquad [3\text{-}3]$$

where $\bar{J} = R|\Lambda|R^{-1}$. Defining a numerical flux function as

$$H_{i+1/2}^n = \frac{1}{2}\left[J(U_{i+1}^n + U_i^n) - \bar{J}(U_{i+1}^n - U_i^n)\right]$$

and noting that this flux function is evaluated at cell interfaces (i.e., {i+1/2}, {i-1/2} locations), Eqn [3-3] may be rewritten as

$$U_i^{n+1} = U_i^n - \nu(H_{i+1/2}^n - H_{i-1/2}^n) + \Delta t S_i^n$$

Non-Linear, Coupled Systems. The Roe scheme is applied to a system of non-linear, coupled equations in a manner similar to that described above. Consider the system of equations given by

$$U_t + E_x = S \qquad\qquad [3\text{-}4]$$

where the non-linearity arises because $E = E(U)$. There is no restriction on S at this point; therefore, it is acceptable for $S = S(U)$. This is identical in form to Eqn [2-26] and its solution procedure, outlined in (51), is now summarized.

The first step in the solution process is to linearize Eqn [3-4]. This is done by defining a mean-value Jacobian matrix, $\hat{J}$, such that

$$U_t + \hat{J} U_x = S \quad ; \quad \hat{J} = \left.\frac{\partial E}{\partial U}\right|_{i \pm 1/2}$$

This definition of $\hat{J}$ is similar to the classic definition of the Jacobian. The only difference is that the mean-value Jacobian is evaluated at the cell interfaces instead of at 'dividual nodes. A number of different methods for evaluating the mean-value are available. One is to take a simple average of the Jacobians at neighboring points;

$$\hat{J}_{i+1/2} = \frac{1}{2}(J_i + J_{i+1})$$

another is to directly calculate the mean-value based on the interpolation of U;

$$\hat{J}_{i+1/2} = J_i((U_i + U_{i+1})/2)$$

The first of these methods is used in this work.

The second step is to define a modified flux function, which is given as

$$H_{i+1/2}^n = \frac{1}{2}(E_{i+1}^n + E_i^n - (\hat{R}_{i+1/2} \mid \hat{\Lambda}_{i+1/2} \mid \hat{R}_{i+1/2}^{-1})^n (U_{i+1} - U_i^n)) \qquad\qquad [3\text{-}5]$$

$\hat{R}$ is the matrix composed of the right eigenvectors of $\hat{J}$, and $\hat{\Lambda}$ is the diagonal matrix composed of the eigenvalues of $\hat{J}$. The Roe scheme, then, for the non-linear system of coupled equations given by Eqn [3-4] is

$$U_i^{n+1} = U_i^n - \nu(H_{i+1/2}^n - H_{i-1/2}^n) + \Delta t S_i^n \qquad \text{[3-6]}$$

The flux functions, H, are given by Eqn [3-5].

Jacobian Matrix. Recall from Chapter II that the matrices U and E are,

$$U = \begin{bmatrix} A \\ AV \end{bmatrix}$$

$$E = \begin{bmatrix} AV \\ AV^2 + \dfrac{PA}{\rho} \end{bmatrix}.$$

Note that these are the dimensional forms of the matrices. The remainder of this discussion will utilize the dimensional forms to enhance the understanding; the actual code uses the non-dimensional forms.

In order to determine the Jacobian, the E matrix needs to be written in terms of the primitive variables within U. Defining $U_1 = A$, $U_2 = AV$, then clearly, the first element within E, termed E_1 , is U_2 . The second element within E, termed E_2 , requires slightly more manipulation to put it in the correct form. (AV^2) is easily written as (U_2^2/U_1); however, (PA/ρ) requires the pressure to be written in terms of U_1 and U_2 . From Chapter II, the liquid pressure is defined by Eqn [2-16]. With this, (PA/ρ) is written in terms of the primitive variables as

$$\frac{PA}{\rho} = \frac{P_v U_1}{\rho} - \frac{\sigma U_1}{\rho R} + \frac{g U_1^2}{2w}\cos\psi$$

Note the radius of curvature, R, in the above equation is a function of U_1 . E_2 is therefore

$$E_2 = U_2^2 U_1^{-1} + \frac{P_v U_1}{\rho} - \frac{\sigma U_1}{\rho R} + \frac{g U_1^2}{2w}\cos\psi$$

The Jacobian for the E matrix is composed of four elements whose values are determined by differentiating each element of E by the primitive variables within U. In other words

$$J_{m,n} = \frac{\partial E_m}{\partial U_n} \quad ; \quad m = 1,2 \quad n = 1,2$$

Performing the required differentiation, the Jacobian matrix, J, is

$$J = \begin{bmatrix} 0 & 1 \\ \left(-V^2 + \dfrac{P_v}{\rho} - \dfrac{\sigma}{\rho R} + \dfrac{\sigma A}{\rho R^2}\dfrac{\partial R}{\partial A} + \dfrac{gA}{w}\cos\psi \right) & 2V \end{bmatrix} \qquad \text{[3-7]}$$

Eigenvalues. Once the Jacobian matrix is known, the determination of the eigenvalues is straightforward. By defining a new variable, c, such that

$$c^2 = \frac{P_v}{\rho} - \frac{\sigma}{\rho R} + \frac{\sigma A}{\rho R^2}\frac{dR}{dA} + g\bar{h}$$

where $\bar{h}$ is defined in Chapter II, then the eigenvalues for the Jacobian matrix given above are

$$\lambda_1 = V - c \qquad\qquad \lambda_2 = V + c$$

Eigenvectors. With the eigenvalues, the eigenvectors can be determined. While not trivial, the procedure is relatively straightforward. A solution of the following vector equation is sought

$$\begin{bmatrix} -\lambda_i & 1 \\ c^2 - V^2 & 2V - \lambda_i \end{bmatrix} \bar{\xi}_i = 0 \quad ; \quad i = 1,2$$

where $\bar{\xi}_i$ are the (2 x 1) eigenvectors corresponding to the eigenvalues, λ_i. Performing the required math, the eigenvectors are

$$\xi_1 = \left\{ \frac{-c-V}{c^2-V^2}, 1 \right\}^T \qquad \xi_2 = \left\{ \frac{c-V}{c^2-V^2}, 1 \right\}^T$$

With the eigenvalues, the diagonal matrix, Λ, is formed, and with the corresponding eigenvectors, the matrix R is constructed. This provides all the required information to solve Eqn [3-6].

Stability. A complete treatment of the numerical solution to the problem at hand requires an investigation of the stability requirements. These requirements dictate the magnitude of the timestep that can be used during the numerical solution of the problem.

Using Eqn [3-4] as the baseline and assuming that E and S can be written as

$$E = J \frac{\partial U}{\partial x} \ ; \ J = \frac{\partial E}{\partial U}$$

$$S = BU \quad ; \ B = \frac{\partial S}{\partial U}$$

then Eqn [3-6] is expanded to yield

$$U_i^{n+1} = U_i^n - \frac{\nu}{2} \left[E_{i+1}^n - E_{i-1}^n \right]$$

$$+ \frac{\nu}{2} \left[|J|_{i+1/2}^n (U_{i+1}^n - U_i^n) - |J|_{i-1/2}^n (U_i^n - U_{i-1}^n) \right] + \Delta t B_i^n U_i^n$$

[3-8]

In order to linearize the flux terms, Taylor series expansions to second order accuracy about the point i are utilized to obtain

$$E_{i+1}^n - E_{i-1}^n \approx J_i^n U_{i+1}^n - J_i^n U_{i-1}^n$$

and substituting this into Eqn [3-8] yields

$$U_i^{n+1} = U_i^n - \frac{\nu}{2} \left[J_i^n (U_{i+1}^n - U_{i-1}^n) \right] + \frac{\nu}{2} \left[|J|_{i+1/2}^n (U_{i+1}^n - U_i^n) - |J|_{i-1/2}^n (U_i^n - U_{i-1}^n) \right]$$

$$+ \Delta t B_i^n U_i^n$$

This is the linearized form of the numerical scheme. A Fourier analysis is then applied directly to investigate the stability requirements.

When a Fourier component of the form $U_i^n = U^n e^{I\theta i}$, where $I = \sqrt{-1}$, is introduced into the equation above, extensive algebra is applied to show that the amplification factor, G, defined as $(\dfrac{U_i^{n+1}}{U_i^n})$, is

$$G = 1 - \frac{v}{2}\left[J_i^n(e^{i\theta} - e^{-i\theta})\right] + \frac{v}{2}\left[|J_{i+1/2}^n|(e^{i\theta} - 1) - |J_{i-1/2}^n|(1 - e^{-i\theta})\right] + \Delta t B_i^n$$

If it is further assumed that $|J_{i+1/2}^n| \approx |J_{i-1/2}^n| \approx |J_i^n|$, then the amplification factor can be written as

$$G = 1 + \Delta t B_i^n + |J_i^n| v(\cos\theta - 1) - IJ_i^n(\sin\theta)$$

For stability of any numerical scheme, it is required that $|G| \leq 1$, which, for the complex amplification factor above, results in

$$|1 + \Delta t B_i^n + |J_i^n| v(\cos\theta - 1)|^2 + |J_i^n v(\sin\theta)|^2 \leq 1$$

Multiplying this expression out and collecting like terms with respect to Δt and Δt^2, results in

$$\Delta t^2 B_i^2 + \Delta t 2 B_i(1 + |J_i^n| v(\cos\theta - 1)) + (\cos\theta - 1)\left[2|J_i^n| v - 2v^2 |J_i^n|^2\right] \leq 0$$

The most restrictive condition on this equation exists for $\theta = \pi/2$. Substitution and simplification yields the following timestep restriction

$$\Delta t \leq \left[\frac{2\Delta x |J_i| - 2B_i \Delta x^2}{B_i^2 \Delta x^2 - 2B_i \Delta x |J_i| + 2|J_i|^2}\right] \qquad [3\text{-}9]$$

Consider when the right-hand side of Eqn [3-4] approaches zero. This removes the forcing function and the resulting equation reduces to the one-dimensional, non-linear, inviscid Burger's Equation for which the stability requirement is (48)

3-7

$$\frac{\Delta t\,|J_i|}{\Delta x} \leq 1 \qquad\qquad\qquad \text{[3-10]}$$

By removing the forcing function, this sets B_i equal to zero in Eqn [3-9] and reduces the stability requirement to that given by Eqn [3-10]. For simplicity in the numerical portion of this work, Eqn [3-10] is used with a stability margin of 0.9 to calculate the required timestep. In other words

$$\Delta t \leq \frac{0.9\Delta x}{|J_i|}$$

Scheme Implementation

The following section explains how the Roe scheme was implemented in solving the groove problem with a discussion on how the boundary conditions were updated at the front.

In order to begin integrating in time, initial values of area, velocity and temperature for the liquid are required. This time level is denoted by n . The grid size at any time level is a constant and is I nodes wide. Since this work is one-dimensional, there are grid points in only one direction and the points are set up so they lie in the center of the control volumes as seen in Figure 3-1. The spacing is set up so that node 1 lies on the left boundary ($x^* = 0$) where the velocity is zero and the grid spacing is $\Delta x/2$. The grid extends to I nodes, some or all of which are wet, depending on the location of the front. This grid is referred to as GRID1. If the groove is entirely full of liquid at time level n , then nodes 1 through I are wet and a temporary boundary node, nb , is established and set equal to I. If, however, the groove is in a state of dryout or rewet, then the temporary node nb is the last node that has liquid in it and is equal to an
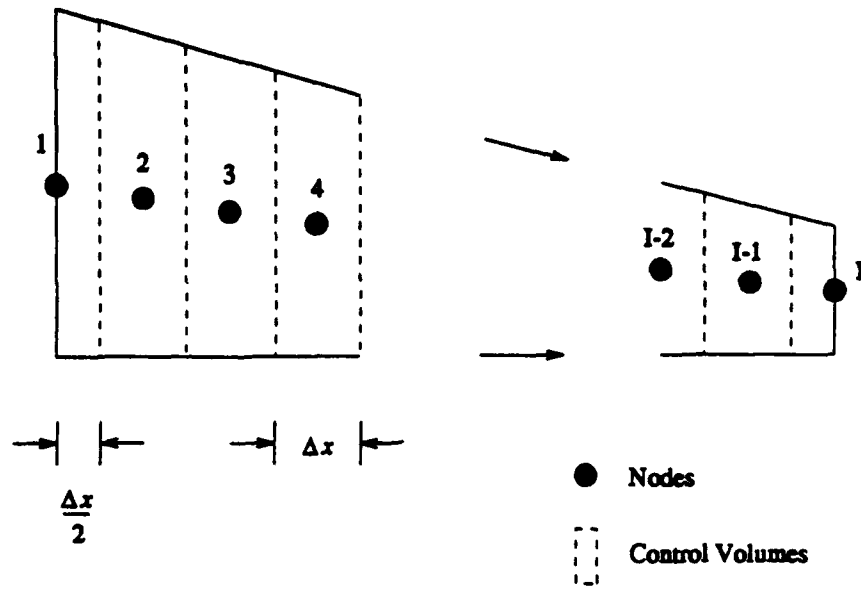
Figure 3-1. Grid Schematic--GRID1

integer value less than I. In fact, node *nb* always refers to the last wet node and moves with the liquid front.

There is an additional grid, seen in Figure 3-2, that is maintained such that the nodes form the ends of the individual control volumes. This grid is referred to as GRID2. This is done to facilitate updating of the boundary conditions. Node *nb* is still the last wet node and the mass within any control volume for GRID2 is given by

$$m_i^n = 0.5\rho (A_i^n + A_{i-1}^n)\Delta x \qquad ; \qquad i = 2, nb \qquad [3\text{-}11]$$

Note that control volume 1 is not defined using GRID2.

At time level *n*, the total mass of liquid in the groove, m_g^n, is known. At time level *n*+1, the total mass of liquid in the groove is

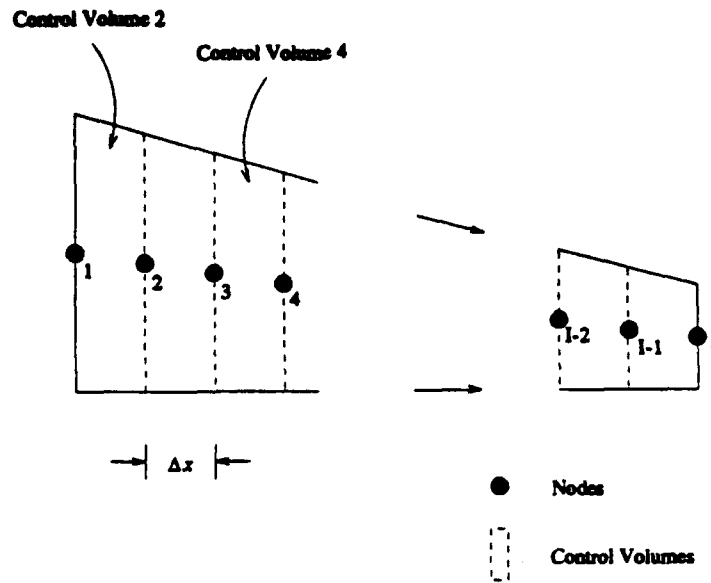$$m_g^{n+1} = m_g^n - \sum_{i=2}^{nb} \dot{m}_{e_i} \Delta t \qquad [3\text{-}12]$$

3-9

Figure 3-2. Grid Schematic--GRID2

where $\dot{m}_e$ is a function of the liquid temperature and is determined experimentally and discussed in Chapter IV. A positive value of $\dot{m}_e$ refers to evaporation.

The Roe scheme for a system of equations is applied to the continuity and momentum equations between nodes 2 and nb-1 only, using GRID1, and provides updated values of area and velocity at these nodes at time n+1.

A scalar version of the Roe scheme is used with GRID1 to integrate Eqn [2-20], the energy equation from Chapter II. The results of this integration provide values of temperature at nodes between 2 and nb-1 at time n+1. This scalar version of the Roe scheme is (51)

$$T_i^{n+1} = T_i^n - \Delta t \left[V_i^n \frac{T_{i+1}^n - T_{i-1}^n}{2\Delta x} - |V_i^n| \frac{T_{i+1}^n - 2T_i^n + T_{i-1}^n}{\Delta x^2} - S_i^n \right] \qquad [3\text{-}13]$$

where the source term is given by

$$S_i^{\,n} = \frac{\Delta Q_i^{\,n}}{\rho A_i^{\,n} c_p dx} - \frac{1}{\rho A_i^{\,n} c_p dx} \frac{\partial Q_{cond}^{\,n}}{\partial x} + \frac{V_i^{\,n} \Omega^2 r_i}{c_p} + \frac{T_i^{\,n}}{A_i^{\,n}} \frac{\dot{m}_{e_i}^{\,n}}{\rho dx} \qquad [3\text{-}14]$$

$\Delta Q_i^{\,n}$ in the equation above is defined as $\Delta Q_i^{\,n} = (Q_{in}^{\,n} - Q_{out}^{\,n})$. The mass in the control volumes between nodes 3 and nb-1 is updated using Eqn [3-11]. This sum of the internal masses is termed $m_{int}^{\,n+1}$. The only remaining calculations are updates of the area, velocity and temperature at the boundaries.

Using the left most control volume in Figure 3-2, the area of node 1 is calculated. Node 1 is the point around which the entire groove rotates and hence, it remains wet at all times throughout the transient. Applying conservation of mass to control volume 2 yields

$$m_2^{\,n+1} = m_2^{\,n} - \Delta t\,(\dot{m}_2^{\,n} + \dot{m}_e^{\,n})$$

$$\Rightarrow A_1^{\,n+1} = \frac{2 m_2^{\,n+1}}{\rho \Delta x} - A_2^{\,n+1} \qquad [3\text{-}15]$$

The velocity at node 1 is zero because of the physical boundary and the temperature is calculated assuming an adiabatic end condition, $\frac{\partial T}{\partial x}\big|_{x=0} = 0$.

With the mass in control volume 2 calculated, the remaining mass in the groove at time n+1 is

$$m_r^{\,n+1} = m_g^{\,n+1} - m_{int}^{\,n+1} - m_2^{\,n+1} \qquad [3\text{-}16]$$

This remaining mass occupies some specified volume extending from node nb on the right end of the groove. If the groove is not in a state of dryout, then the remaining mass occupies the last control volume. But, if the groove is exhibiting dryout or rewet, then a front exists and the remaining mass occupies a volume extending beyond node nb.

Several possibilities exists regarding the distribution of liquid to the right of node nb. Two of the more obvious are seen in Figure 3-3. The first order (or linear) volume
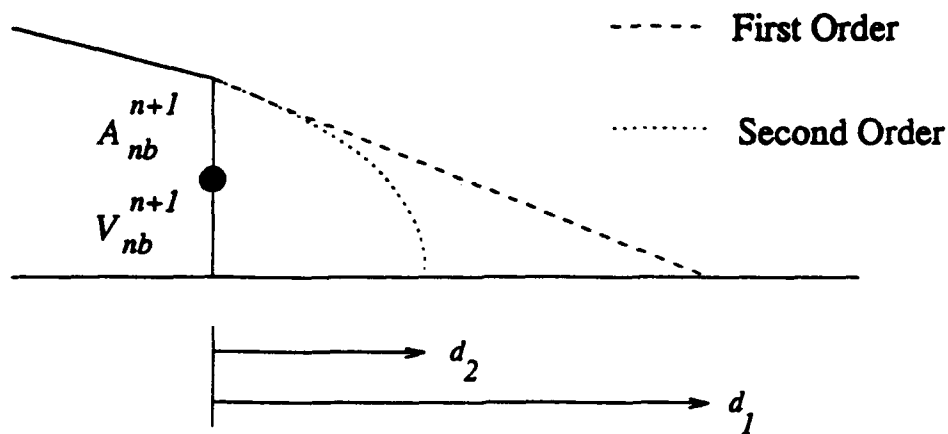
3-11

Figure 3-3. Sample Front Shapes Using First and Second Order Approximations

simply fills a right triangle with the remaining mass, while the second order (or parabolic) volume attempts to match a parabola with a specified slope at the front to the remaining mass. Higher order matches are also possible. For this work, the linear model was chosen.

Knowing the remaining mass, m_r, and the area at node nb, and assuming a linear distribution of mass beyond node nb, the distance between node nb and the front, d_1, is determined using

$$d_1 = \frac{2m_r}{\rho A_{nb}^{n+1}} \qquad [3\text{-}17]$$

This length can extend to the next node $nb+1$, or to several nodes beyond $nb+1$, or it may not even extend to node $nb+1$ depending on the amount of mass that remains. Defining the location in the groove where the cross-sectional flow area is zero as the

3-12

extinction point, d_{ep} , then the area at the extinction point is zero and the slope of the area distribution at the extinction point is $\frac{\partial A}{\partial x}\big|_{ep} = -\frac{A_{nb}^{n+1}}{d_{ep}}$. Rewriting d_{ep} in terms of the known variables, the area boundary conditions at the extinction point are

$$A_{ep} = 0$$

$$\left|\frac{\partial A}{\partial x}\right|_{ep} = \frac{-\rho\left(A_{nb}^{n+1}\right)^2}{2m_r}$$

[3-18]

If d_{ep} is less than Δx , then the remaining mass is not sufficient to extend the triangular profile to the next node. In this case, the area, velocity and temperature distribution of the liquid in the groove are completely defined and no further calculations of area, velocity or temperature are needed because there are no nodes extending beyond node nb .

If, however, d_{ep} is greater than Δx , then there is sufficient remaining mass to extend the profile to node $nb+1$. In this case, the area at node $nb+1$ is calculated using the area at node nb and the slope from Eqn [3-18]. In other words

$$A_{nb+1}^{n+1} = A_{nb}^{n+1} - \Delta x\left|\frac{\partial A}{\partial x}\right|_{ep}$$

[3-19]

Applying conservation of mass on the control volume between nodes nb and $nb+1$, shown in Figure 3-4 , yields the velocity at node $nb+1$ at time $n+1$ as

$$\frac{\partial(\rho\forall)}{\partial t} + \rho(AV)_{nb+1}^{n+1} - \rho(AV)_{nb}^{n+1} + \dot{m}_e^{n+1} = 0$$

$$\Rightarrow V_{nb+1}^{n+1} = \frac{(AV)_{nb}^{n+1} - \left(\frac{\partial\forall}{\partial t}\right)_{nb+1} - \frac{\dot{m}_e^{n+1}}{\rho}}{A_{nb+1}^{n+1}}$$
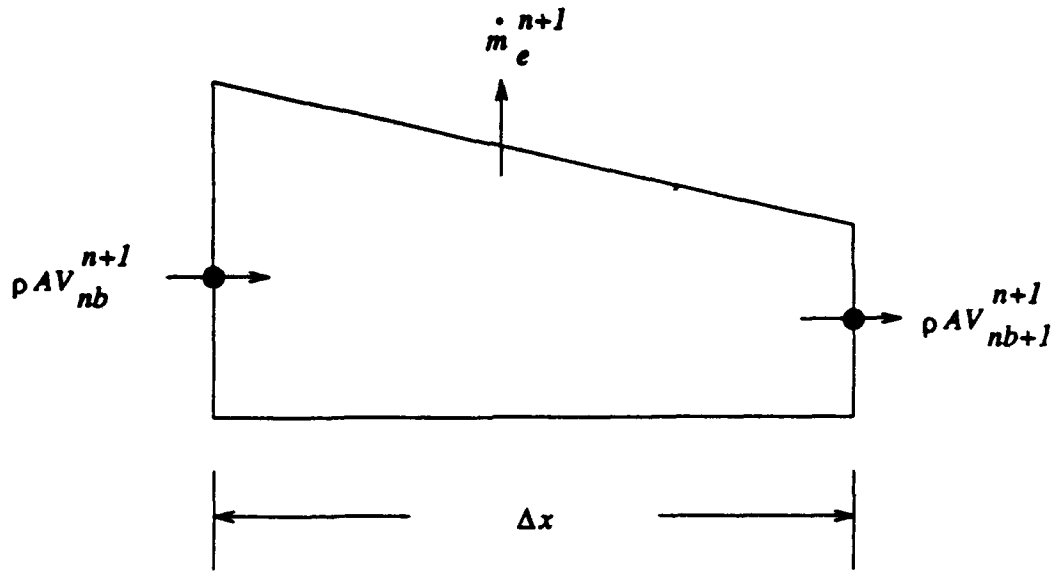
[3-20]

Figure 3-4. Control Volume $nb+1$ for Velocity Calculation

A first order approximation to the volume derivative, $\frac{\partial \forall}{\partial t}$, is used and the evaporation term is evaluated at the temperature of node nb at time level $n+1$. The temperature is updated assuming no axial conduction; in other words, $T_{nb+1}^{n+1} = T_{nb}^{n+1}$.

After the area, velocity and temperature at node $nb+1$ are updated, the mass in the control volume is calculated and subtracted from the original remaining mass, thereby providing a new remaining mass. Node $nb+1$, now the last wet node, is renumbered as node nb. With the new node and new mass, a new distance is calculated and the procedure described above is repeated until d_{ep} is less than Δx where the liquid distribution is completely defined.

A special case occurs when d_{ep} is greater than Δx but when node $nb+1$ is the boundary node, I. In this case, no front exists, and the area is calculated using

$$A_I^{n+1} = \frac{2m_r}{\rho \Delta x} - A_{ub}^{n+1} \qquad\qquad [3\text{-}21]$$

The velocity at node I is zero because of the physical boundary and the temperature is calculated using the adiabatic condition $T_I^{n+1} = T_{I-1}^{n+1}$.

IV. *Experimental Apparatus and Procedures*

The purpose of this chapter is to describe the equipment and procedures used to obtain the physical data necessary to verify the numerical model presented in Chapter II. The initial portion of the chapter discusses those variables that needed to be measured in the physical experiments, followed by a discussion of the actual equipment and procedures used to gather the data for the different physical experiments conducted in this work.

Experimental Goal

Figure 4-1 shows the input variables the code requires and the output it provides to the user. The boxes with the rounded corners refer to software-related items while the sharp-edged boxes refer to experimental quantities. The required input variables are:
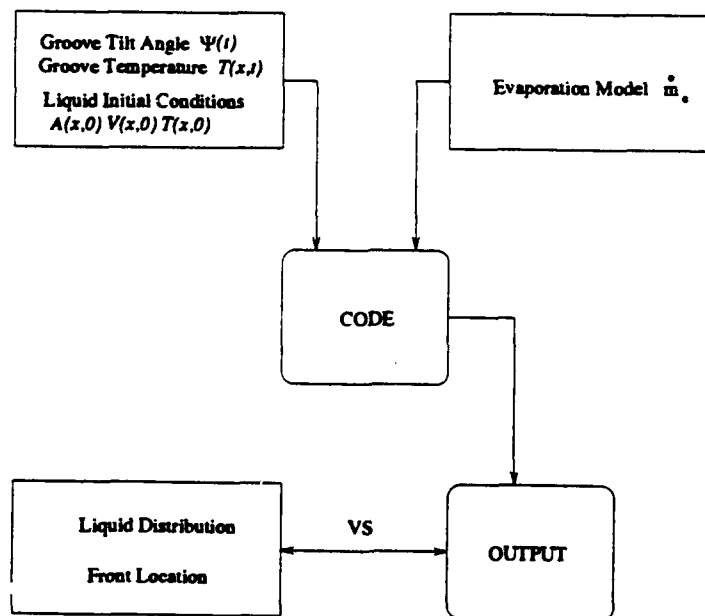

Figure 4-1. Relationship Between Code Input and Output

groove tilt schedule, groove temperature schedule, liquid evaporation model and liquid initial conditions. All of these parameters need to be measured experimentally. Output from the code includes the liquid cross-sectional flow area, liquid velocity and temperature, all as a function of location and time. Since these last two quantities are impossible to measure in the small channels of this study, experimental measurement of the cross-sectional flow area and the location of the fronts provides the data necessary for code validation.

The goal of this portion of the research, therefore, was to design a physical experiment that subjected a heated, axially-grooved capillary structure and the liquid contained within to a transient body force. The transient force was generated by varying the tilt angle of the groove as a function of time. The experimental apparatus needed to measure the groove tilt angle as a function of time, the groove temperature distribution as a function of axial location and time, the cross-sectional flow area of the liquid in the groove as a function of axial location and time and the evaporation ..te of the working fluid as a function of temperature.

Apparatus and Procedures

This section describes the equipment used and the procedures followed for the four physical experiments that were accomplished in this work; namely, the experiment that determined the evaporation rate of ethanol as a function of temperature, the experiment that validated the use of the depth gauge, the experiment that validated the measurement of the front location, and finally, the body force experiments that gathered the cross-sectional flow area and dryout and rewet front location data.

Evaporation Experiment. Figure 4-2 shows the schematic of the evaporation experiment. Ethanol was chosen as the working fluid due primarily to its excellent
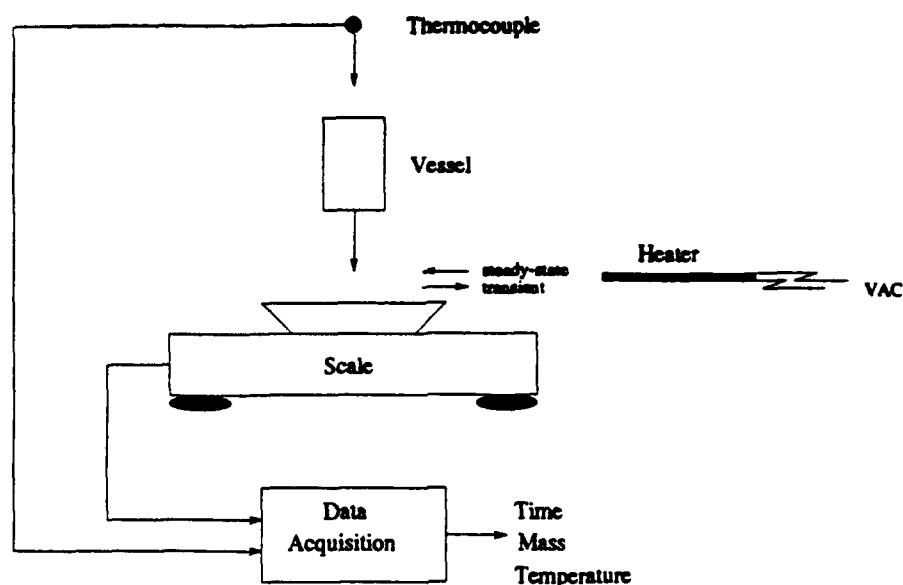
Figure 4-2. Schematic of Evaporation Experiment

wetting characteristics with respect to stainless steel--the material used to construct the groove. A cylindrical vessel with an opening of known cross-sectional area was placed on a digital scale and a thermocouple placed within the vessel. The scale and thermocouple were connected to a digital acquisition system that recorded the mass and temperature of the ethanol in the vessel as a function of time. An optional heater was placed between the vessel and the scale depending on whether a steady-state or transient measurement was desired.

The transient evaporation test was accomplished first. The optional heater was removed from the setup and the vessel with ethanol was independently heated until the ethanol was boiling. The vessel was then placed on the scale and the thermocouple placed into the ethanol. As the ethanol cooled, the total mass and temperature were recorded as a function of time. Figure 4-3 shows an example mass profile from a sample
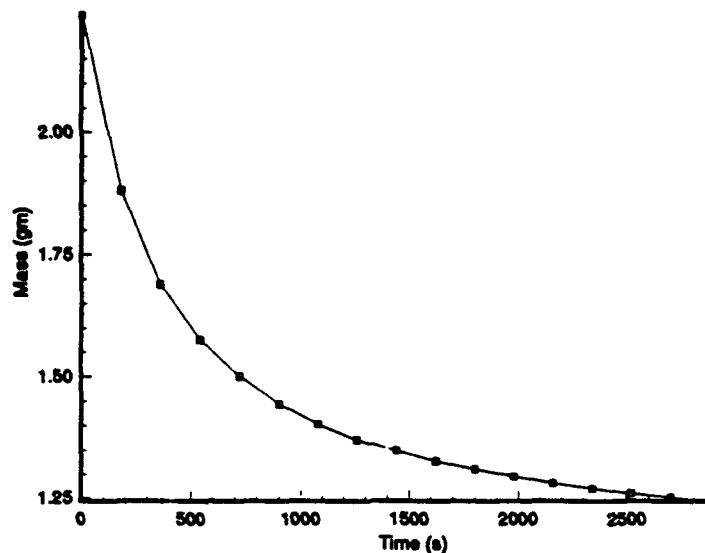
Figure 4-3. Example Mass Profile--Transient Test

transient test. In this figure, each square represents the ethanol in the vessel at a different temperature; the longer the time, the cooler the temperature. By finite differencing this data using

$$\dot{m}_e(T) = \left| \frac{m_{i+1} - m_{i-1}}{t_{i+1} - t_{i-1}} \right| \qquad [4\text{-}1]$$

where the subscript i refers to a specific data point, m is the mass and t is the time, a profile of mass flow versus temperature for ethanol was generated and is seen in Figure 4-4. This was done to establish the general shape of the mass flow curve. The transient test was accomplished twice to ensure repeatability of the results.

To validate the mass flow curve generated by the transient test, several steady-state tests were conducted. These were done similarly to the transient tests; the only difference being that the optional heater was inserted between the vessel and the scale. The vessel
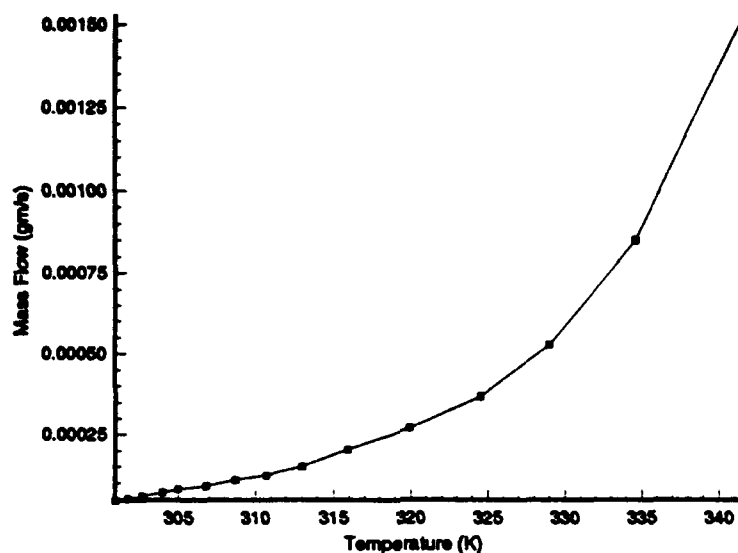
Figure 4-4. Example Mass Flow Profile--Transient Test

with ethanol was placed on the scale with the heater. The ethanol was heated until the temperature reached some steady-state value that depended on the amount of input power. The data acquisition system was activated and a mass profile curve was generated as seen in Figure 4-5. Since the temperature in these tests was held constant, the mass flow rate, determined by the slope of the data, was constant as evident from the figure. Numerous steady-state tests, each representing a different temperature, were accomplished and the mass flow determined by performing a linear best fit to the data.

Plotting these mass flows against temperature yielded the experimental mass flow profile for ethanol seen in Figure 4-6. The vertical lines on this plot refer to the uncertainty associated with each of the measurements. A spline fit through the data points is depicted by the dashed line and it was this fit that was input into the code as the
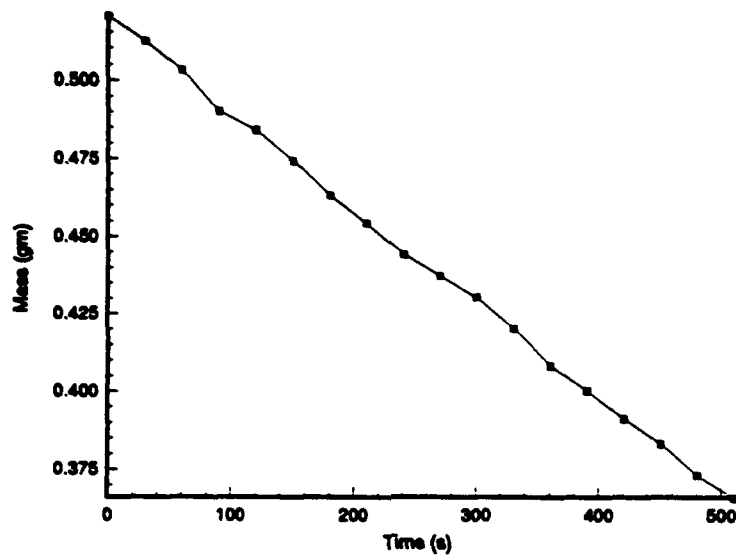
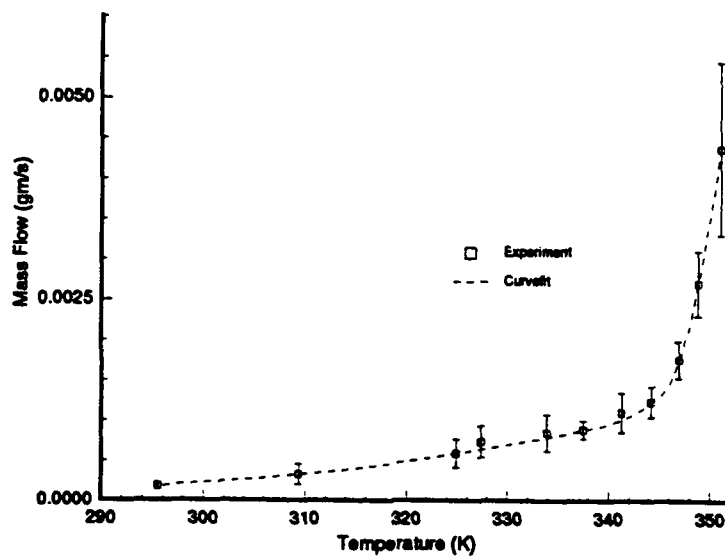**Figure 4-5.** Example Mass Profile--Steady-State Test

Figure 4-6. Experimental Mass Flow Profile

evaporation model. The data points in Figure 4-6 represent the average of two experimental runs. The associated uncertainties were calculated using a least squares analysis.

The last three experiments were conducted with the groove structure and supporting instrumentation. The groove structure consisted of a substructure which was a stainless steel plate into which rectangular grooves were milled, and a superstructure into which the plate was placed. Details of the equipment are now described.

Equipment. Figure 4-7 shows the schematic of the substructure which includes a grooved plate and heater assembly. The plate was constructed from 302 stainless steel and was 152.4 mm x 34.925 mm x 6.35 mm in dimension. Eight rectangular channels were milled into the top of the plate; each channel being 1.5875 mm square. A stainless steel end plate was welded onto each end to prevent liquid outflow; each plate was 34.925 mm x 12.7 mm x 3.175 mm in dimension. A 25.4 mm x 101.6 mm x 0.254 mm flexible strip heater was attached to the bottom of the plate with adhesive. Seven circular holes, each 1.5875 mm deep were drilled into the center peak as seen in the figure; each hole equally spaced axially along the groove and the hole diameter sufficient to house a thermocouple bead. Seven thermocouples were cemented into the holes with a high thermal conductivity thermocouple cement. A metric ruler was attached to the top of the groove substructure and was used to measure the front location.

This substructure was placed into a superstructure assembly seen in Figure 4-8. The superstructure was made of plexiglass and a cavity was milled out sufficiently large to entirely encase the substructure. Silicone cement was placed into the cavity and the substructure inserted and allowed to dry in place. The silicone cement served to thermally insulate the substructure as well as hold it in place within the cavity. The superstructure was supported by two aluminum struts (one on either side) and allowed to

4-7

(34.925 mm x 12.7 mm x 3.175 mm end plates)

152.4 mm x 34.925 mm x 6.35 mm

VAC

(25.4 mm x 101.6 mm x 0.254 mm kapton strip heater)

(holes for thermocouple bead--1.5875 mm deep)

x

5.56 mm

5.56 mm

1.5875 mm typ.
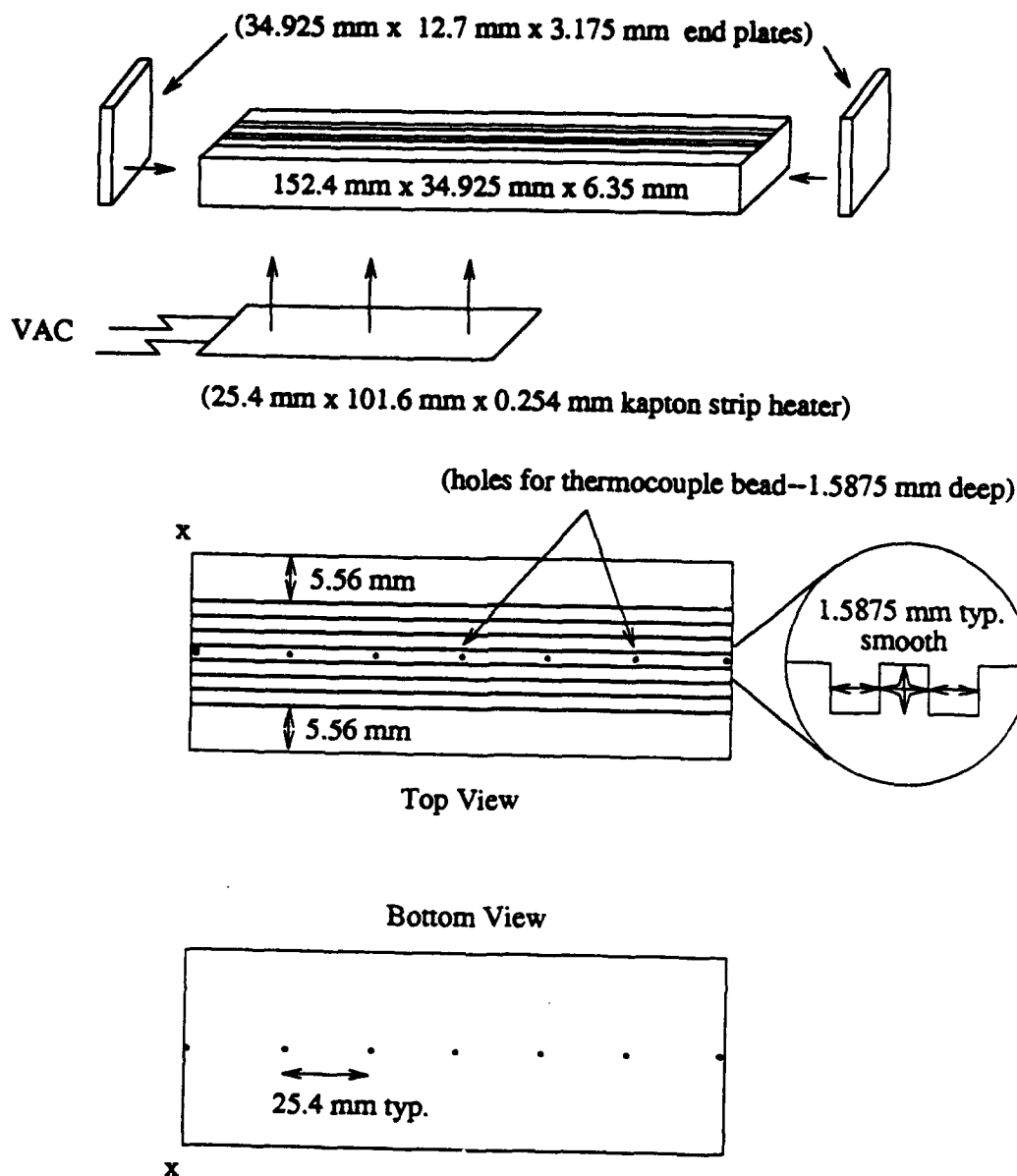smooth

Top View

Bottom View

25.4 mm typ.

x

Figure 4-7. Schematic of Groove Substructure

rotate around two circular stainless steel pins. A linear variable differential transducer (LVDT) was used to monitor and record the tilt of the superstructure.

A depth gauge and associated supporting structure were connected to the superstructure. The depth gauge was simply a micrometer with a needle point attached to the end. The gauge was positioned directly above a center channel such that its motion allowed the needle point to traverse into and out of the groove as seen in the insert in Figure 4-8. The axial location of the gauge was measured from the center of rotation of the groove structure and was fixed for any particular data run but could be varied between runs. An optical magnifier and supporting structure were positioned on the other end of the superstructure. This magnifier was used to monitor the movement of the depth gauge into and out of the groove to ensure that the needle point did not come in contact with the liquid.

Test Procedures. Three experiments were done with the groove assembly (substructure and superstructure with associated instrumentation). The results from these experiments are presented in Chapter V. The first experiment was performed to establish correct procedures for using the depth gauge and also to validate the evaporation model. The second experiment was performed to establish techniques for measuring the front location within the groove structure. Once the measurement of the front and the liquid distribution in the groove were validated their associated uncertainties determined, the final experiment was performed. This experiment attempted to validate the dynamics of the liquid flow in the heated groove subject to a transient body force. The data from this final experiment was used as the basis for validating the numerical model.

Figure 4-9 shows the general schematic of the groove structure and associated data acquisition. Thermocouple one was positioned at the hottest part of the groove and thermocouple seven was positioned at the coolest part. This was also the location
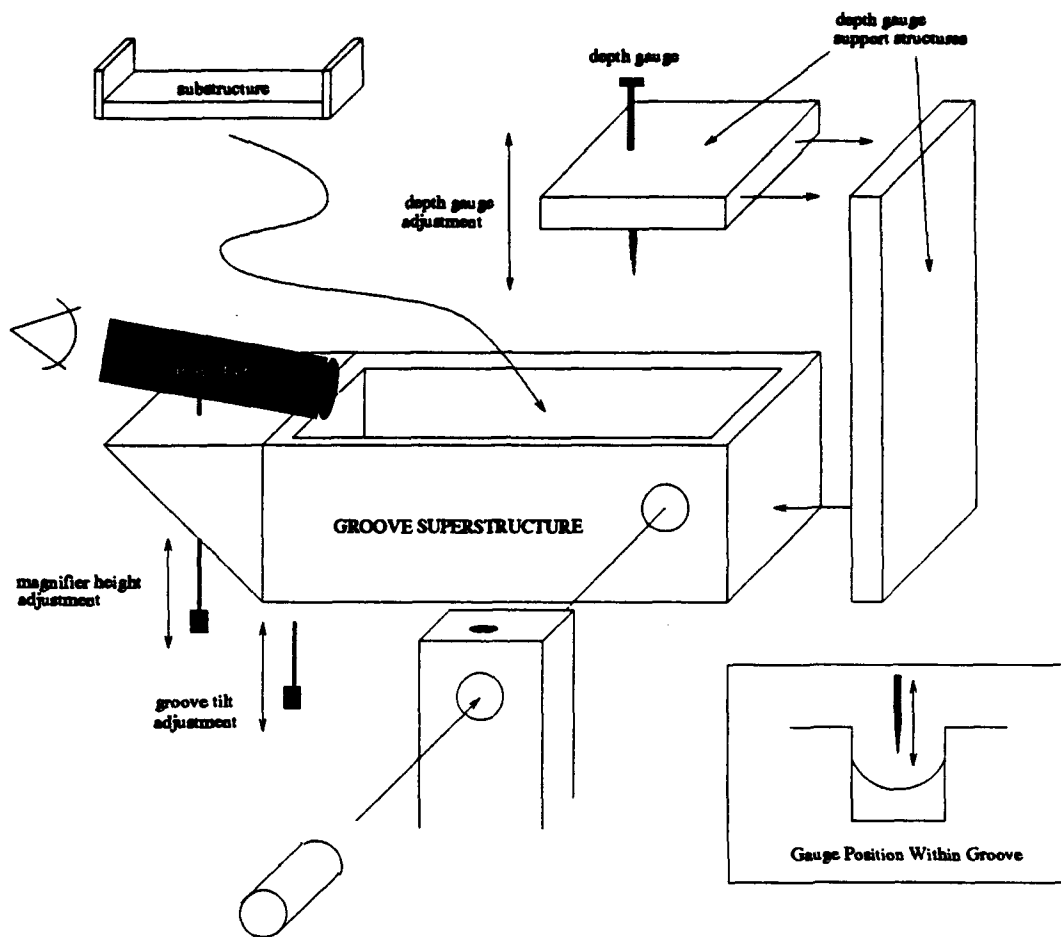
Figure 4-8. Schematic of Groove Superstructure

around which the entire structure rotated. The groove tilt was accomplished manually, monitored with a digital display and recorded with the LVDT via the data acquisition system. The depth gauge was also operated manually but its output was manually noted and recorded. The front location, when it occurred, was also manually noted against the metric ruler and recorded.
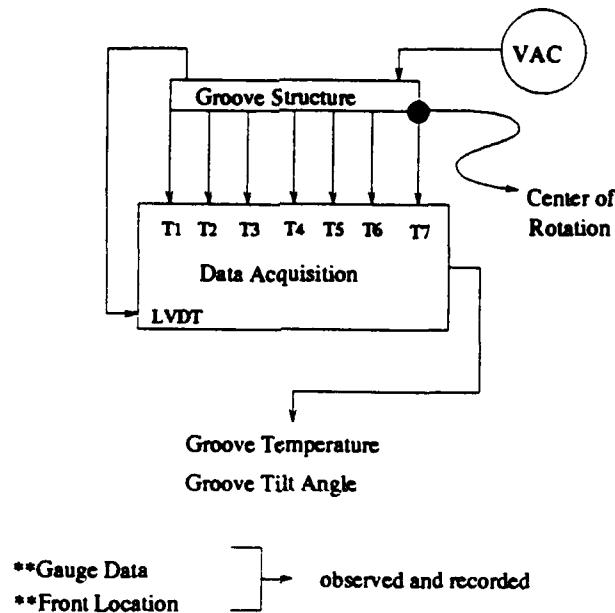
Figure 4-9. General Overview--Test Schematic

Depth Gauge Experiment. This experiment was done to establish the correct procedures for using the depth gauge and also to validate the evaporation model. The groove was leveled (and kept level throughout this test) using an inclinometer which provided accuracy to 0.30 milli-radians. The gauge was positioned 76.2 mm axially from the center of rotation--an axial position of $x^* = 0.50$. The eight grooves were flooded with ethanol and the test was begun.

Total test time for this experiment was 15 minutes. Every sixty seconds the depth gauge was slowly lowered into the groove until the needle point was just above the meniscus as seen in Figure 4-10. This was determined by monitoring the movement of the needle point with the magnifier and observing the reflection of the point in the liquid. When the reflection was noted, the needle motion was stopped and its depth into the groove, h_p , was recorded. The uncertainty in this measurement was $\pm$ 0.08 mm and resulted primarily from the uncertainty in the micrometer adjustment and secondarily from the uncertainty in determining the proximity of the needlepoint to the meniscus.
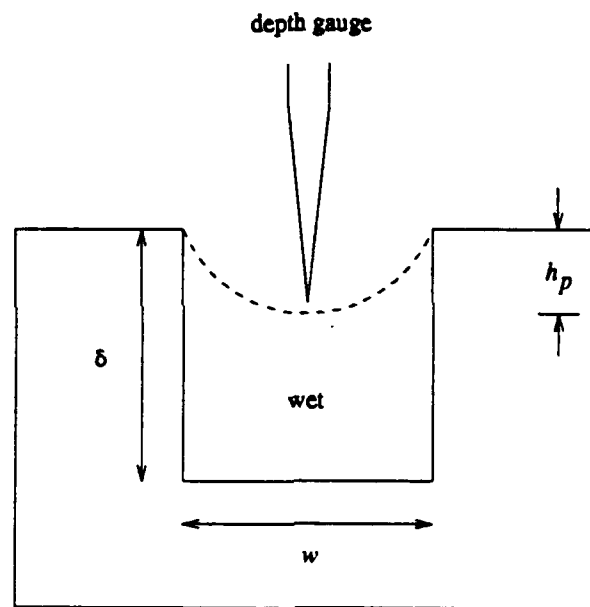

Figure 4-10. Schematic of Depth Gauge Movement

This test was performed with the heater off to evaluate the evaporation model at ambient temperature and then with the heater on to determine if this method could capture the increased recession of the meniscus at elevated temperatures. The groove heating schedule, between zero and six minutes, is seen in Figure 4-11. Between the six and 15

minute points, the heater power was reduced to maintain the groove temperatures at their six minute values. The data for each thermocouple in Figure 4-11 was curvefit in time using a simple polynomial fit. There was no attempt to curvefit the temperature data with respect to axial location; a simple linear fit between each thermocouple was used. The results of these curvefits were input into the code as the required heating schedule. Each test (heater on and heater off) was performed twice to ensure repeatability of the results.
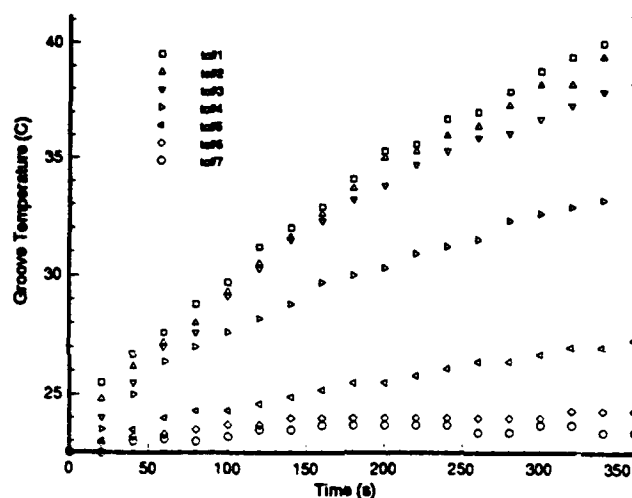

Figure 4-11. Groove Heating Schedule

The experimental data from this test, h_p, is a measure of the liquid cross-sectional flow area. To compare the experimental data to that generated from the code, h_p needs to be derived in terms of what the code outputs (i.e. the cross-sectional flow area and radius of curvature). Using analytic geometry, h_p was shown to be

$$h_p = \delta - R + (R^2 - 0.25w^2)^{0.5} \qquad \text{[4-2]}$$

for a cross-sectional flow area between A_{c1} and A_{c2}. For a cross-sectional flow area between A_{c2} and A_{c3}, h_p was

$$h_p = \delta - \frac{A}{w} + \frac{w}{8}(4 - \pi) \qquad \text{[4-3]}$$

For any cross-sectional flow area less than A_{c3}, dryout of the groove had begun and h_p was simply the groove depth, δ.

Front Location Experiment. The front location experiment was performed to establish methods for measuring the front location in the groove structure during a dryout or rewet.

The experiment was initiated from the level condition and was performed with the heater off. The grooves were filled with ethanol and evaporation was allowed to continue until the depth guage could be inserted halfway into the channel--a depth of 0.79 mm. The groove was then rotated with a constant rate of 0.291 mrad/s to a maximum angle of 0.0524 rad which occurred at 180 seconds. Between 180 and 240 seconds, the groove was maintained at 0.0524 rad. This schedule was chosen after numerous trial tests because it provided visible dryout in the groove structure without causing a flood condition.

As the front formed in the groove during this transient, its position was noted and recorded. Accuracy of the front measurement was ± 5 mm. This experiment was performed twice to ensure repeatability of the results.

Recall from Chapter I that the definition of a front is the interface between the dry and wet areas in the wick. For this work, a front was defined to exist when the level of liquid in the groove was sufficient so that the tangent to the meniscus was coincident with the bottom of the groove as shown in Figure 4-12. Using this definition, when a front

Head-On View   Top View
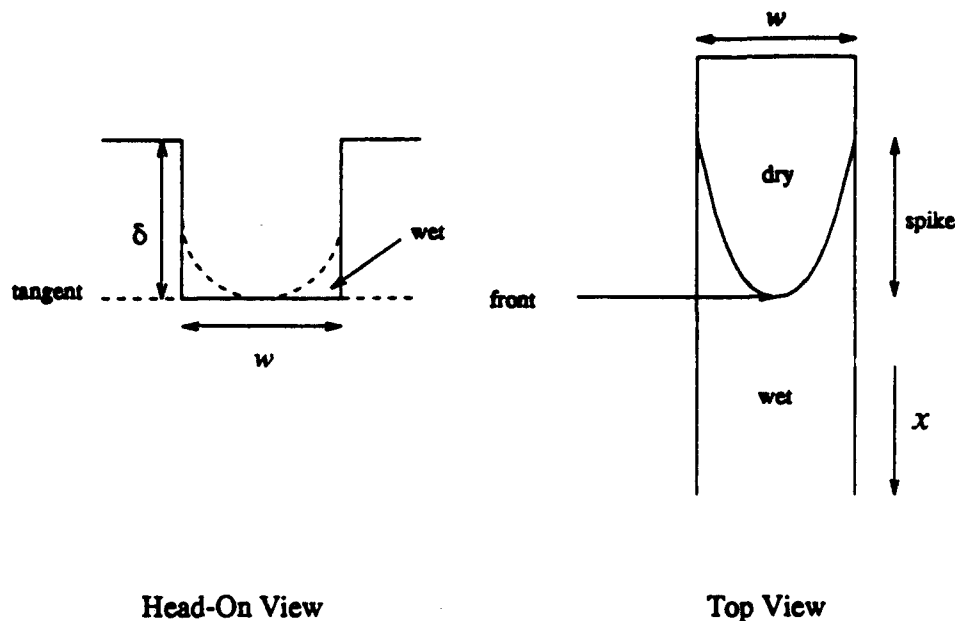
Figure 4-12. Liquid Front Definition

forms, there is still some liquid in the groove; the non-dimensional cross-sectional flow area corresponds to $A^* = 0.1073$. This definition of the front was chosen because it was the most readily visible during the preliminary testing. The presence of the spikes discussed in Chapter II were visible but the ability to accurately determine their length and where they ended was questionable.

Body Force Experiments. The body force experiments consisted of the equipment and procedures used to gather the data on the liquid distribution and the location of the dryout and rewet fronts in the heated groove subject to a transient body force. Power-off tests were conducted to model the liquid dynamics independent of any heat transfer. Once it was determined that the dynamics were properly modeled, the power-on testing was accomplished. Data from these tests were used to validate the numerical model of Chapter II.

4-15

Power-Off Test. This series of tests was used to gather data on the motion of the liquid in the groove independent of any external heat transfer. This test served two purposes; first, it tested the ability of the numerics to model the physics of the liquid dynamics independent of any external heating. If this basic problem could not be modeled, then there was no reason to pursue the external heating case. Its second purpose was to provide the baseline data against which to match the external heating data.

The power-off tests were started in a manner similar to the depth gauge and front location tests. The only difference was that these tests involved an angular rotation of the groove assembly. The groove structure was rotated through the angular schedule seen in Figure 4-13. Interval 1 consisted of a constant rate of +0.01745 radians per minute for
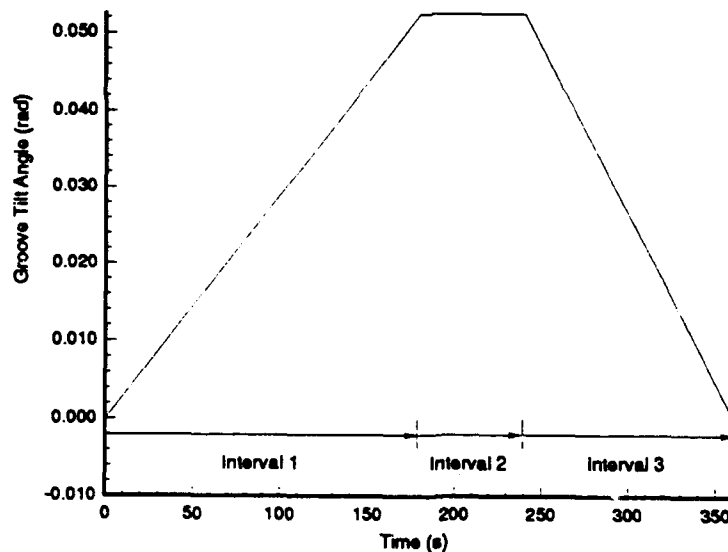

Figure 4-13. Groove Angular Schedule

the first three minutes. Between minute three and minute four (Interval 2), the angle was held constant at 0.05236 radians. Between minutes four and six (Interval 3), the angular

4-16

rate was -0.02618 radians per minute so that the groove was back to level at the six minute point. This schedule was chosen to provide a test of two different frequencies of application of a body force.

If the body force per unit mass, $F_B = g\sin\psi + \Omega^2 r$, is assumed to behave in a sawtooth manner, then the frequency of the body force in Interval 1 is 2.8 mHz and the frequency of the body force in Interval 3 is 4.2 mHz. Interval 1 then results in a maximum body force per unit mass of 0.51 m/s^2 at a frequency of 2.8 mHz, while Interval 3 results in the same maximum body force but at a higher frequency of 4.2 mHz as seen in Figure 4-14.
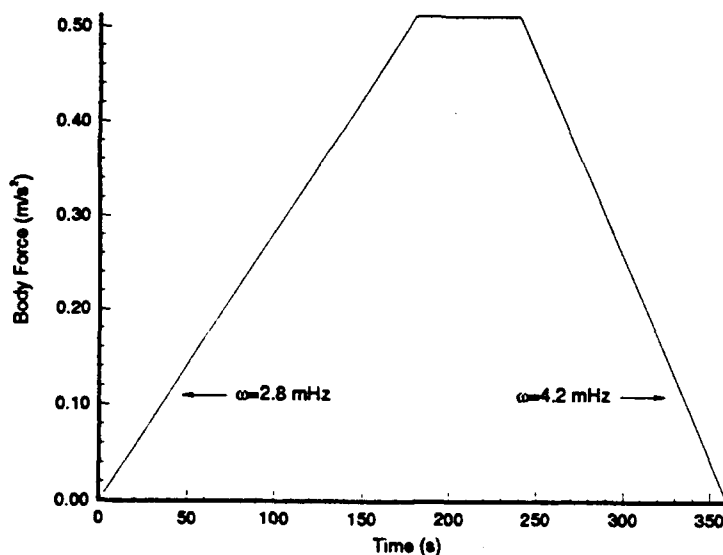

Figure 4-14. Transient Body Force Schedule

The reason that the maximum angle, and therefore the maximum body force, was so low was because of the no flooding restriction discussed earlier. Since the grooves could not be flooded, the maximum angle that the groove could be raised to was

approximately 0.05 radians. This resulted in the heated end of the groove being raised to a maximum height of approximately 8 mm.

The test began by leveling the groove and filling the individual channels with ethanol. The ethanol was allowed to evaporate, with the groove level, until the depth gauge measurement was approximately 0.8 mm. This corresponded to the groove being half full and resulted in a non-dimensional cross-sectional flow area of $A^* = 0.6073$. At this point, the rotation schedule described above was started and the data acquisition system was initiated. Depth gauge measurements for this test were taken at $x^* = 0.125$ and at approximately one minute intervals. When a front appeared, its location and time were also recorded.

Power-On Test. The power-on tests were done in exactly the same manner as the power-off tests with the exception of the heating of the groove substructure. The same procedure used to establish the initial conditions in the power-off tests was used for this test. The difference was that when the level of ethanol in the groove substructure reached the 0.8 mm level used in the power-off testing, the heater was turned on and remained on for the duration of the test. Readings from the seven installed thermocouples were recorded, along with the groove tilt as a function of time. The same variables that were measured in the power-off tests were measured in this series of tests; namely, depth gauge measurements at the $x^* = 0.125$ location and dryout and rewet front positions when they occurred.

V. *Results and Discussion*

This chapter presents the results of numerical experiments performed with the code and the results of the physical experiments described in Chapter IV. The first portion of this chapter describes the numerical experiments and presents the results that established confidence in the code's ability to model the liquid flow, to include dryout and rewet, in a heated capillary structure subject to transient body forces. The second portion of the chapter deals with the physical experiments; specifically, results from the depth gauge, front location and body force experiments are presented and comparisons are made with the numerics. Trends between the numerics and the physical data are noted and explained. This is followed by a numerical sensitivity study that is divided into three sections. The first section determines the sensitivity of the results to those variables that were experimentally measured and used as input to the code. The second section of the study determines the sensitivity of the solution to several terms in the governing equations and the third section determines the sensitivity of the solution to the numerical grid. The third portion of this chapter discusses the improvement of the new model over the Beam piston model and provides a comparative study.

Numerical Experiments

Several numerical experiments were performed with the code to establish confidence in its ability to model the flow of liquid in a heated capillary structure subject to transient body forces. Since no comparisons to physical data were made, absolute accuracy of the results was not considered important. However, correct trends needed to be demonstrated as well as the ability to numerically model the formation of a front in the groove structure. The complexity of each experiment was increased until all the

relevant phenomena expected in the physical experiments were included and modeled. Each numerical experiment is now described.

Test One--No Body Force. The purpose of this test was to demonstrate that liquid in a groove that is initially level and remains level should have no tendency to move. The test setup is shown in Figure 5-1. The groove, shown by the dotted line in the figure, is a square channel. The width, w, and depth, δ, are 1.5875 mm, where the width dimension is into the page. The groove length, L_{∞}, is 0.254 m, the liquid is ethanol and the capillary force and evaporation are neglected. In this test, the groove is maintained at the ambient temperature, $T = 295K$, and is not allowed to rotate. The initial area distribution is such that the groove is exactly one-half full. This is represented by the shaded area in the figure.

Figure 5-2 shows the results of a ten second real time computer run. This is a three-dimensional plot of the non-dimensional area distribution in the groove, A^*, as a function of non-dimensional time, t^*, and non-dimensional axial groove location, x^*. Each axis runs from a minimum value of zero to a maximum value of one. The perspective of the liquid distribution is from an observer positioned on the groove. According to the figure, the area distribution does not vary with time from its initial level value of 0.5 (one-half full); the steady-state condition.

Test Two--Steady Body Force. This test was accomplished similarly to the first test; the only difference being in the initial groove angle and liquid distribution. The groove is set at an initial angle of, $\psi_{init} = \tan^{-1}(\delta/L_{\infty})$, and the initial distribution of liquid is such that $A^* = 1$ at the left end of the groove ($x^* = 0$) and $A^* = 0$ at the right end ($x^* = 1$) with a linear distribution in between, as shown in Figure 5-3. This provides the same volume of liquid used in the first test. In the absence of any capillary or body

L_∞

$T=295K$ $T=295K$

$\psi = \psi_{max} \sin(2\pi\omega t)$ $0 \le t \le \theta$
$\psi = 0\ rad$ $t > 0$

$10\ s$

Run Parameters

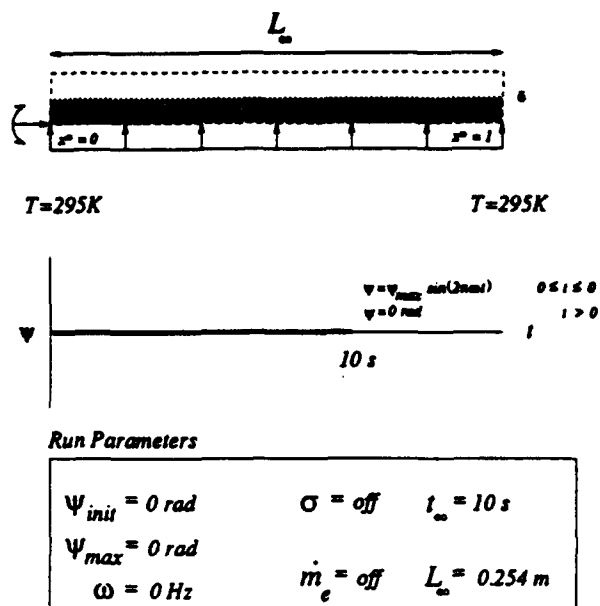|		
$\psi_{init} = 0\ rad$	$\sigma = off$	$t_\infty = 10\ s$
$\psi_{max} = 0\ rad$		
$\omega = 0\ Hz$	$\dot{m}_e = off$	$L_\infty = 0.254\ m$

Figure 5-1. Numerical Test One Parameters
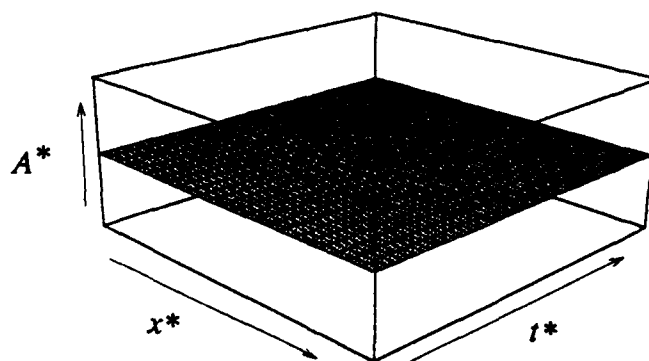

A^*

x^* t^*

Figure 5-2. Numerical Test One Results

forces, there should be no tendency for the liquid to change from this position, which is the steady-state solution for the initial conditions.

Figure 5-4 shows the results of a ten second real time computer run and reveals no change from the initial distribution described above. This result demonstrates that the hydrostatic and atmospheric pressure forces, along with the body force, are modeled properly and coded correctly.

Test Three--Steady Body Force With Motion. It was necessary to determine if the code could predict the correct steady-state solution for an initial condition other than steady-state. To demonstrate this behavior, a setup identical to test two was used with the initial liquid distribution similar to that of test one and is shown in Figure 5-5. From this initial condition, the liquid should begin to flow towards the left end of the groove $(x^* = 0)$ and reach the steady-state conditions of test two.

Figure 5-6 shows the results of a ten second real time computer run. Note that as time progresses, A^* increases at $x^* = 0$ and decreases at $x^* = 1$. This shows bulk liquid motion towards $x^* = 0$, and at $t^* = 1$, steady-state conditions are achieved. This test demonstrates that the code predicts the correct steady-state solution for a non steady-state initial condition.

Test Four--Steady Body and Capillary Forces. This test was performed to determine if the capillary force was coded properly. The initial conditions for this experiment are seen in Figure 5-7. The groove tilt angle was similar to test three and the liquid distribution was the same as test two. In the absence of the capillary force, it was seen in test two that the liquid had no tendency to move. However, if the capillary force is now considered, the liquid should have a tendency to move towards $x^* = 1$ since the liquid in that end has receded further into the groove and the capillary influence should be greatest.

Run Parameters

$\psi_{init} = 0.00625\ rad$	$\sigma = off$	$t_{\infty} = 10\ s$
$\psi_{max} = 0\ rad$		
$\omega = 0\ Hz$	$\dot{m}_e = off$	$L_{\infty} = 0.254\ m$
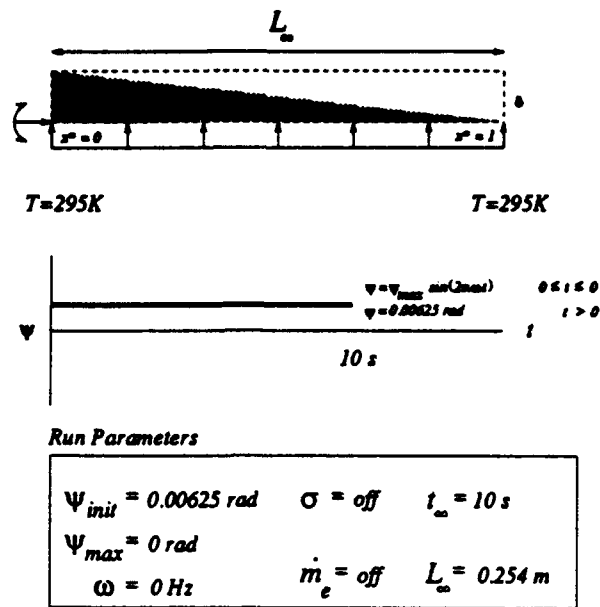
Figure 5-3. Numerical Test Two Parameters
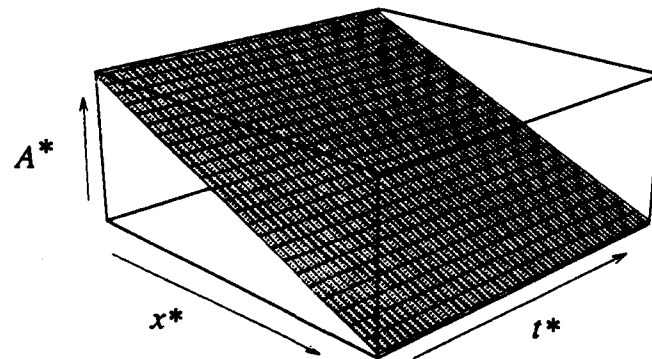
Figure 5-4. Numerical Test Two Results

Run Parameters

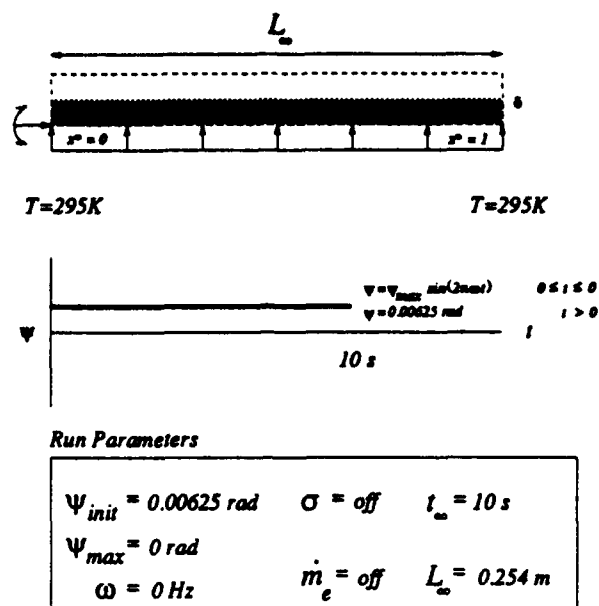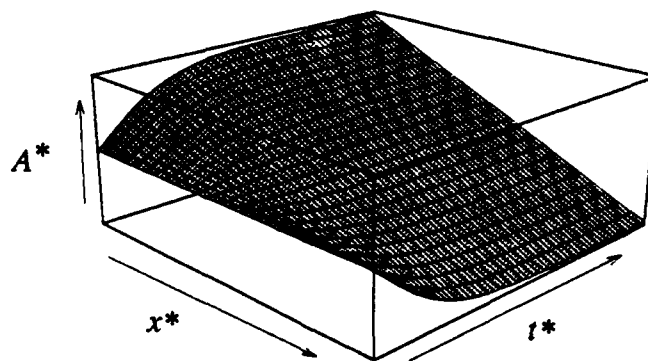|		
$\psi_{init} = 0.00625\ rad$	$\sigma = off$	$t_{\infty} = 10\ s$
$\psi_{max} = 0\ rad$		
$\omega = 0\ Hz$	$\dot{m}_e = off$	$L_{\infty} = 0.254\ m$

Figure 5-5. Numerical Test Three Parameters

Figure 5-6. Numerical Test Three Results

Figure 5-8 shows the results from this study. With the capillary force present, the liquid does indeed move towards $x^* = 1$ as seen by the increase in A^* at $x^* = 1$ and a corresponding decrease in A^* at $x^* = 0$. The liquid approaches a steady-state distribution different from the steady-state condition seen in Figure 5-4. This is due to the inclusion of the capillary force.

The remaining three numerical experiments were performed with the capillary force and evaporation present. The goal of these remaining experiments was to determine the code's ability to model the liquid motion in the groove under transient body forces and external heating; two important parameters that were neglected in tests one through four. The magnitude and duration of the body forces and heating were sufficient to form a liquid front in the groove; a phenomenon also neglected in tests one through four.

Test Five--Transient Body Force, No External Heating. This test was performed to determine if the code could capture the formation of a liquid front in a groove that was subject to a transient body force but no external heating. No external heating refers to no externally applied heat sources, such as a heater. It does not mean that no heat transfer takes place; in fact, heat transfer does occur in the form of evaporation.

In this test, the groove was initially at a level condition and one-third full of liquid. The groove was rotated through the schedule shown by the bold line in Figure 5-9. This schedule was

$$\psi = \psi_{max} \sin(2\pi\omega t) \qquad 0 \le t \le 5$$

$$\psi = 0 \qquad t > 5$$

with a maximum angle, ψ_{max}, of 0.0524 radians and a frequency of $\omega = 0.1$ Hz. This particular schedule was chosen after numerous numerical test runs because it resulted in a partial dryout of the groove followed by a rewet.

L_∞

$x^* = 0$ $x^* = 1$

$T=295K$ $T=295K$

$\psi = \psi_{max} \sin(2\pi\omega t)$ $0 \le t \le 0$
$\psi = 0.00625 \, rad$ $t > 0$

t

$10 \, s$

Run Parameters

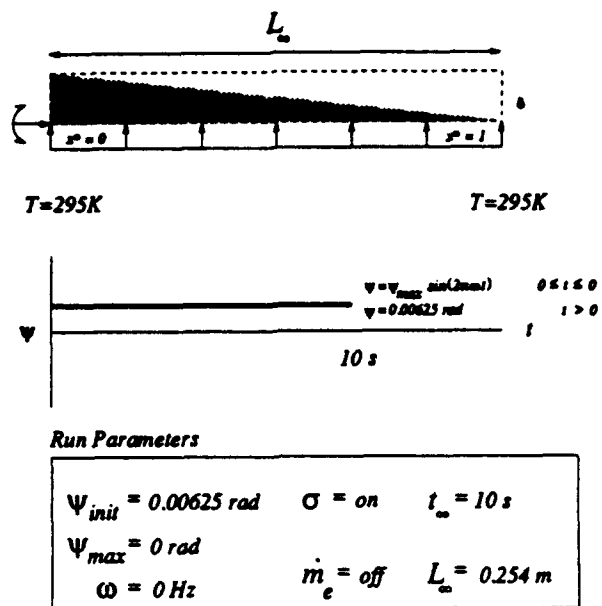|		
$\psi_{init} = 0.00625 \, rad$	$\sigma = on$	$t_\infty = 10 \, s$
$\psi_{max} = 0 \, rad$		
$\omega = 0 \, Hz$	$\dot{m}_e = off$	$L_\infty = 0.254 \, m$

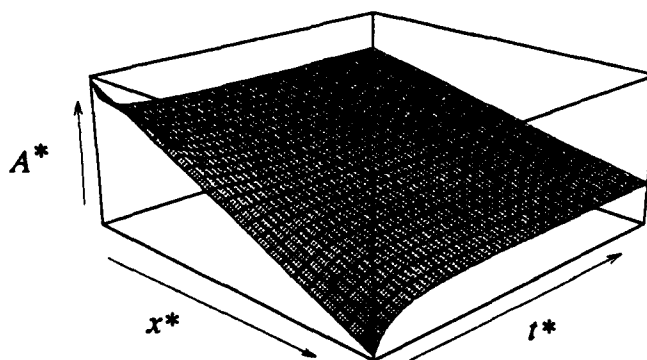**Figure 5-7.** Numerical Test Four Parameters

A^*

x^* t^*

Figure 5-8. Numerical Test Four Results

The results of this test run are shown in Figure 5-10. As the transient body force is applied, the level of liquid at $x^* = 0$ increases and the level at $x^* = 1$ decreases, indicating bulk liquid motion towards $x^* = 0$. At approximately $t^* = 0.3$, the groove dries out; noted by $A^* = 0$ at $x^* = 1$. As the tilt schedule reverses direction back towards the initial level condition, the liquid motion follows and the rewet is captured by the increase in A^* from its zero value. At $t^* = 1$, the liquid distribution in the groove is not level as steady-state conditions would dictate. The code was allowed to run for additional time and the liquid distribution did eventually reach a quasi-steady-state condition. This quasi-steady-state refers to the liquid level in the groove being uniform along its length but decreasing in time due to evaporation of the liquid. The time shown in Figure 5-10 was chosen to reveal details of the dryout and rewet. This experiment validated the code's ability to capture a dryout and rewet due solely to a transient body force.

Test Six--No Body Force, External Heating. This test was performed to determine if the code could capture the formation of a liquid front in a groove subjected to external heating but no transient body force.

In this test, the groove was initially at a level condition and entirely full of liquid. The groove was kept level throughout the test as shown in Figure 5-11. The left end of the groove was maintained at $T = 295K$, the right end was maintained at $T = 345K$, with a linear distribution of temperature between $x^* = 0$ and $x^* = 1$. The maximum temperature of 345 K was chosen to exercise the full temperature range of the evaporation model of Chapter IV.

This test was carried out for 480 seconds. For the first 420 seconds, the temperature profile described above was used. This was done to generate a front.

L_∞

$T=295K$ $T=295K$

$\Psi = \Psi_{max} \sin(2\pi\omega t)$ $0 \le t \le 5$
$\Psi = 0$ $t > 5$

Run Parameters

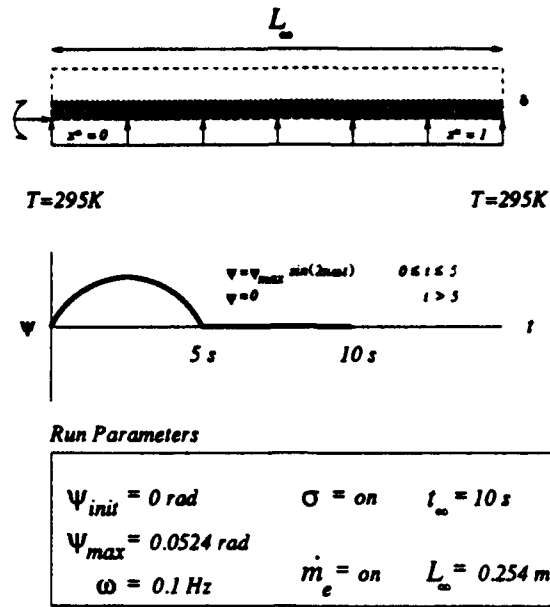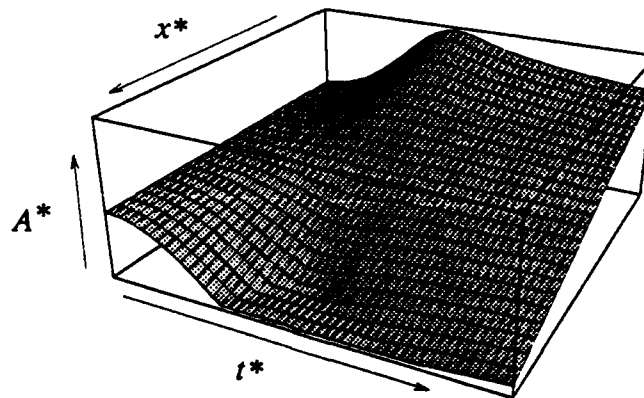|		
$\Psi_{init} = 0\ rad$	$\sigma = on$	$t_\infty = 10\ s$
$\Psi_{max} = 0.0524\ rad$		
$\omega = 0.1\ Hz$	$\dot{m}_e = on$	$L_\infty = 0.254\ m$

Figure 5-9. Numerical Test Five Parameters

Figure 5-10. Numerical Test Five Results

Between 420 and 480 seconds, the temperature profile was reduced to a uniform temperature of $T = 295K$ to allow a rewet to occur.

The results of this experiment are seen in Figure 5-12. Several interesting trends are seen in this figure. First, the decrease in liquid volume between $t^* = 0$ and $t^* = 1$ is evident by the decrease in A^* along the groove. Note however, that the rate of decrease in A^* is greater at $x^* = 1$ than at $x^* = 0$. This is due to the elevated temperatures as x^* approaches one. Higher temperatures result in higher evaporation rates and a quicker depletion of liquid from the groove.

The second trend is the formation of a dryout front, $A^* = 0$, at approximately $t^* = 0.9$. At this point, the elevated temperature profile was reduced to the uniform profile and a rewet of the groove was noted. At $t^* = 1$ the liquid has not reached its quasi-steady-state condition. This test validated the code's ability to capture a dryout and rewet due solely to external heating.

Test Seven--Transient Body Force, External Heating. This numerical experiment was performed to determine the code's ability to capture a dryout and rewet in a groove subject to both transient ody forces and external heating; similar to what was investigated in the physical experiments.

The test setup is shown in Figure 5-13. The heating schedule of test six was combined with the tilt schedule of test five. The total run time for this experiment was ten seconds. This was done to compare the results to those of test five.

The results are seen in Figure 5-14. The same trends noted in Figure 5-10 are seen here; namely, the dryout of the groove at approximately $t^* = 0.3$ and the rewet following the groove rotation back to level. The primary difference between these two figures is in the rewet phase. In Figure 5-10 the rewet is seen by the rise in A^* at
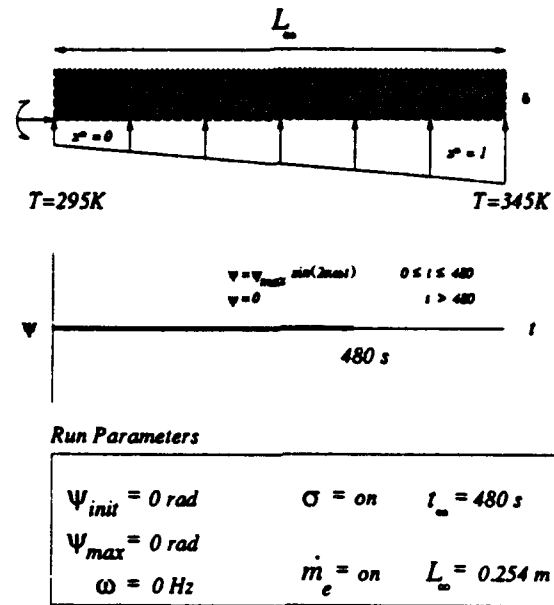
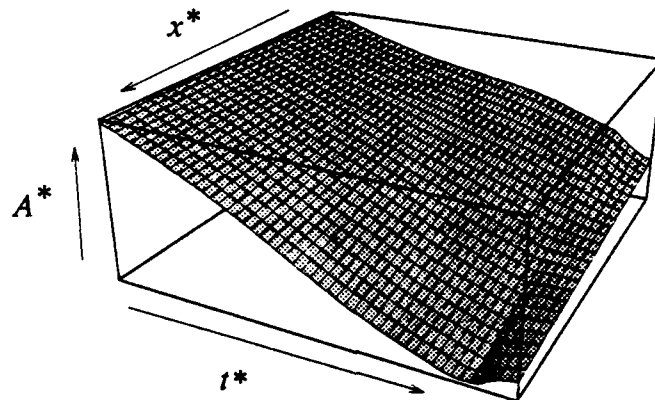Figure 5-11. Numerical Test Six Parameters

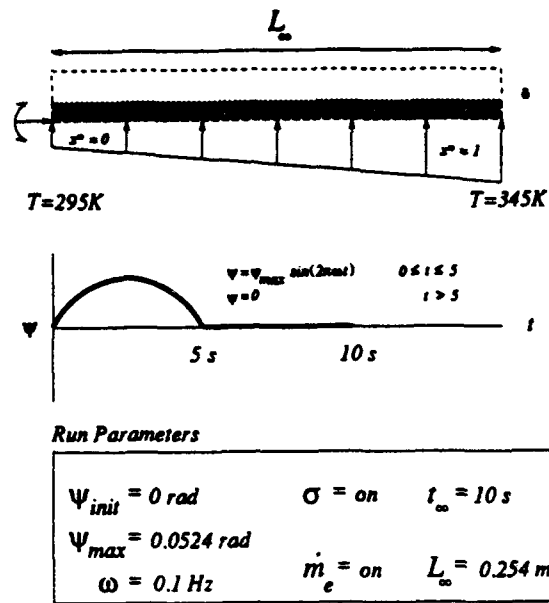Figure 5-12. Numerical Test Six Results
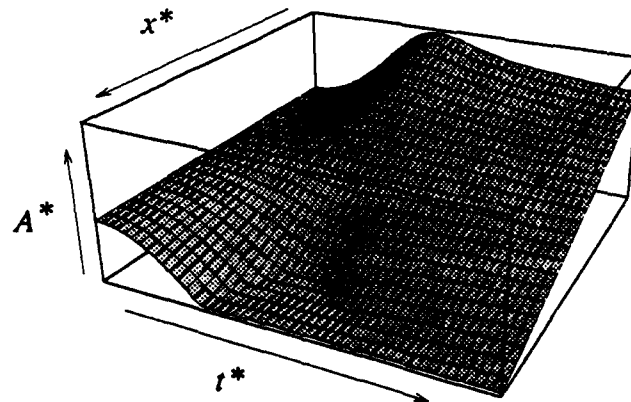
Figure 5-13. Numerical Test Seven Parameters

Figure 5-14. Numerical Test Seven Results

$x^* = 1$ between $t^* = 0.5$ and $t^* = 1$. The same region in Figure 5-14, however, shows a dryout condition; in fact, at $x^* = 1$, A^* is zero at $t^* = 1$, compared to $A^* = 0.045$ in Figure 5-10. This is due to the elevated temperatures and correspondingly increased evaporation rates.

Test Eight--Increased Frequency. An additional numerical study was performed to demonstrate the ability of the code to model the liquid flow in a heated capillary structure under a frequency and amplitude greater than those of tests one through seven.

The code was run at the same conditions as numerical experiments one through seven, but the amplitude was allowed to vary between +0.0524 and -0.0524 radians. Additionally, a frequency of 1 Hz was used; one order of magnitude greater than the maximum frequency of the first seven numerical tests but still below the maximum limit described in Chapter II. Initial liquid distribution and temperature boundary conditions are shown in Figure 5-15.

The results of a sixty second run are shown in Figure 5-16. The sinusoidal motion of the liquid is evident. The overall volume of liquid in the groove is decreasing with time as evidenced by the maximum amplitude of the area peaks at $x^* = 0$ and $x^* = 1$ decreasing with time. No dryout is seen in the figure but this is only because the computer run was stopped before dryout occurred. An additional run was completed to verify that dryout did occur. This was expected since evaporation and bulk liquid motion similar to the previous numerical tests were occurring and dryout occurred in those tests. The code appears to predict the correct trends in the liquid motion.

Based on these numerical tests, confidence was established with the code's ability to model a dryout and rewet in a capillary groove subject to transient body forces and external heat transfer. This however, did not validate the code since no comparisons with
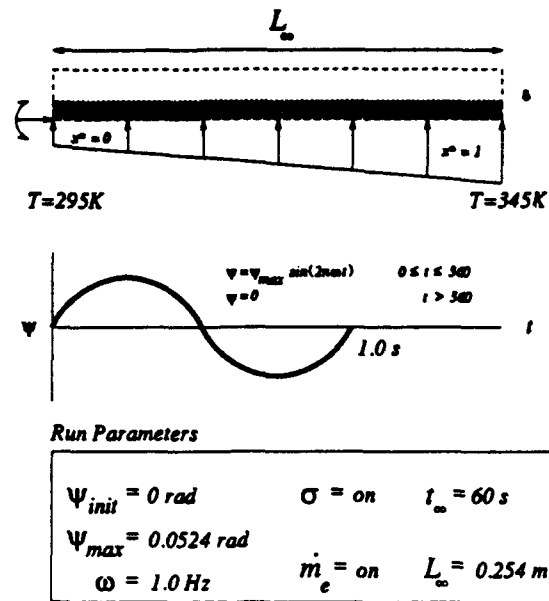
Figure 5-15. Numerical Test Eight Parameters
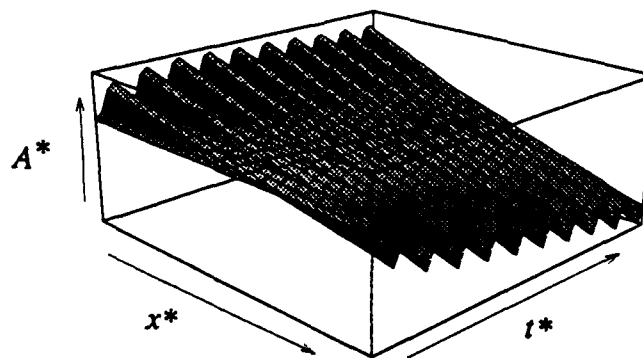
Figure 5-16. Numerical Test Eight Results

physical data were made. A discussion of these physical experiments and the comparison of their results with the numerics is now presented.

Physical Experiments

The physical experiments consisted of the depth gauge tests, the front location tests and the body force tests. The first two of these tests were performed to verify the measurement of and establish the accuracy of the liquid height and front location. The results of each experiment are now presented.

Depth Gauge Experiment. Figure 5-17 shows the results of the depth gauge tests described in Chapter IV. The horizontal axis is non-dimensional time, $t* = (t/t_{\omega})$, where

Figure 5-17. Depth Gauge Test Results

t_{ω} is the total run time; in this case 15 minutes. The vertical axis is non-dimensional liquid height in the groove. This liquid height, h_l , is defined as

$$h_l = (1 - \frac{h_p}{\delta})$$ [5-1]

Four sets of data are on this figure. The solid line represents the numerical solution for the case of no external heating and the dashed line represents the numerical solution for the case with external he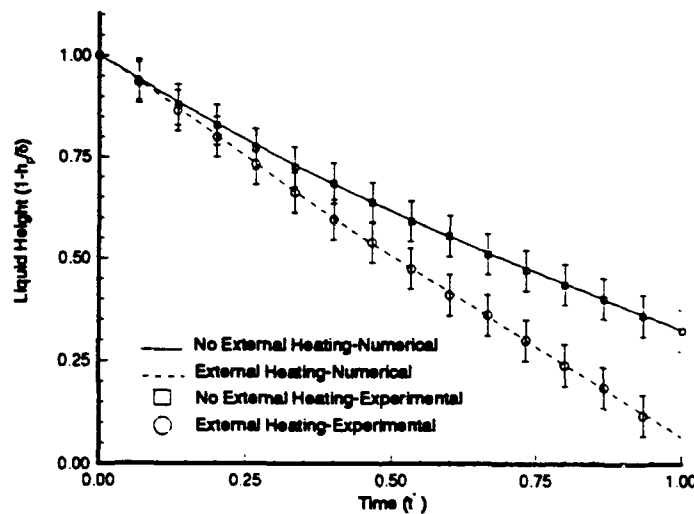ating. Experimental data for each case is shown by the squares and circles. The squares represent the average of two separate experimental runs for the no external heating case. The circles represent the average of two separate experimental runs for the external heating case. The vertical lines on the figure depict the uncertainty in the depth gauge measurement (± 0.08 mm).

The agreement between the numerical solution and experiment is within the uncertainty of the measurements. The rate of evaporation for the groove with external heating is faster than for the groove with no external heating as evidenced by the slope of the dashed line being steeper than the slope of the solid line. At t^* of approximately 0.4 (six minutes into the test) the slope of each line changes and becomes less negative. This is due to the change in input power to the heater discussed in Chapter IV. Both the numerics and depth gauge measurements capture the trend. Based on these observations, the depth gauge was validated as a means of measuring the cross-sectional flow area in the groove and its associated uncertainty was established.

Front Location Experiment. Figure 5-18 shows the numerical and experimental results of the front location tests. The horizontal axis in this figure is non-dimensional time and the vertical axis is non-dimensional front location measured from the center of rotation. The experimental front location data is depicted by the squares and is an average of two experimental runs. The uncertainty is shown by the vertical lines and represents the uncertainty in the front measurement (± 5 mm). Total run time for this test was 17 minutes.

5-17

As seen in the figure, the experimental data matches the theory within the uncertainty of the measurement. Numerical dryout does not occur until approximately $t^* = 0.65$. Once dryout does occur, the front moves towards $x^* = 0$ with a velocity of approximately 0.05 mm/s. Visual observations of the front verified the existence of the spikes discussed in Chapter II. Based on these observations, measurement of the front location and its associated uncertainty was established.
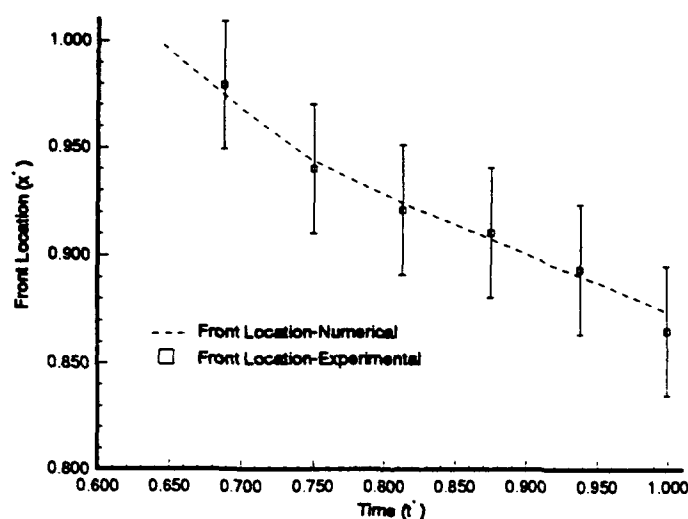

Figure 5-18. Front Location Test Results

Body Force Experiment. The body force experiments were divided into those modeling dryout in the capillary groove due to body force effects with no external heating (power-off) and those modeling dryout in the groove due to body force effects with external heating (power-on). The results of each test are now presented.

5-18

Power-Off Test. Figure 5-19 shows the results from the power-off test described in Chapter IV. Four sets of data are shown in this figure; two corresponding to the numerical results and two corresponding to the experimental results.

The horizontal axis is non-dimensional time, where t_∞ for this experiment is six minutes. The left vertical axis is non-dimensional liquid height, h_l . The right vertical axis is non-dimensional front location. Depth gauge measurements for this test were taken at $x^* = 0.125$.

The solid line on Figure 5-19 represents the liquid height in the groove at $x^* = 0.125$ predicted by the numerics over the span of the experiment. At the beginning of the experiment, h_l is 0.5 as seen in the figure. As the groove is rotated up, (Interval 1), liquid flows towards the gauge position and the distance that the gauge can be lowered into the groove before touching the meniscus is reduced. This corresponds to a rise in the liquid height as seen in the figure.

During the time that the groove is held constant at 0.0524 radians, (Interval 2), the liquid height decreases. During this interval, liquid momentum and gravity were still carrying the liquid towards the gauge position, $x^* = 0$. Because of the momentum and gravity, the liquid height was expected to increase. The decrease is due to the fact that the liquid is continuing to evaporate, which more than offsets the momentum and gravity-induced motion.

During Interval 3, where the groove is lowered back to the level condition, the liquid height decreases more rapidly than the rate of increase observed during Interval 1. This is due to the fact that the frequency with which the body force is applied during Interval 3 is 50 percent higher than the frequency applied during Interval 1.

At $t^* = 1$, the liquid height is approximately $h_l = 0.34$. Because the liquid is still moving towards $x^* = 1$ at this time, this height is higher than the quasi-steady-state
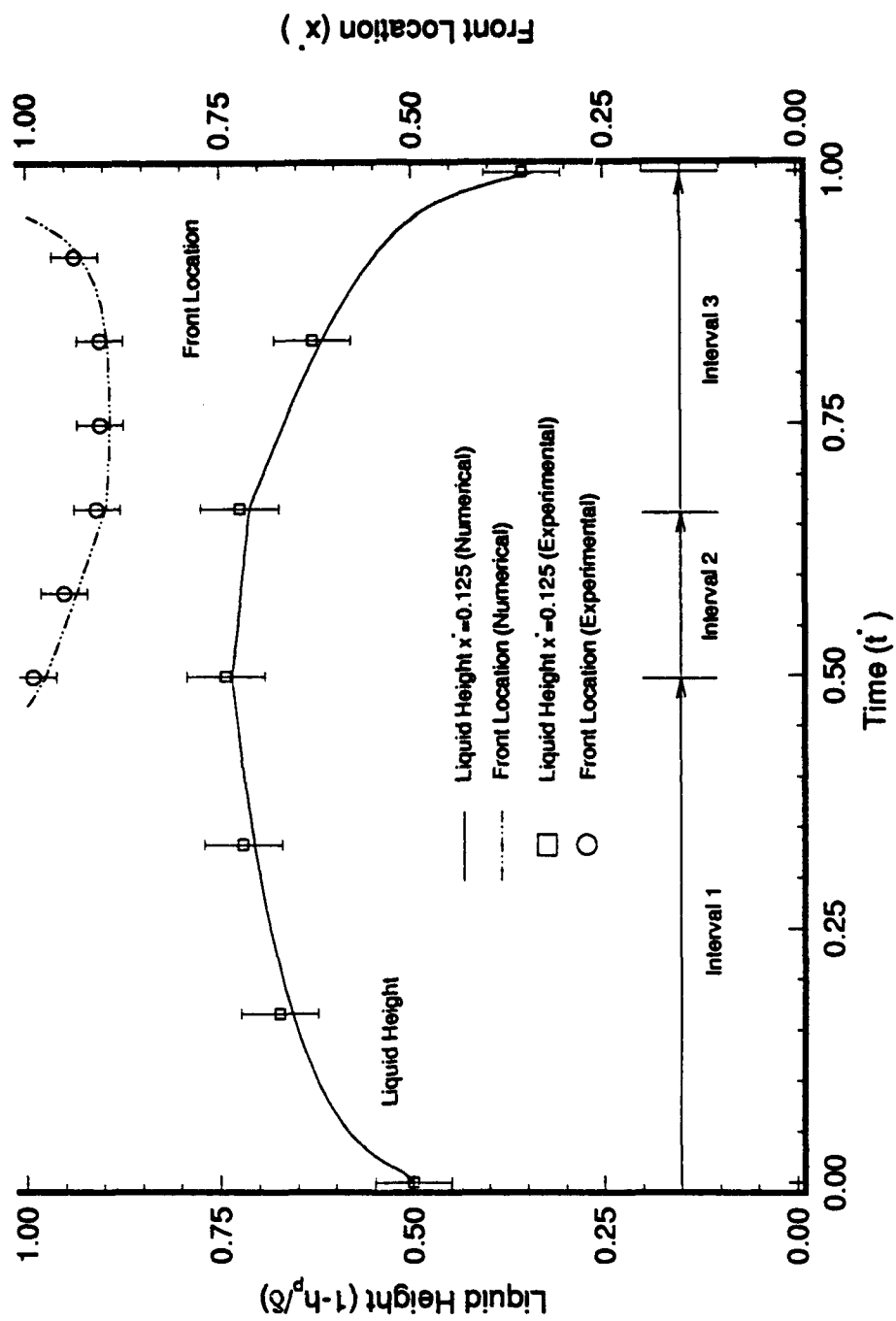
5-19

Figure 5-19. Power-Off Test Results

value that would be attained in the absence of any momentum or transient body force-induced motion. The important thing to note is that the value, $h_l = 0.34$, at the end of the test run is below the value at the beginning of the test run (0.50 vs. 0.34). This is indicative of evaporation occurring in the absence of any external heat transfer.

The squares on Figure 5-19 represent the average of the measured liquid heights from two experimental data runs. The vertical lines on the liquid height curve represent the uncertainty associated with the depth gauge measurement (± 0.08 mm). The numerics capture the correct trends and properly model the behavior of the liquid flow in the groove within the uncertainty of the measurements.

There appears to be a bias in the liquid height experimental data in a direction above the numerical data. This means that the experimentally measured liquid height is greater than that predicted from the numerics. This could be caused by several factors.

One could be an overprediction of the friction. If the actual friction in the groove was less than that predicted from the analytical model, there would be less restriction to the liquid motion. This means more liquid would flow towards the gauge and higher liquid heights would be recorded, as noted in the figure.

Another explanation could be related to the depth gauge measurement itself. Since the depth gauge is always lowered from above the liquid to a position just above the liquid surface, and because the gauge could never come in contact with the liquid surface, there was most likely a tendency to stop the guage motion early. This would lead to experimental values greater than those predicted from the numerics, as noted in the figure.

Still another explanation could be an error in the evaporation model. If the evaporation model overpredicted the evaporation rate of ethanol, then more liquid would leave the groove through the numerical model than was actually being lost by physical processes. This would explain the bias seen in the liquid front data.

5-21

Most likely, the answer is a combination of the three explanations described above. As will be seen later in this chapter, the numerical model is most sensitive to errors in the evaporation model.

The dashed line on Figure 5-19 represents the front position as predicted from the numerics. From the figure, the beginning of dryout is predicted at the end of Interval 1 and continues through Interval 2 into Interval 3. The numerics show that as the rotation back to level is begun, $t^* = 0.67$, the liquid responds immediately and the rewet is completed at $t^* = 0.96$. The maximum distance the front travels into the groove, defined here as the extent of dryout, is approximately $x^* = 0.88$ and occurs at $t^* = 0.76$.

The circles on Figure 5-19 represent the average of the measured front locations from the same two experimental data runs. The vertical lines on the front location curve represent the uncertainty in the front location measurement ($\pm$ 5 mm). Here also, there appears to be a bias in the experimental data in a direction above the numerical front locations; however, this bias seems less pronounced than the bias in the liquid height data. This seems most likely tied to an inaccurate evaporation model. If the evaporation were overpredicted, as suspected in the liquid height data, then more liquid would be lost from the groove and the extent of dryout would be enhanced, as seen in Figure 5-19.

Again, the numerics capture the correct trends and properly model the behavior of the liquid front in the groove within the uncertainty of the measurements.

Power-On Test. Figure 5-20 shows the results from the power-on test. The axes and their definitions are identical to those discussed for the power-off test. From this figure, the initial time of dryout occurs earlier than for the power-off test, ($t^* = 0.4$ vs. $t^* = 0.45$), full rewet occurs later than the power-off test, ($t^* = 1.0$ vs. $t^* = 0.96$), and the extent of the dryout is more pronounced than the power-off test,
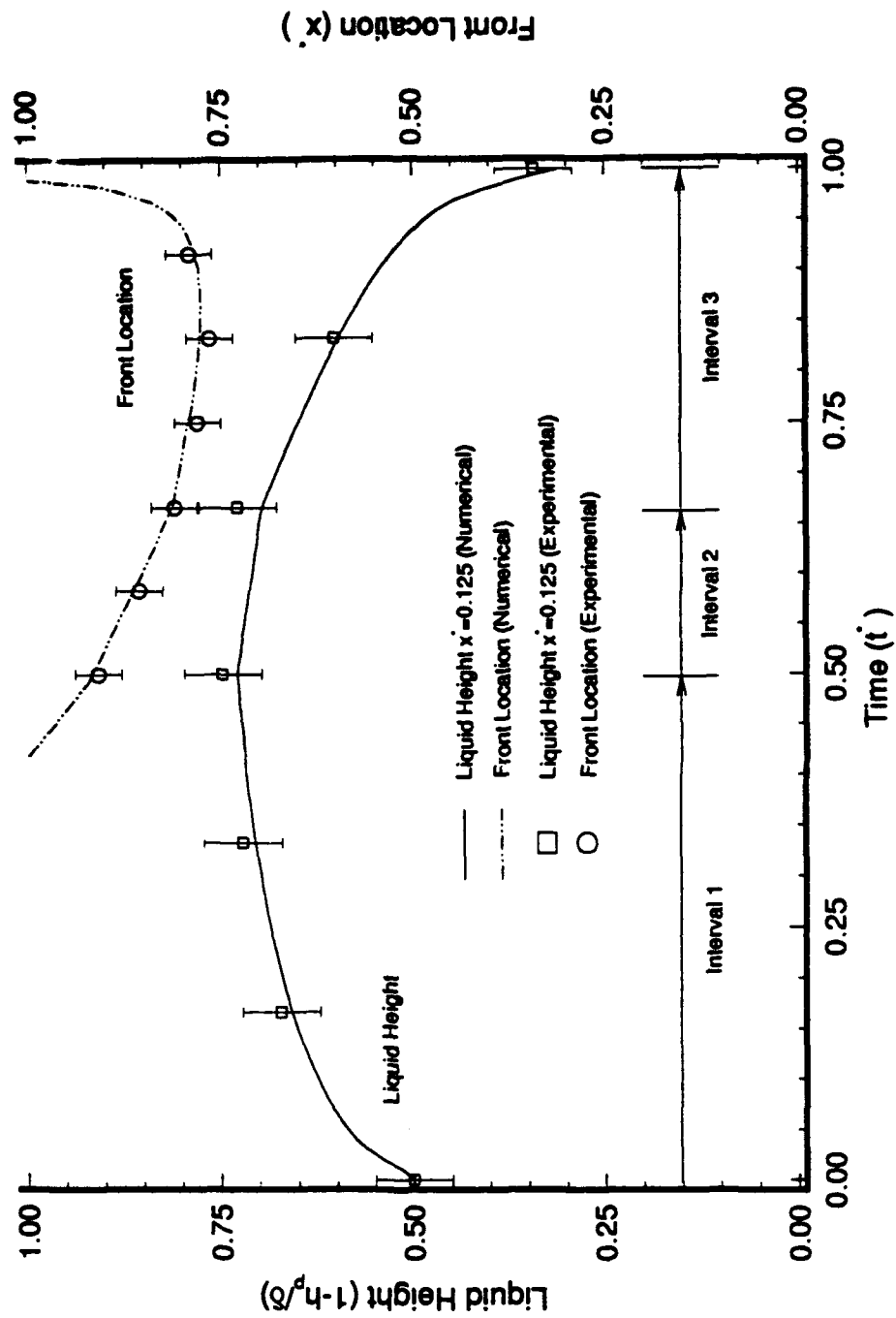
Figure 5-20. Power-On Test Results

($x^* = 0.77$ vs. $x^* = 0.88$). Definitions of the experimental quantities and the associated uncertainties are also identical to those discussed for Figure 5-19. Again, the numerics capture the correct trends and properly model the behavior of the liquid front in the groove within the uncertainty of the measurements.

To get a full appreciation for the differences between the two cases, each curve was plotted against the other and the result is seen in Figure 5-21. In this figure, the solid lines represent the power-off numerical results and the dashed lines represent the numerical power-on data.

Comparing the liquid height curves, the power-off data lies above the power-on data with the most deviation occurring in Intervals 2 and 3. There is a three percent maximum difference between the two curves. The reason is due to the increased evaporation in the power-on test due to the increased liquid temperatures caused by the external heating. The two curves do not deviate until Interval 2 because of the time required to increase the liquid temperature in the groove.

Comparing the front location curves yields a different result. Here the effect of the external heating is more evident. The first difference is the time at which the initial dryout first occurs; earlier in Interval 1 for the power-on test. The second difference is the rate at which the dryout progresses; for the power-on test, the rate of dryout is greater than for the power-off test as evidenced by the steeper slope of the front location curve. The third difference is the extent of the dryout; 11 percent greater for the power-on test. Each of these is explained by the increased evaporation rate caused by the external heating of the groove.

Another difference between the two front location curves is the behavior of the front during Interval 3. In the power-off test, the front begins to recover and rewet the groove immediately, whereas the front in the power-on test continues its dryout of the
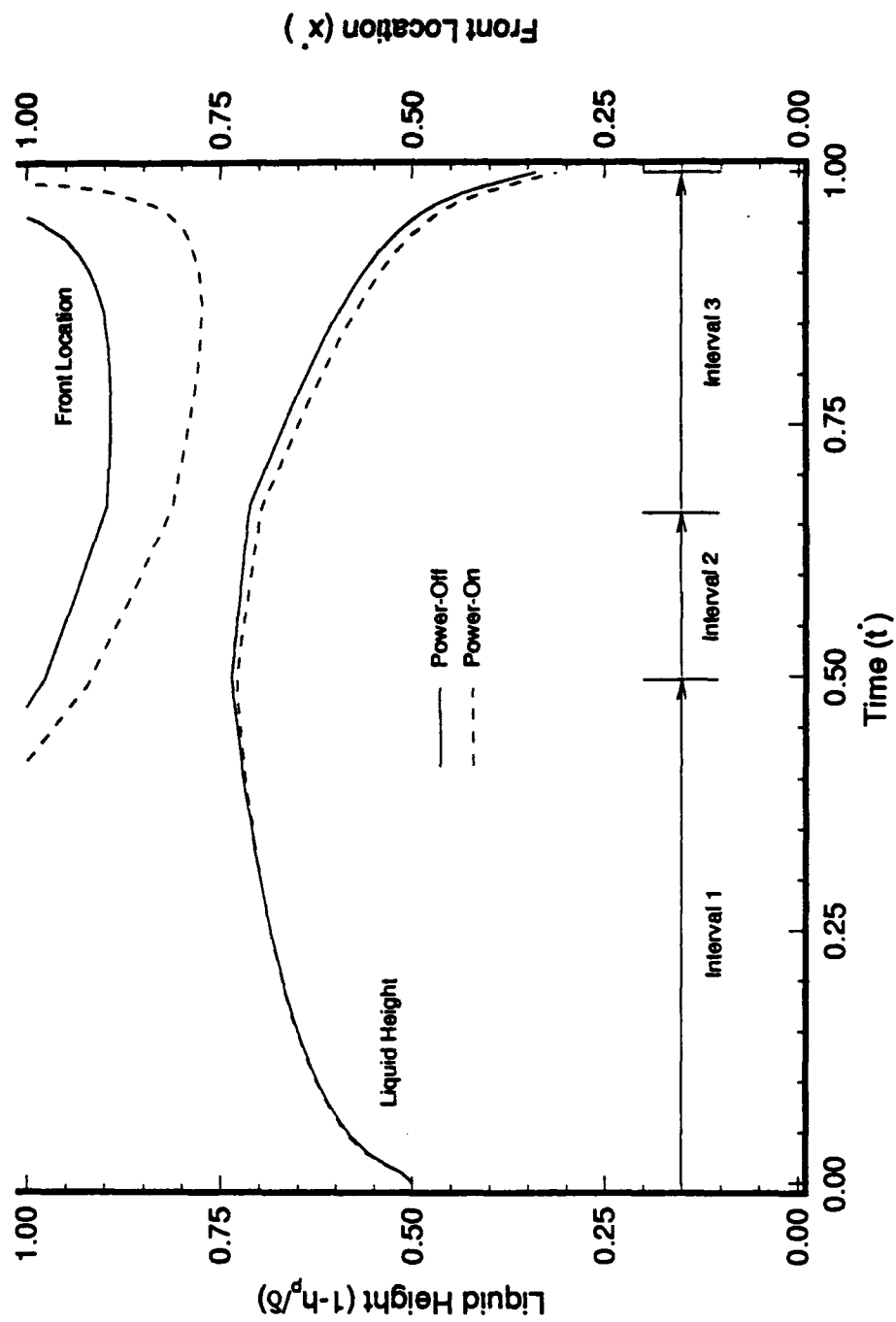
Figure 5-21. Comparison Between Power-Off and Power-On Tests

groove until approximately $t^* = 0.90$. At this point, the front reverses direction and begins to rewet. This behavior is also caused by the external heating; the dryout that occurs in the power-on test causes the groove in the dried out region to heat up faster than those areas of the groove that still have ethanol in them. When the groove is lowered and the ethanol begins to rewet the hot groove surface, the amount of liquid that evaporates is greater than that being supplied by the bulk liquid motion due to the transient body force generated by the lowering of the groove. However, once sufficient momentum is generated by the body force, the front reverses direction and the rewet begins until full rewet occurs at approximately $t^* = 0.99$.

Sensitivity Study

A study was conducted to determine the sensitivity of the numerical solution of the power-on test presented above, to inaccuracies in the quantities that were experimentally measured, to determine the relative importance of the terms in the governing equations and finally, to determine the sensitivity to the numerical grid.

Experimental Sensitivity. The three quantities that were measured in the experiment and input to the code were the ethanol mass flow, the groove tilt angle and the groove temperature. By looking at the sensitivity of the solution to errors in the measured input quantities, a determination could be made as to whether or not the accuracy of measuring these quantities was acceptable for the work.

The experimental sensitivity study consisted of three computational runs, one run for each experimentally measured variable described above. Each run increased the experimental quantity by a percentage that approximated the experimental uncertainty of that quantity. For example, consider a baseline temperature measurement of 300 K to be valid to ± 1 K; this is approximately 0.5 percent. For the temperature sensitivity study,

then, the groove temperature input to the code would be the measured baseline plus 0.5 percent.

A point by point comparison was made against the baseline data to determine the sensitivity of the solution to the uncertainty. If the baseline solution changed by more than the measurement error, then the validity of the baseline solution would be suspect.

Because interest in this study was primarily on differences in trends from a baseline, a coarser grid (25 nodes) than that used for the initial runs (97 nodes) was utilized. It was assumed that trends discovered using the coarser grid were valid for the more refined grid.

The mass flow was the first quantity evaluated. Its value was perturbed plus ten percent from its established curve-fit at all temperatures; this approximated the experimental uncertainty in the mass flow between 295K and 315K. Figure 5-22 is a comparison of the error associated with the perturbed mass flow; the solid line refers to the baseline and the dotted line refers to the perturbed values. The axes definitions are identical to those described for Figure 5-19 through Figure 5-21.

From the figure the perturbed data lies consistently below the baseline data. Because of the increased mass flow, the liquid height curve is lower at all times throughout the test; the maximum deviation is approximately two percent. This is within the uncertainty of the experimental measurement of the liquid height, which is approximately ten percent.

The front location curve lies below the baseline front location curve and is also a result of the increased mass flow. The maximum error in the front location due to the perturbed mass flow is approximately four percent. This difference is also within the experimental uncertainty of the front measurement, which is approximately seven percent. In each case, the ten percent change in the mass flow measurement does not alter the
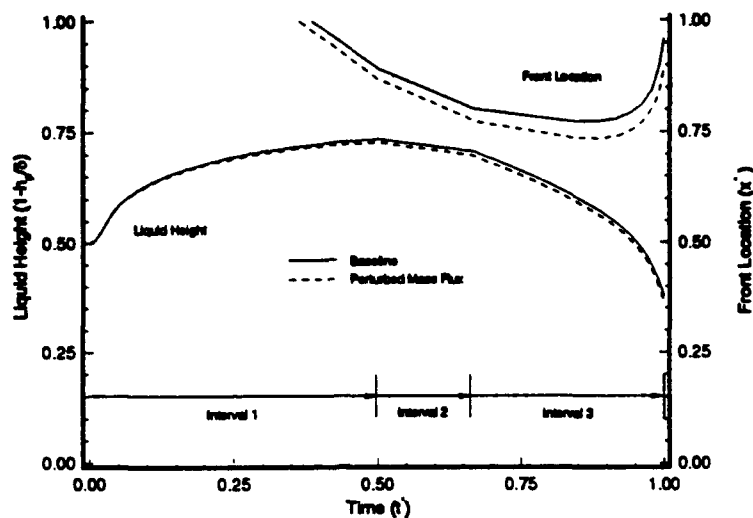
Figure 5-22. Sensitivity Study--Ethanol Mass Flux

baseline solution more than the uncertainty of the respective uncertainties. Therefore, unless the accuracy of the depth gauge or the front location measurement is improved, there is no need to improve the mass flow measurement.

The second quantity to be evaluated was the groove tilt angle. In this case, a plus five percent perturbation in the angular measurement was sufficient to capture the uncertainty. Figure 5-23 shows the comparison between the baseline and perturbed angular data. In this case, the liquid height curve for the perturbed case lies above the baseline. The reason for this is due to the increased rotation of the groove. The maximum difference in this measurement is approximately one percent and again is within the uncertainty of the liquid height measurement.

The front location for the perturbed case lies below the baseline curve as it did for the mass flow case. The reason for this is also due to the higher tilt of the groove. The
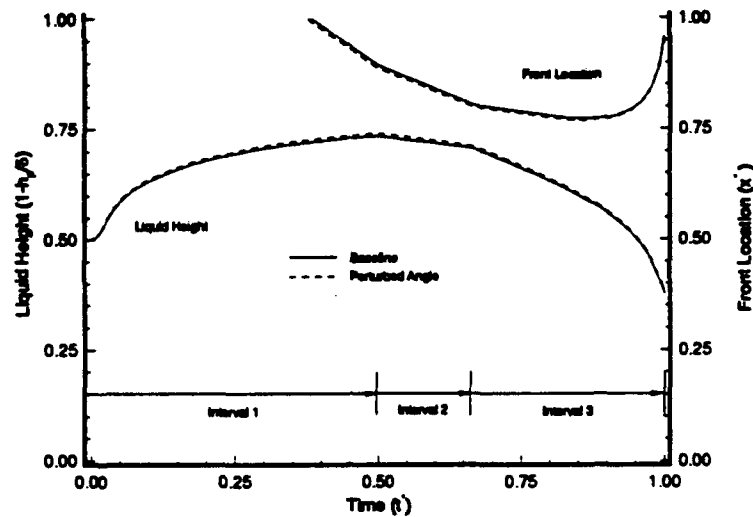
Figure 5-23. Sensitivity Study--Groove Tilt Schedule

maximum difference between these curves is less than one percent and is within the experimental uncertainty of the front location measurement. Again, in either case, unless the accuracy of the depth gauge or front location data is improved, there is no need to improve the accuracy of measuring the groove tilt angle.

The final quantity to be explored was the groove temperature. During the actual testing, groove temperatures between 295 K and 315 K were observed and recorded. The accuracy of the thermocouples was ±1 K. Because of this, a perturbation of plus 0.5 percent was used to model the uncertainty. The results of this study are seen in Figure 5-24.

This curve appears similar to the mass flow sensitivity study and indeed it is. The increase in groove temperature equates to an increase in the mass flow. Because of this,
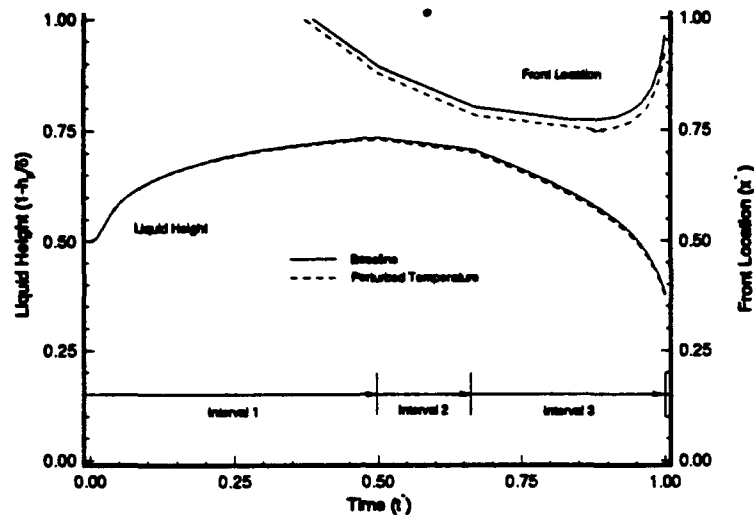
Figure 5-24. Sensitivity Study--Groove Temperature Schedule

the liquid height curve for the perturbed temperature lies below the baseline; the maximum difference is approximately one percent.

The front location line for the perturbed case also lies below the baseline; its maximum deviation is approximately two percent. This is lower than for the mass flow sensitivity study. From this, the same conclusion for the mass flow study is applicable here; namely, the inaccuracy in the temperature measurements is insignificant compared to the inaccuracy of the depth gauge and front location measurements.

To summarize, the inaccuracies of the variables used as input to the code were less than the uncertainties associated with the measurement of the liquid height and the front location. The error in the mass flow measurement causes the most deviation from the baseline solution. The evaporation, groove tilt and groove temperature models used in

this study did not introduce errors greater than those associated with measuring the liquid height and front location.

Equation Sensitivity. This section presents the results of two numerical sensitivity studies. The first study investigated the sensitivity of the solution to changes in the terms comprising the source term, S, in the governing equations. This was done to determine which terms could be neglected and which terms could not. The second numerical study was performed to determine the sensitivity of the solution to changes in the analytical friction and heat transfer models used in this work.

Source Term. The first study investigated the sensitivity of the solution to the source term, S. The terms of interest were the body force term, the capillary force term and the fictitious acceleration term. The mass flow term was not included because its importance to the problem was obvious and could not be summarily dismissed. Each test was accomplished by zeroing out the term of interest and running the code using the baseline experimental quantities. Each test in this first study is now discussed.

Figure 5-25 shows the comparison between the no body force case and the baseline. By removing the groove tilt, the only method of moving liquid is by evaporation. Because of the lack of any tilt, the liquid height curve for the no tilt case does not follow the baseline; in fact, the reason there is any decrease is due entirely to evaporation. The maximum error is approximately 37 percent. The figure shows no dryout front for the no tilt case which was not indicated from the experiment. Based on these observations, the body force term can not be neglected.

Figure 5-26 shows the comparison between the no capillary force solution and the baseline. By neglecting the capillary term, the momentum of the liquid is not retarded and its motion towards the center of rotation ($x^* = 0$) is enhanced over that of the baseline. This equates to more liquid flowing towards the depth gauge, which results in
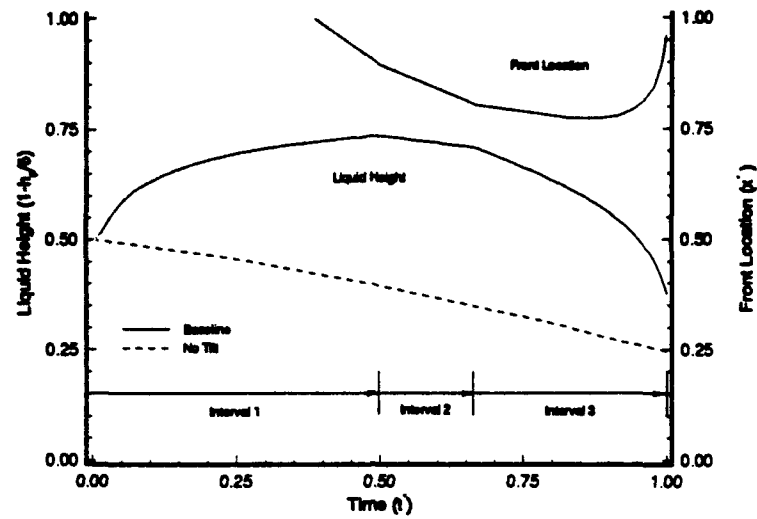
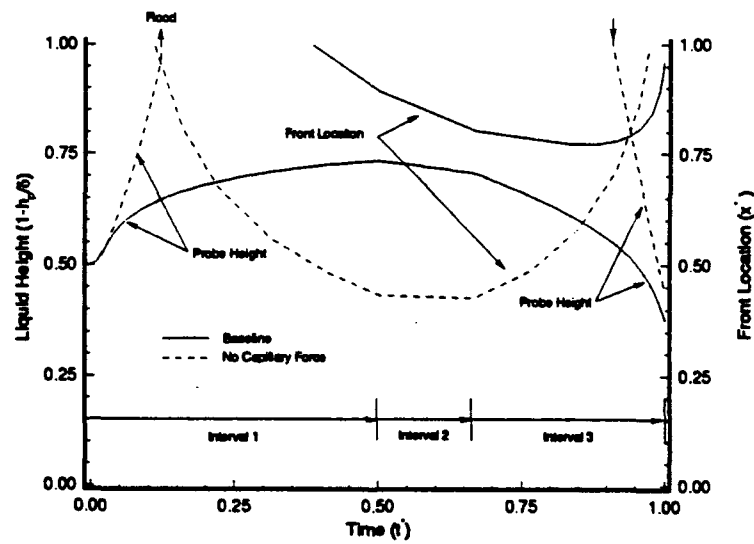**Figure 5-25.** Sensitivity Study--No Tilt

Figure 5-26. Sensitivity Study--No Capillary Force

5-32

a higher liquid height as seen in the figure. In fact, without the capillary force term, the numerics predict a condition where the cross-sectional flow area at $x^* = 0$ is greater than unity. This is a flood condition seen on the figure at $t^* = 0.15$. This condition does not relieve itself again until $t^* = 0.92$; a trend not indicated from the experiment. The maximum error in the liquid height is greater than 50 percent.

The lack of the capillary force term also results in the extent of dryout being greater than the baseline as evidenced by the front location curves on Figure 5-26; a trend also not indicated from the experiment. Dryout occurs earlier ($t^* = 0.10$ vs. $t^* = 0.40$) and the extent of dryout is more severe ($x^* = 0.43$ vs. $x^* = 0.77$). The maximum error in the front location is approximately 50 percent. The reason for this behavior can be seen by investigating the relative magnitudes of the capillary and body force terms.

The body force per unit mass is $F_B = g \sin\psi + \Omega^2 r$. Using the maximum angle in this study, F_B is approximately 0.51 m/s². The capillary force per unit mass is $F_C = \dfrac{\sigma A}{R \rho \forall}$. Assuming a groove full of ethanol, F_C is approximately 0.22 m/s². Since these are order of magnitude close, the capillary force term may not be neglected in the analysis. The result of doing so was seen in Figure 5-26.

It is hypothesized that as long as the capillary force term is on the order of the body force term, its impact on the liquid motion in a capillary structure will be important. Further work is necessary to quantify and validate this hypothesis. Based on these observations, the capillary force term can not be neglected in this analysis.

The final comparison dealt with the fictitious acceleration term. Figure 5-27 shows that for this particular angular schedule, the impact of the fictitious term is negligible for both the liquid height and front location curves. This is only true because of the length of the groove structure and the rotation rates involved in the experiment. Since the fictitious term varies linearly with distance from the center of rotation and
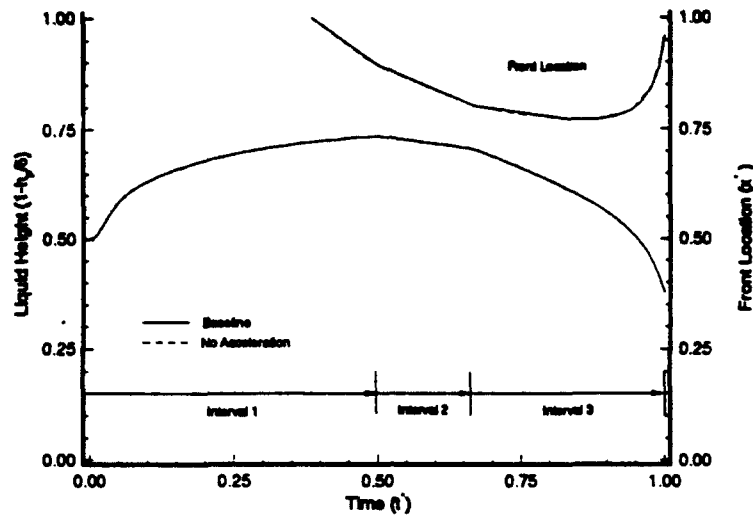
Figure 5-27. Sensitivity Study--No Acceleration

linearly with the square of the rotation rate, either a long groove structure or a high rotation rate would be needed to increase the magnitude of this term to the order of the body force term. For this experiment and conditions only, the fictitious acceleration term is negligible and can be neglected; however, this statement cannot be applied universally to every case. This term should therefore always be included in the analysis.

Friction. To determine the sensitivity of the governing equations to the friction model chosen in this work, the code was run with the baseline conditions but the friction coefficient was perturbed one order of magnitude greater than the value used in the baseline run. Figure 5-28 shows the results of this study. The liquid height curve for the perturbed friction lies below the baseline by less than one percent over the entire run. The perturbed curve should lie below the baseline since the increased friction retards the liquid motion over that of the baseline.

5-34
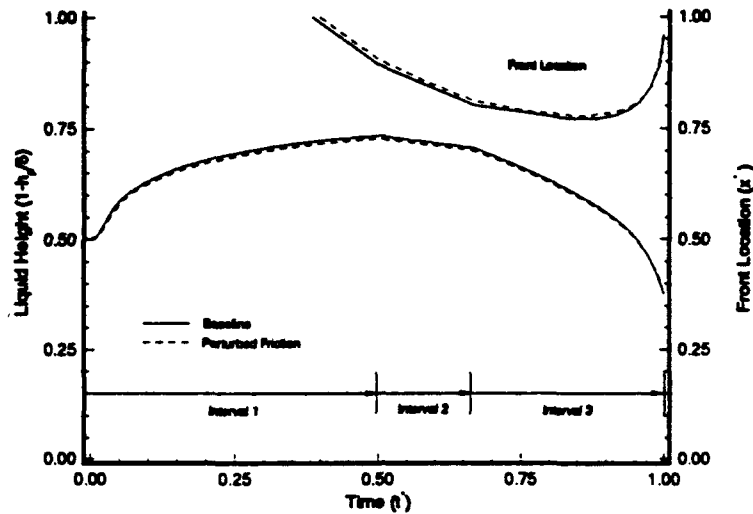
Figure 5-28. Sensitivity Study--Friction Model

The front location curve for the perturbed case lies above the baseline; the difference between the baseline is also less than one percent. This curve should lie above the baseline since the increased friction keeps more liquid in the end of the groove near $x^* = 1$. Based on these observations, the governing equations do not appear to be sensitive to the friction model.

Heat Transfer. To determine the sensitivity of the governing equations to the heat transfer model chosen in this work, the code was run with the baseline conditions but the heat transfer coefficient was perturbed one order of magnitude greater than the value used in the baseline run. Figure 5-29 shows the results of this study. The liquid height curve for the perturbed friction lies on the baseline; the error is less than one percent over the entire run. Theoretically, the perturbed curve should lie below the

5-35
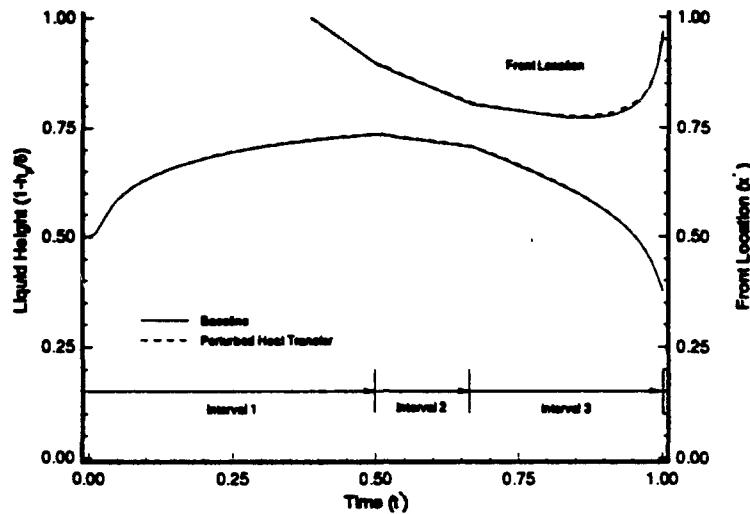
Figure 5-29. Sensitivity Study—Heat Transfer Model

baseline since the increased heat transfer should increase evaporation and reduce the total liquid volume in the groove.

The front location curve for the perturbed case also lies on the baseline; the difference between the baseline is less than one percent. This curve should also lie below the baseline for the same reason given above.

The reason the governing equations are not sensitive to the heat transfer model is due to the fact that the evaporation model from Chapter IV is not sensitive to temperature over the range investigated in this study (295 K to 315 K). While the increased heat transfer coefficient results in the liquid getting hotter faster, the rate of change in the evaporation model with respect to temperature varies by less than 0.0025 percent. Since the change in evaporation is negligible, the overall liquid volume is not affected; hence the small deviations (less than one percent) noted in the figure. It is suspected that if

temperatures closer to the boiling point of ethanol are investigated, where the evaporation model is more sensitive to temperature, more deviation from the baseline would be noted. Further work is necessary to validate this hypothesis. Based on these observations for the temperature range studied, the governing equations are not sensitive to the heat transfer model.

Grid Sensitivity. The cross-sectional flow area was chosen as the primary tool in determining whether or not a specific grid was sufficiently refined. This was done after several numerical runs which showed that this variable was the most sensitive to changes in grid size. In order to proceed with the grid study, a definition of sufficiently refined was required.

A grid was considered sufficiently refined when the maximum difference between cross-sectional flow areas at the current grid and the previous grid remained below one percent for two successive calculations. In other words

$$\Delta A_{max} = \left| \frac{A_i^{new} - A_i^{old}}{A_{cl}} \right| \leq 0.01 \qquad [5\text{-}2]$$

A^{old} is the most previous grid; A^{new} is the current grid and is obtained by doubling the grid size of A^{old}. When the criteria established above was satisfied, the excess computational overhead associated with the finer mesh, A^{new}, was deemed too costly and the grid associated with A^{old} was used.

The grid study was performed on a representative problem, simulating conditions in the experimental study. Early numerical studies showed that groove rotation rate, Ω , was the most demanding condition for the numerics and therefore, the maximum rate experienced in the physical experiments was chosen for the grid study. Temperature profiles and initial conditions were also chosen to match the experimental conditions. A summary of the study parameters is shown in Table 5-1. The grid study was run for sixty

Table 5-1. Initial Conditions for Groove Grid Study

$$
\begin{aligned}
A_i &= 1.5305 \times 10^{-6} \ \ \text{m}^2 \\
V_i &= 0.0000 \times 10^{+0} \ \ \text{m/s} \\
T_i &= 2.9500 \times 10^{+2} \ \ \text{K} \\
T_s &= 2.9500 \times 10^{+2} \ \ \text{K} \\
\psi_i &= 0.0000 \times 10^{+0} \ \ \text{rad} \\
\Omega_i &= 4.3633 \times 10^{-4} \ \ \text{rad/s}
\end{aligned}
$$

seconds real time to allow the liquid motion to develop and also to allow liquid to flow into the critical regions discussed previously. This was done to establish the influence of the capillary action which, in turn, affected the liquid distribution within the groove.

The working grid for debugging and initial data runs was 25 nodes in length and was used as the base grid. Grid sizes of 49, 97 and 193 were also investigated. Comparisons between grids 25-49, 49-97 and 97-193 were accomplished and the results shown in Table 5-2.

Table 5-2. Results of Groove Grid Study

Grid Improvement	ΔA_{max}
25→49	0.01370
49→97	0.00956
97→193	0.00922

From this table, the percent difference in flow areas decreases as the grid size increases. Since the maximum difference in areas between grids 97 and 193 was less

than one percent for two successive runs, a 97 node grid was determined to be adequate to capture the physics of the groove problem under the conditions in the experiment.

Model Comparison

To gain a full appreciation for the value of this new model, a comparison is made with the Beam piston model described in Appendix A. Because the Beam piston model was developed to be used in a heat pipe environment and because the experiment in this work was not designed as a heat pipe, a direct comparison to the experimental data was not possible. However, a numerical experiment between the two models was possible and these results were used as a basis of comparison.

Consider a setup similar to the experiment discussed in Chapter IV except the plate on the end of the groove structure closest to the center of rotation is removed. In its place, assume that some mechanism exists that automatically maintains the cross-sectional flow area at a value of $A^* = 1$ and at some specified velocity, V^*, that is known. Also assume that the initial conditions, ethanol evaporation model, groove heating and groove rotation schedules are similar to the experiment of Chapter IV.

The discussion in Appendix A on the piston model applies here with two differences. The first difference is that x_0 is situated at the center of rotation instead of half way down the groove as depicted in Figure A-1, which means that the initial distance in the model is the groove length, L_∞. The other difference is that an additional term must be added to Eqn [A-9] to account for the body force term, since the Beam piston model does not account for body forces. The modified piston equation is

$$\frac{dx}{dt} = \frac{r_h^2}{\mu(f \cdot Re)}\left[\frac{\sigma}{R_{min}x} - \rho g \sin\psi\right] - \frac{\dot{m}_e}{\rho A_w} \qquad [5\text{-}3]$$

where the extra term, $\rho g \sin\psi$, accounts for the body force. This equation was solved using first order finite differencing with values of the groove tilt schedule, groove heating schedule and evaporation rate being supplied by the new model. Both codes were run for 360 seconds on a 25 node grid. The results presented below are snapshots of the liquid distribution within the groove structure at specific times throughout the transient.

Figure 5-30 shows the liquid distribution along the groove at $t^* = 0.129$, which is in Interval 1. The horizontal axis is non-dimensional distance along the groove and the vertical axis is non-dimensional cross-sectional flow area. Note that at $x^* = 0$ the flow area is maintained at $A^* = 1$; the specified boundary condition. At this time in the transient the groove is approaching its maximum tilt angle. Neither the modified piston model or the new model predicts dryout, but the new model shows a seven percent recession at $x^* = 1$.

Figure 5-31 shows the liquid distribution at $t^* = 0.378$, which is over two minutes into the transient and is still in Interval 1. At this point, the modified piston model predicts a dryout condition with the extent of dryout being approximately $x^* = 0.66$. The new model, on the other hand, shows no dryout but simply a recession of the liquid along the groove with maximum recession at $x^* = 1$ of approximately 20 percent.

Figure 5-32 shows the liquid distribution at $t^* = 0.626$, which is under the four minute point in the transient which is in Interval 2. The modified piston model continues to predict a dryout condition with the front at $x^* = 0.46$. The new model shows further recession into the groove, more than 35 percent at $x^* = 1$, but no dryout.

Figure 5-33 shows the liquid distribution at $t^* = 0.825$; almost 5 minutes into the transient, which is in Interval 3. The modified piston model predicts a partial rewet with the front located at a position of $x^* = 0.76$. The new model, on the other hand, continues to predict recession into the groove structure and at this point, the recession at $x^* = 1$

Figure 5-30. Comparison between Beam Piston Model and New Model--t^*=0.129

Figure 5-31. Comparison between Beam Piston Model and New Model--t^*=0.378

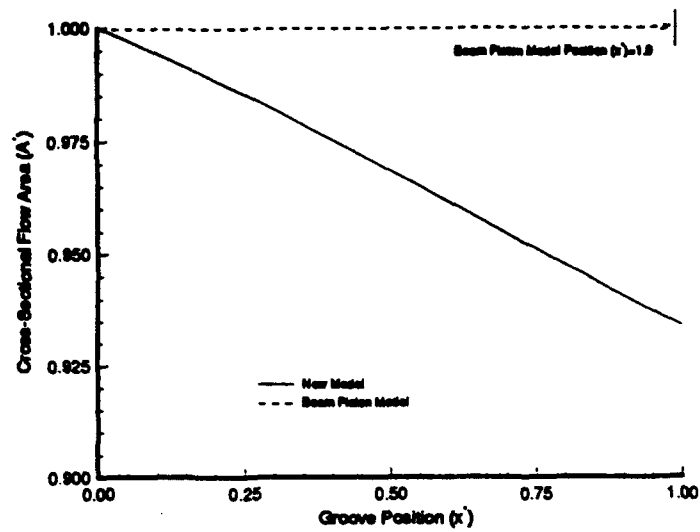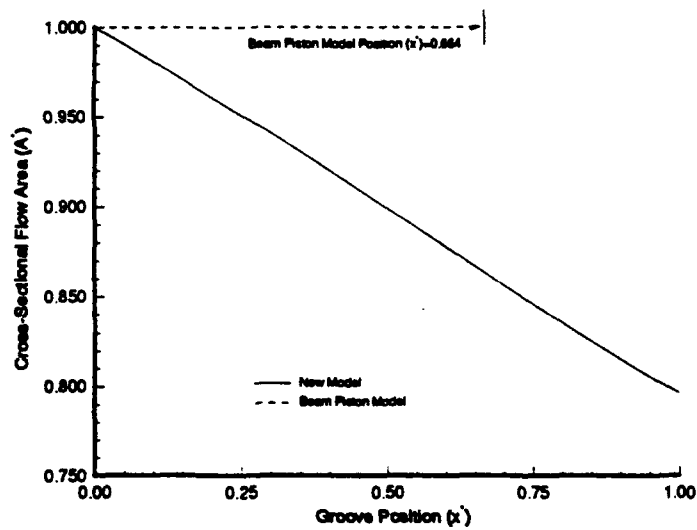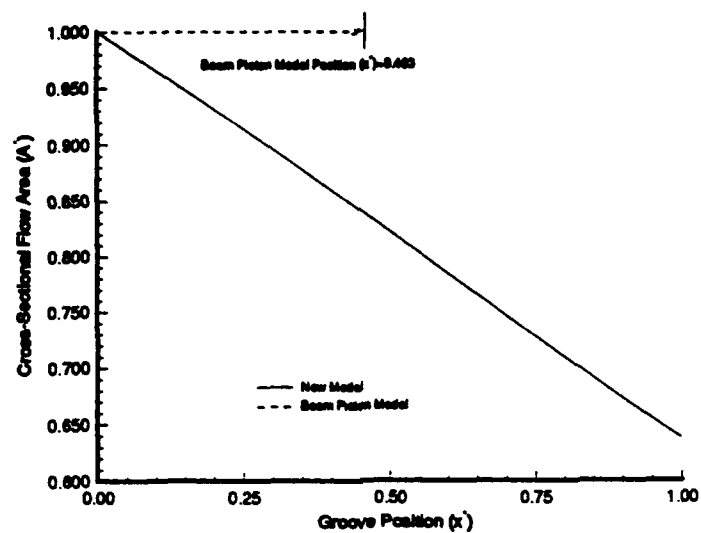**Figure 5-32.** Comparison between Beam Piston Model and New Model--t^*=0.626
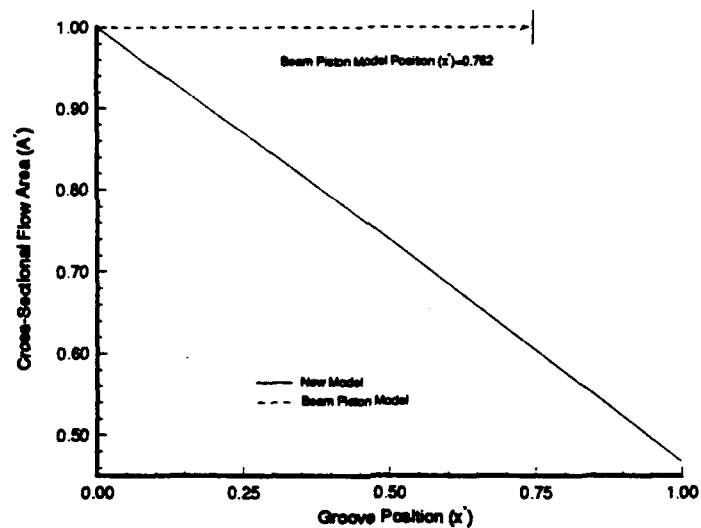
Figure 5-33. Comparison between Beam Piston Model and New Model--t^*=0.825

exceeds 50 percent. The entire groove, however, is still wet and dryout never occurs during the entire transient.

The reason for this behavior is due to the assumption in the piston model of the planar front. Because the model does not allow for liquid recession, the groove at any axial location either has liquid in it or it is dry. The recession that is evident in the new model is not allowed to occur and because of this, the modified piston model shows dryout whereas the new model accounts for the phenomenon with recession along the length of the groove. This is the value of the new model.

By allowing for recession along the groove, the new model more accurately predicts the liquid distribution along the groove and more accurately determines the position of the dryout and rewet fronts. In this particular example, the modified piston model predicts dryout along the groove for the majority of the transient whereas the new model predicts no dryout, but a recession of the liquid into the groove structure.

VI. *Conclusions and Recommendations*

Conclusions

This work was undertaken to show that the liquid distribution, including dryout and rewet, in a heated capillary structure, subject to transient body forces could be accurately modeled. This thesis has been substantiated.

Governing equations describing conservation of mass, momentum and energy were developed for liquid flow in an axial, square groove. Variable recession of the liquid meniscus into the groove, shear and heat transfer between the groove wall and the liquid, evaporation and transient body forces were accounted for in the model. An analytical model was developed for the shape of the liquid front. The governing equations were numerically solved using a first-order explicit method.

A physical experiment was performed that subjected ethanol within a stainless steel groove structure to a maximum transient body force of 0.51 m/s^2. The transient body force was generated by varying the tilt of the groove with time. The frequency of the body force was varied between 2.8 mHz and 4.2 mHz. The ethanol cross-sectional flow area, and dryout and rewet front location were measured.

Based on the numerical and physical test results from Chapter V, the following conclusions are drawn:

--Transient body forces can influence the liquid motion in a heated capillary groove. This conclusion is based on the results from the numerical and physical tests which showed bulk liquid motion for transient body forces up to 0.51 m/s^2 .

--The influence of transient body forces can cause a dryout of the heated groove structure; these same body forces can also effect a rewet of the same dried out structure.

This conclusion is based on the numerical and physical results which showed that transient body forces of 0.51 m/s^2 at frequencies up to 4.2 mHz caused a twenty percent dryout followed by full rewet.

--The dryout and rewet caused by transient body forces may be accurately modeled using numerical techniques. This conclusion is based on the agreement between the numerical and physical experiments which was within the experimental uncertainty.

--It is important to include the body and capillary forces in the analysis, as well as the fictitious acceleration terms. This conclusion is based on the results of the sensitivity studies which showed the importance of these terms and the result of not including them in the analysis.

--The new model predicts the liquid distribution in a groove and the position of the front during a transient body force-induced dryout and rewet more accurately than existing models. This conclusion is based on the results of the comparison of the new model with the Beam piston model.

Recommendations

Based on the results from this work, several recommendations are suggested. These are divided into two types; those dealing with improvements and modifications to the experiment and those dealing with improvements and upgrades to the computer code.

Because of the no flooding restriction, the maximum angular rate that could be tested was limited to approximately 0.44 mrad/sec. To explore higher angles and higher rotation rates without exceeding the no flood condition, a groove structure with an aspect ratio greater than one (i.e., a groove structure deeper than wider) should be constructed and tested in a manner similar to this experiment. This would provide valuable

information on the capabilities of the current code to handle transient body forces beyond the 0.51 m/s^2 limit of this study.

The code predicted dryout and rewet in a groove that was heated to temperatures that were 30 K below the boiling point of ethanol. Higher temperatures should be investigated to determine their effect on the dryout and rewet phenomenon, the validity of the heat transfer model and evaporation models, and the code capability at the higher evaporation rates. It is suspected that temperatures approaching the boiling point of ethanol would significantly hinder the rewet phenomenon, possibly to the point of not allowing a rewet to even occur. While the code should predict this behavior, experimental confirmation would provide added credence to the model.

It was demonstrated that dryout and rewet could be experimentally studied and numerically modeled in a groove structure. Further studies should investigate means of delaying the dryout and enhancing the rewet, not only in these geometries, but others as well. The computer code would prove extremely useful in estimating the relative performance of these different structures prior to their construction.

Concerning improvements and upgrades to the current code, the following are recommended. Since flooding of a capillary-driven evaporator or a heat pipe is an expected phenomenon in a transient body force environment, a flooding model should be developed. This would allow the current groove structure to be rotated to higher angles than were studied in this work.

The current code utilizes a linear model for the liquid front and the comparison between experiment and the numerics and was within the experimental uncertainty. A second order front model was mentioned but not investigated. As higher rotation rates are considered, the shape of the front may experience some changes. For example, during a dryout the first order model may be a good approximation; however, during the rewet,

a second order (or higher) model may be more appropriate than the linear model. Some preliminary observations on the general shape of fronts during these higher rotation rate tests is warranted.

The current code utilizes an explicit, first order accurate scheme which suffers from a small timestep restriction. Effort should be expended into developing and validating an implicit version of the code. This would serve to reduce the amount of processing time required to generate results. For example, experimental run times for this experiment were on the order of minutes, while computer runs required approximately 24 hours on a Silicon Graphics workstation. An implicit scheme would increase the allowable timestep and reduce the overall run times.

Finally, this new model should be coupled to both a heat pipe vapor model and a heat pipe wall model to simulate a complete heat pipe. Since validating the performance of such a device in a transient body force environment was one impetus for this work, the model should be modified and input into a heat pipe/transient body force scenario. Where possible, actual experimental data should be used and compared to the output of this new model to determine the level of improvement over existing prediction tools.

Bibliography

1. Peterson, G. P. "Heat Pipes in the Thermal Control of Electronic Components," *Proceedings of the 3rd International Heat Pipe Symposium.* Tsukuba City, Japan, September 1988.

2. Yerkes, Kirk L. and Brian G. Hager. "Transient Response of Heat Pipes for Actuator Thermal Management," *SAE Aerospace Atlantic Conference (SAE Paper 921024).* Dayton, Ohio, April 1992.

3. Ponnappan, R. et. al. "Analysis and Testing of Heat Pipe in Accelerating Environment," *Proceedings of the 8th International Heat Pipe Conference.* Beijing, China, September 1992.

4. Müller, Robert. "Analysis of the Liquid Distribution in Capillary Grooves of a SpacePlane Evaporation Cooler," *Proceedings of the 8th International Heat Pipe Conference,* Beijing, China, September 1992.

5. Silverstein, C. C. *"A Feasibility Study of Heat-Pipe-Cooled Leading Edges for Hypersonic Cruise Aircraft,"* NASA CR 1857, November 1971.

6. Camarda, C. J. and R. V. Masek. "Design, Analysis, and Tests of a Shuttle-Type Heat-Pipe-Cooled Leading Edge," *Journal of Spacecraft and Rockets, 18 n 1:* 71-78 (January-February 1981).

7. Camarda, C. J. "Thermostructural Applications of Heat Pipes for High-Speed Aerospace Vehicles," *Proceedings of the 3rd International Heat Pipe Symposium.* Tsukuba City, Japan, September 1988.

8. Colwell, G. T. "Cooling Hypersonic Vehicle Structures," *Proceedings of the 7th International Heat Pipe Conference.* Minsk, USSR, May 1990.

9. Petley, D. et. al. "Analysis of Cooling Systems for Hypersonic Aircraft," *AIAA 3rd International Aerospace Planes Conference (AIAA Paper 91-5063).* Orlando, Florida, 1991.

10. Jones, S. and D. Petley. "A Comparison of Cooling Methods for the Airframe Nozzle of a Single-Stage-to-Orbit Aircraft," *AIAA 3rd International Aerospace Planes Conference (AIAA Paper 91-5036).* Orlando, Florida, 1991.

11. Ribot, J. and R. D. McConnell. "Testing and Analysis of a Heat Pipe Solar Collector," *Journal of Solar Energy Engineering, 105 n 4:* 440-445 (November 1983).

12. Keddy, E. et. al. "Development of an Integrated Heat Pipe-Thermal Storage System for a Solar Receiver," *AIAA 23rd Thermophysics, Plasmadynamics and Lasers Conference (AIAA Paper 88-2683)*. San Antonio, Texas, 1988.

13. Paripatyador, S. A. and J. T. Richardson. "Cyclic Performance of a Sodium Heat Pipe, Solar Reformer," *Solar Energy, 41 n 5:* 475-485 (May 1988).

14. Adkins, Douglas R. "Design Considerations for Heat-Pipe Solar Receivers," *Journal of Solar Energy Engineering, 112 n 3:* 169-176 (August 1990).

15. Crane, R. A. "Evaluation of Thermal Energy Storage Devices for Advanced Solar Dynamic Systems," *Journal of Solar Energy Engineering, 113 n 3:* 138-145 (August 1991).

16. Driver, R. B. et. al. "Solar Test of an Integrated Sodium Reflux Heat Pipe Receiver/Reactor for Thermochemical Energy Transport," *Solar Energy, 48 n 1:* 21-30 (January 1992).

17. Kuramae, M. and Makato Ito. "Some Considerations on Physical Heat Pipe Models for Analyzing Dynamic Heat-Transfer Characteristics," *Heat Transfer-Japanese Research, 20 n 4:* 389-406 (October 1991).

18. Dehart, M. D. and F. R. Best. "Heat Pipe Startup Transient Measurements Including Internal Visual Observations," *AIAA 22nd Thermophysics Conference (AIAA Paper 87-1649)*. Honolulu, Hawaii, 1987.

19. Richardson, J. W. et. al. "Effect of Longitudinal Vibration on Heat Pipe Performance," *Journal of Astronautical Sciences, 17 n 5:* 249-266 (March-April 1970).

20. Symons, Eugene P. *"Wicking of Liquids in Screens,"* NASA TN D-7657, May 1974.

21. Shishido, I. and S. Ohtani. "Working Fluid Distribution Within Heat Pipe Wick," *Proceedings of the 5th International Heat Pipe Conference*, Tsukuba, Japan, May 1984.

22. Gerasimov, Y. F. et. al. "Performance of Heat Pipe with Separate Vapor and Liquid Ducts Rotating in a Gravity Field," *Heat Transfer-Soviet Research, 17 n 4:* 127-130 (July-August 1985).

23. Kiseev, V. M. et. al. "Influence of Adverse Accelerations on the Operation of an 'Antigravity' Heat Pipe," *Journal of Engineering Physics, 50 n 4:* 394-398 (April 1986).

24. Noda, H. et. al. "A Model for the Heat Transfer Limit of a Screen Wick Heat Pipe," *Heat Transfer-Japanese Research, 18 n 3:* 44-57 (May-June 1989).

25. Hendrix, Walter A. *An Analysis of Body Force Effects on Transient and Steady-State Performance of Heat Pipes.* PhD Dissertation. Georgia Institute of Technology, GA, 1989.

26. Charlton, Capt Mark C. "Effect of Transverse Vibration on the Capillary Limit of a Wrapped Screen Wick Copper/Water Heat Pipe." MS Thesis AFIT/GA/ENY/92D-02. School of Engineering, Air Force Institute of Technology (AU), Wright-Patterson AFB OH, December 1992 (AAJ-4635).

27. Hawthorne, Capt Lowell S. "Rewet Performance of a Rectangular Grooved Heat Pipe Wick After Gravitationally Induced Dryout." MS Thesis AFIT/GA/ENY/92D-04. School of Engineering, Air Force Institute of Technology (AU), Wright-Patterson AFB OH, December 1992 (AAJ-4640).

28. Yerkes, K. L. et. al. "Heat Pipe Performance With Transient Heat Flux and Body Force Effects," *Proceedings of the 8th International Heat Pipe Conference.* Beijing, China, September 1992.

29. Huber, Capt Neil F. "Effect of Longitudinal Vibration on the Capillary Limit of a Wrapped Screen Wick Copper/Water Heat Pipe." MS Thesis AFIT/GA/ENY/93D-18. School of Engineering, Air Force Institute of Technology (AU), Wright-Patterson AFB OH, December 1993.

30. NASA Lewis Research Center. Modeling Heat Pipe Performance Under Transient Operation Conditions Workshop-Summary Conclusions, Cleveland, Ohio, 25 September 1990.

31. Holderness, James H. *Operation of a Heat Pipe Beyond the Capillary Limit.* PhD Dissertation. University of Michigan, MI, 1973.

32. Brennan, P. S. and E. J. Kroliczek. *Heat Pipe Design Handbook, Volume 1.* Contract NAS5-23406. Towson, Maryland: B & K Engineering, Inc., June 1979.

33. Beam, J. E. "Transient Heat Pipe Analysis," *AIAA 20th Thermophysics Conference (AIAA Paper 85-0936).* Williamsburg, Virginia, June 1985.

34. Ambrose, J. H. et. al. "Transient Heat Pipe Response and Rewetting Behavior," Journal of Thermophysics and Heat Transfer, 1 n 3 : 222-227 (July 1987).

35. Ambrose, J. H. et. al. "A Detailed Model for Transient Liquid Flow in Heat Pipe Wicks," *AIAA 28th Aerospace Sciences Meeting (AIAA Paper 90-0062).* Reno, Nevada, 1990.

36. Tournier, J. and Mohamed S. El-Genk. "'HPTAM' Heat-Pipe Transient Analysis Model: An Analysis of Water Heat Pipes," *Proceedings of the 9th Symposium on Space Nuclear Power Systems*. 1023-1037. Albuquerque, New Mexico, January 1992.

37. Peng, X. F. et. al. "Rewetting Analysis of Capillary Induced Flow in Circular Channels With Internal Grooves," *AIAA 30th Aerospace Sciences Meeting and Exhibit (AIAA Paper 92-0127)*. Reno, Nevada, 1992.

38. Peng, X. F. and G. P. Peterson. "Acceleration-Induced Depriming of External Artery Heat Pipes," *Journal of Thermophysics and Heat Transfer, 6 n 3:* 546-548 (July-September 1992).

39. Ochterbeck, J. M. et. al. "Acceleration Induced Depriming and Capillary Rewetting of External Artery Heat Pipes: Comparison with SHARE-II Flight Experiment," *AIAA 31st Aerospace Sciences Meeting and Exhibit (AIAA Paper 93-0282)*. Reno, Nevada, 1993.

40. Munson, Bruce R. et. al. *Fundamentals of Fluid Mechanics*. New York: John Wiley & Sons, Inc., 1990.

41. Chi, S. W. *Heat Pipe Theory and Practice*. Washington: McGraw-Hill Book Company, 1976.

42. Murphy, Capt Timothy J. "A Study of Heat Flux Induced Dryout in Capillary Grooves." MS Thesis AFIT/GA/ENY/92D-06. School of Engineering, Air Force Institute of Technology (AU), Wright-Patterson AFB OH, December 1992 (AAJ-4569).

43. Ivanovskii, M. et. al. *The Physical Principles of Heat Pipes*. Oxford: Clarendon Press, 1982.

44. White, Frank M. *Viscous Fluid Flow* (Second Edition). New York: McGraw-Hill Book Company, 1991.

45. Shah, R. K. and A. L. London. *Laminar Flow Forced Convection in Ducts*. New York, Academic Press, 1978.

46. Incropera, F. J. and D. P. DeWitt. *Introduction to Heat Transfer*. New York: John Wiley & Sons, Inc., 1985.

47. Reynolds, William C. and Henry C. Perkins. *Engineering Thermodynamics*. New York: McGraw-Hill Book Company, 1977.

48. Anderson, D. A. et. al. *Computational Fluid Mechanics and Heat Transfer*. New York: Hemisphere Publishing Corporation, 1984.

49. Roe, P. L. "Approximate Riemann Solvers, Parameter Vectors, and Difference Schemes," *Journal of Computational Physics, 43 n 2:* 357-372 (November 1981).

50. Yee, H.C. "A Class of High-Resolution Explicit and Implicit Shock-Capturing Methods," NASA TM-101088, 1989.

51. Beran, Philip S. Class notes distributed in AE 752, Computational Aerodynamics. School of Engineering, Air Force Institute of Technology (AU), Wright-Patterson AFB OH, April 1991.

52. Jen, H. *Summary Report for Axially Grooved Heat Pipe Study.* Contract NAS5-22562. Towson, Maryland: B & K Engineering, Inc., July 1979.

Appendix A. Heat Pipe Wick Models

The purpose of this appendix is to present two generally accepted numerical models that describe liquid motion in a heat pipe wick, the Groove Analysis Program and the Beam piston model. The assumptions inherent in each model are discussed and a brief description of how each model is used to solve a wick flow problem is provided.

Groove Analysis Program

In a 1977 study on the performance of axially-grooved heat pipes, an in-depth analysis of the liquid flow in axial channels was funded by NASA and performed by B & K Engineering, Inc. (52). The result from the work was a computer code, named GAP, that numerically solved the differential equations governing the hydrodynamic flow. The theoretical model accounted for fluid recession into the wick as well as laminar and turbulent vapor flow conditions. Evaporator elevation above the condenser was included as an input to the code but was treated as a constant and was not allowed to vary in time. Good agreement between the theory and experimental heat pipe results was noted by the authors with deviations at the high and low elevation regimes.

The theoretical model is based on independent grooves equally affected by body forces. Incompressible, laminar flow is assumed for the liquid and Darcy flow is used to model the viscous pressure drop. Only body forces in the direction of liquid flow are addressed, and constant fluid properties and steady state operating conditions are assumed.

The governing equations are solved numerically by specifying an initial heat input and a minimum radius of curvature at the evaporator equal to one half the groove opening. The axial variation in the liquid radius of curvature required to support steady-state operation of the pipe is then determined by integrating the equations between the evaporator and the condenser. The value of the heat input to the pipe is varied until the

A-1

liquid radius of curvature at the end of the condenser equals to the radius of the vapor space. This value of heat is termed the capillary pumping limit.

Beam Piston Model

In this presentation, the wick is assumed to be an axial rectangular groove milled into a flat plate. The groove has a constant cross-sectional flow area, A_w, and length, L_w, with equal condenser and evaporator lengths of L_{co} and L_{ev}, respectively as shown by the solid line control volume in Figure A-1. Note that $L_w = L_{co} + L_{ev}$.
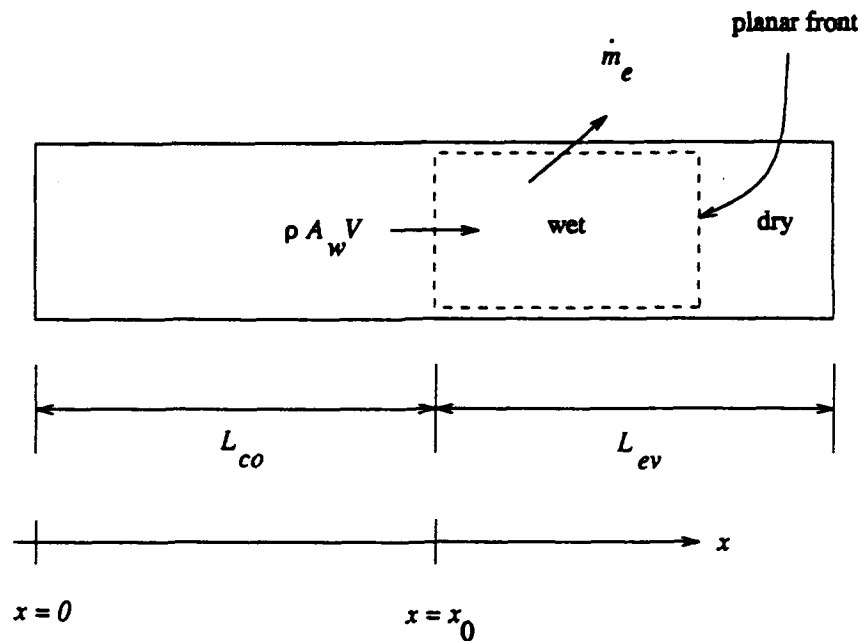

Figure A-1. Control Volume for Beam Piston Model--Continuity Analysis

The liquid control volume is depicted by the dotted line in the figure. The left hand side of the control volume is defined as $x = x_0$ and is located at a position along the wick such that $x_0 = (L_{co} + L_{ev})/2$. For this discussion, note that x_0 lies midway along the total wick length.

A-2

At any given time and axial location, the wick can either be totally wet (full) or totally dry (empty), but not both. The interface between the wet and dry regions, defined as the front, is assumed to be planar and perpendicular to the flow direction and serves as a moving boundary of the control volume. The location of this moving front is at location x. Continuity for this control volume requires that the sum of the time rate of change of mass within the control volume and the rate of mass entering the control volume minus the rate of mass exiting the control volume equal zero. Applying this statement of conservation of mass to Figure A-1 yields

$$\frac{d(\rho A_w \Delta x)}{dt} + \dot{m}_e - \rho A_w V = 0 \qquad \text{[A-1]}$$

where ρ is the liquid density, V is the liquid velocity at $x = x_0$, $\dot{m}_e$ is the mass flow lost from the wick due to evaporation, and $\Delta x = x - x_0$.

The liquid velocity is modeled using Figure A-2. The flow is assumed to be steady and the change in momentum flow is assumed to be negligible. Because of this assumption, the sum of all forces acting on the control volume must equal zero. Summing the forces in the flow direction yields

$$PA_w - PA_w - \frac{d(PA_w)}{dx} dx - \tau \tilde{A} = 0 \qquad \text{[A-2]}$$

where P is the liquid pressure, τ is the shear stress and $\tilde{A}$ is the circumferential wick area over which the shear force acts. Dividing by A_w and dx, Eqn [A-2] is rewritten as,

$$\frac{dP}{dx} = -\frac{\tau \tilde{A}}{A_w dx} \qquad \text{[A-3]}$$

Rewriting this equation in terms of the hydraulic radius, r_h, yields
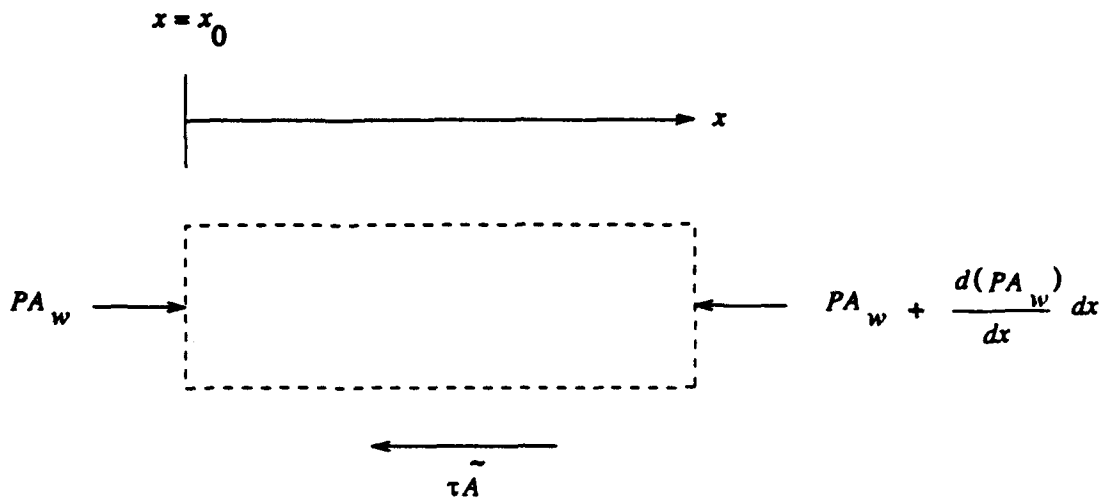
A-3

Figure A-2. Control Volume for Beam Piston Model--Momentum Analysis

$$\frac{dP}{dx} = -\frac{2\tau}{r_h} \qquad \text{[A-4]}$$

The right hand side of Eqn [A-4] may be rewritten as (41)

$$\frac{2\tau}{r_h} = \frac{\mu(f\cdot Re)V}{r_h^2} \qquad \text{[A-5]}$$

where μ is the liquid viscosity, f is the friction factor and Re is the Reynolds Number based on the hydraulic diameter. Substituting Eqn [A-5] into Eqn [A-4] and solving for velocity gives

$$V = -\frac{r_h^2}{\mu(f\cdot Re)}\frac{dP}{dx} \qquad \text{[A-6]}$$

Substituting Eqn [A-6] into Eqn [A-1] and noting that $\frac{d\Delta x}{dt} = \frac{dx}{dt}$ yields

$$\frac{dx}{dt} = -\frac{r_h^2}{\mu(f \cdot Re)} \frac{dP}{dx} - \frac{\dot{m}_e}{\rho A_w} \qquad [A\text{-}7]$$

For this model, the location of the liquid front is assumed to be the point at which the maximum capillary pressure difference is attained. The maximum capillary pressure difference for this geometry is

$$P_c = -\frac{\sigma}{R_{min}} \qquad [A\text{-}8]$$

where σ is the fluid surface tension coefficient and R_{min} is the minimum radius of curvature allowed by the geometry; in this case, one-half the groove width. Substituting this into Eqn [A-7] yields

$$\frac{dx}{dt} = \frac{r_h^2}{\mu(f \cdot Re)} \frac{\sigma}{R_{min} x} - \frac{\dot{m}_e}{\rho A_w} \qquad [A\text{-}9]$$

where the evaporative mass flow is assumed to be known. Integrating Eqn [A-9] with respect to time, t, provides the location of the liquid front as a function of time.

Vita

Major Michael K. Reagan was born on 20 August 1959 in Palo Alto, California. He graduated from Saint Francis High School, Mountain View, California in 1977 and attended the United States Air Force Academy, where he earned the degree of Bachelor of Science in Aeronautical Engineering. Upon graduation in 1981, he was assigned to Undergraduate Pilot Training at Reese AFB, where he graduated in 1982. He remained as a T-37 instructor pilot until 1985, when he was reassigned to Randolph AFB and the Pilot Instructor Training Center. In 1987, he was reassigned to Luke AFB as a student pilot in the F-15 Replacement Training Unit with a follow-on assignment to Keflavik NAS, Iceland. A medical disqualification removed him from the program and he was reassigned to Randolph AFB as executive officer to the Wing Commander. In May of 1989 he was reassigned to the Air Force Institute of Technology, School of Engineering, where he earned the degree of Master of Science in Aeronautical Engineering and remained to complete doctoral studies.

Permanent Address: 3410 Pebblecreek Drive
Beavercreek, Ohio 45432

REPORT DOCUMENTATION PAGE

Public reporting burden for this collection of information is estimated to average 1 hour per response, including the time for reviewing instructions, searching existing data sources, gathering and maintaining the data needed, and completing and reviewing the collection of information. Send comments regarding this burden estimate or any other aspect of this collection of information, including suggestions for reducing this burden, to Washington Headquarters Services, Directorate for information Operations and Reports, 1215 Jefferson Davis Highway, Suite 1204, Arlington, VA 22202-4302, and to the Office of Management and Budget, Paperwork Reduction Project (0704-0188), Washington, DC 20503.

1. AGENCY USE ONLY (Leave blank)	2. REPORT DATE April 1994	3. REPORT TYPE AND DATES COVERED Ph.D. Dissertation (Jan 90-Apr 94)

4. TITLE AND SUBTITLE
TRANSIENT BODY FORCE EFFECTS ON THE DRYOUT
AND REWET OF A HEATED CAPILLARY STRUCTURE

5. FUNDING NUMBERS

6. AUTHOR(S)

Michael K. Reagan, Major, USAF

7. PERFORMING ORGANIZATION NAME(S) AND ADDRESS(ES)

AFIT/ENY Bldg 640
2950 P Street
Wright-Patterson AFB OH 45433-7765

8. PERFORMING ORGANIZATION REPORT NUMBER

AFIT/DS/AA/94-1

9. SPONSORING / MONITORING AGENCY NAME(S) AND ADDRESS(ES)

WL/PO Bldg 18
1950 Fifth Street
Wright-Patterson AFB OH 45433-7251

10. SPONSORING / MONITORING AGENCY REPORT NUMBER

11. SUPPLEMENTARY NOTES

12a. DISTRIBUTION / AVAILABILITY STATEMENT

Approved for public release; distribution unlimited

12b. DISTRIBUTION CODE

13. ABSTRACT (Maximum 200 words)   A transient, one-dimensional numerical code was developed to model the liquid flow in a non-uniformly heated, axial square groove. The groove was subjected to transient body forces up to approximately 0.51 m/s^2. Axial variation in meniscus levels, shear stress and heat transfer between the groove wall and the liquid, axial conduction through the liquid, evaporation and body forces were accounted for in the model. Dryout and rewet of the groove were allowed; the front location was determined using conservation of mass and linear extrapolation.

A physical experiment was performed with a stainless steel plate into which eight square grooves were machined. Ethanol was used as the working liquid. One end of the plate was tilted relative to the other end and this tilt was varied with time, thereby providing the transient body force. The depth of the ethanol in the groove, and the dryout and rewet front locations, were experimentally measured.

Within the uncertainty of the measurements, the numerical results from the code predicted the correct movement of liquid within the groove structure and also the correct position of the dryout and rewet fronts.

14. SUBJECT TERMS

Body force, heat pipe, dryout, rewet, capillarity, meniscus

15. NUMBER OF PAGES
141

16. PRICE CODE

17. SECURITY CLASSIFICATION OF REPORT UNCLASSIFIED	18. SECURITY CLASSIFICATION OF THIS PAGE UNCLASSIFIED	19. SECURITY CLASSIFICATION OF ABSTRACT UNCLASSIFIED	20. LIMITATION OF ABSTRACT UL